

SNAPSHOT: Connections between Internal and Surface Properties of Massive Stars

Eoin J. Farrell,^{1*} Jose H. Groh,¹ Georges Meynet,² J.J. Eldridge,³
Sylvia Ekström,² Cyril Georgy²

¹*School of Physics, Trinity College Dublin, The University of Dublin, Dublin, Ireland*

²*Geneva Observatory, University of Geneva, Chemin des Maillettes 51, 1290 Sauverny, Switzerland*

³*Department of Physics, Private Bag 92019, University of Auckland, New Zealand*

Accepted XXX. Received YYY; in original form ZZZ

ABSTRACT

We introduce **SNAPSHOT**, a technique to systematically compute stellar structure models in hydrostatic and thermal equilibrium based on 3 structural properties – core mass M_{core} , envelope mass M_{env} and core composition. This approach allows us to connect these properties of stellar interiors to the luminosity and effective temperature T_{eff} in a more systematic way than with stellar evolution models. We compute core-H burning models with total masses of $M_{\text{total}} = 8$ to $60M_{\odot}$ and central H mass fractions from 0.70 to 0.05. Using these, we derive an analytical relationship between M_{core} , M_{total} and central H abundance that can be readily used in rapid stellar evolution algorithms. In contrast, core-He burning stars can have a wide range of combinations of M_{core} , M_{env} and core compositions. We compute core-He burning models with $M_{\text{core}} = 2 - 9M_{\odot}$, $M_{\text{env}} = 0 - 50M_{\odot}$ and central He mass fractions of 0.50 and 0.01. Models with $M_{\text{core}}/M_{\text{total}}$ from 0.2 to 0.8 have convective envelopes, low T_{eff} and will appear as red supergiants. For a given M_{core} , they exhibit a small variation in luminosity (0.02 dex) and T_{eff} (~ 400 K) over a wide range of M_{env} ($\sim 2 - 20M_{\odot}$). This means that it is not possible to derive red supergiant masses from luminosities and T_{eff} alone. We derive the following relationship between M_{core} and the total luminosity of a red supergiant during core He burning: $\log M_{\text{core}} \simeq 0.44 \log L/L_{\odot} - 1.38$. At $M_{\text{core}}/M_{\text{total}} \approx 0.2$, our models exhibit a bi-stability and jump from a RSG to a BSG structure. Our models with $M_{\text{core}}/M_{\text{total}} > 0.8$, which correspond to stripped stars produced by mass loss or binary interaction, show that T_{eff} has a strong dependence on M_{env} , M_{core} and the core composition. We constrain the mass of one of these stripped stars in a binary system, HD 45166, and find it to be less than its estimated dynamical mass. When a large observational sample of stripped stars becomes available, our results can be used to constrain their M_{core} , M_{env} , mass-loss rates and the physics of binary interaction.

Key words: stars: evolution – stars: massive – stars: interiors – stars: atmospheres

1 INTRODUCTION

The evolution of massive stars is dominated by the effects of mass loss, rotation, convection and binary interaction. Because of uncertainties in these physical mechanisms, we have a limited understanding on how massive stars evolve, die, and affect their host galaxies. Mass loss, convection, rotation and binary interaction affect the evolution of massive stars by modifying their internal and surface properties. Depending on their impact, a star can evolve to have different combinations of core mass, envelope mass and core composition. These are important properties of stellar structure and

they affect the observable surface properties of massive stars. This connection is the main topic of this paper.

Mass loss by stellar winds has a dramatic effect on the evolution of massive stars (e.g., Chiosi & Maeder 1986; Maeder & Meynet 2012; Smith 2014). Depending on the assumptions in a stellar evolution model for mass-loss rates, a star can evolve to very different regions of the Hertzsprung-Russell (HR) diagram (Meynet et al. 1994; Vanbeveren et al. 2007) leading to different outcomes at the end of their lives (Eldridge & Tout 2004; Georgy 2012; Meynet et al. 2015; Renzo et al. 2017). While a theoretical framework for computing mass-loss rates exists for the main sequence (MS; Vink et al. 2001), mass-loss rates are uncertain for other regions of the HR diagram (e.g., De Beck et al. 2010; Mauron & Josselin 2011; Beasor & Davies 2018). Additionally, there is increasing theoretical and observational evidence that massive stars may undergo erup-

* E-mail: efarrel4@tcd.ie

tive and explosive mass-loss events during the late nuclear burning stages before core-collapse (e.g., Kotak & Vink 2006; Smith et al. 2007; Pastorello et al. 2007; Gal-Yam & Leonard 2009; Fraser et al. 2013; Gal-Yam et al. 2014; Smith 2014; Groh 2014; Fuller 2017; Yaron et al. 2017; Boian & Groh 2018). Despite their potential significance, the nature of these eruptions is very uncertain and they are not usually accounted for in stellar evolution models.

Another important, yet uncertain component of stellar evolution models is the behaviour of their convective cores. Convection is usually parameterised by an overshooting parameter, α_{ov} , which is calibrated from observations. Different values for α_{ov} are adopted in different models (e.g., Brott et al. 2011a; Ekström et al. 2012; Choi et al. 2016; Higgs & Vink 2019), depending on the calibration method. Furthermore, the dependence of α_{ov} on mass and metallicity is also uncertain (Castro et al. 2014). For a given initial mass, the choice of α_{ov} can significantly affect the mass of the convective core during the MS phase and the mass of the He-core during subsequent burning stages. As well as the value adopted for α_{ov} , the exact implementation of core-overshooting in the stellar evolution code can also modify a star's evolution (Martins & Palacios 2013).

Stellar rotation can also significantly affect the evolution of massive stars (e.g., Maeder & Meynet 2000; Meynet & Maeder 2000; Heger et al. 2000, 2005; Maeder 2009; Brott et al. 2011a,b; Chieffi & Limongi 2013). Massive stars exhibit a range of rotational velocities (Huang et al. 2010; Hunter et al. 2008; Ramírez-Agudelo et al. 2013, 2015; Dufton et al. 2019). For sufficiently low velocities, rotation is expected to have a qualitatively similar effect on the evolution of the convective core mass to core overshooting. The behaviour of stellar structure under extreme rotation has recently been suggested to be significantly different than previously thought, with consequences for the late stages of stellar evolution and the explosion (Aguilera-Dena et al. 2018).

The possible evolutionary outcomes for massive stars is greatly complicated by the possibility of binary interaction (e.g., Paczyński 1971; Podsiadlowski et al. 1992; Eldridge & Stanway 2009; de Mink et al. 2013; Yoon 2015; Eldridge et al. 2017; Zapartas et al. 2019). Observations indicate that a large fraction of stars exist in binary systems (e.g., Garmany et al. 1980; Kobulnicky & Fryer 2007; Chini et al. 2012; Kobulnicky et al. 2014; Sota et al. 2014; Dunstall et al. 2015; Almeida et al. 2017). Binary systems can have a wide range of orbital periods, mass-ratios and orbital eccentricities (Moe & Di Stefano 2017). In particular, a significant fraction of massive stars are observed to reside in close binary systems and will interact with a companion at some point during their life (Sana et al. 2012, 2013; Moe & Di Stefano 2017). Despite the significant progress in our understanding of binary interaction, the outcomes of this process are not always fully understood. This contributes to the overall uncertainty in our understanding of the evolution of massive stars.

Mass loss, convection, rotation and binary interaction have important effects on the evolution of stars. One of their main effects is to modify the core and envelope masses (M_{core} and M_{env} , respectively) of a star at a given evolutionary stage, i.e. for a given core composition. For example, higher mass-loss rates produce a lower M_{env} , and in some cases also produce a lower M_{core} . Higher convective core-overshooting (i.e. a larger α_{ov}) produces a higher convective core mass and a corresponding lower M_{env} during the MS, and a higher M_{core} during the post-MS evolution. Binary interaction can dramatically change both M_{core} and M_{env} . Envelope masses can be decreased as a result of stripping of the envelope by Roche-Lobe overflow (RLOF), increased by accretion from a companion star, and can be modified through common-envelope

evolution or a merger event (van Bever & Vanbeveren 1998; Dominik et al. 2012; de Mink et al. 2014; Ivanova 2018; Fragos et al. 2019).

The main purpose of this work is to systematically produce a grid of stellar structure models in hydrostatic and thermal equilibrium, based on three important structural properties: M_{core} , M_{env} and the core composition (described in this paper by X_c and Y_c). We refer to these stellar structure models as *SNAPSHOT* models. The models are constructed in a way that allows us to vary the value of one structural property, while keeping the other properties constant, e.g. varying M_{env} while keeping M_{core} , X_c and Y_c constant. This allows us to isolate the effect of each structural property on the surface properties of the star.

This type of approach to stellar models was first used by Cox & Salpeter (1961). It was further developed by Giannone (1967) and Giannone et al. (1968) to study core-Helium burning stars at low and intermediate masses, and by Lauterborn et al. (1971a) and Lauterborn et al. (1971b) to study the occurrence of blue loops of intermediate mass stars in the HR diagram. However, to our knowledge, this method has never been used in a systematic and comprehensive way as in our work. Moreover some of these approaches used very simple internal structures. In this work, we take advantage of the advancements in stellar evolution and computational capabilities over the last decades to produce state-of-the-art models of stellar structure.

We outline some of the advantages of the *SNAPSHOT* models we present in this work below.

(i) The surface properties of a star depend on its internal structure. This approach allows us to make direct connections between the structural properties (M_{core} , M_{env} , X_c and Y_c) and the surface properties (luminosity, effective temperature, T_{eff} , and surface gravity, $\log g$). For example, with this approach we can directly compare between two core-He burning stars with exactly the same Helium core, but with different M_{env} . These types of comparisons are difficult to obtain from classical stellar evolution models without fine-tuning of processes such as mass loss, overshooting etc.

(ii) It is often difficult to disentangle cause and effect in stellar evolution. The equations of stellar structure and evolution are highly non-linear and processes such as rotation, convection etc. can combine and interact to produce complex effects on the evolution of a star. It is often challenging to connect these evolutionary effects to a particular physical process or combination of processes. Our approach using *SNAPSHOT* stellar models is not subject to such complex evolutionary effects, which allows us to more easily disentangle connections between internal and surface properties. These connections can then be used to help establish cause and effect in stellar evolution models.

(iii) We can produce a wider range of stellar structures than are currently obtained in stellar evolution calculations. Stellar evolution calculations always include prescriptions for computing effects such as mass loss and effects of close binary interactions such as Roche-Lobe Overflow. These prescriptions may limit the range of stellar structures that are produced in evolutionary calculations. Our method allows us to compute stellar structures that may not be produced in stellar evolution calculations and to see if they correspond to observations.

(iv) *SNAPSHOT* models can help us to study how many different internal structures could correspond to a given set of observed properties (such as luminosity, T_{eff} and surface gravity). This is very important, as it will allow us to determine the degree of degeneracy between observable and non-observable stellar properties. For

SNAPSHOT models: Constructing Equilibrium Stellar Structure Models

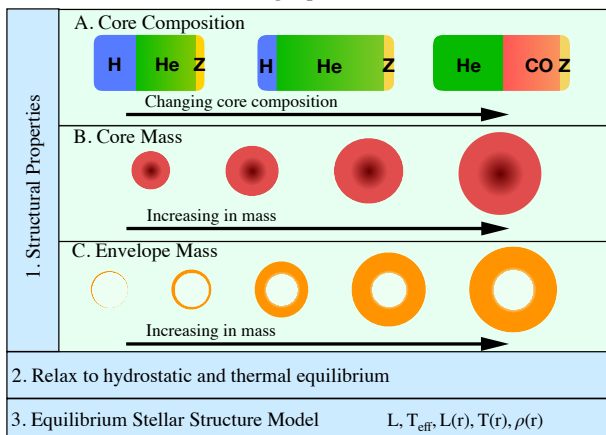


Figure 1. Schematic outline of the construction of SNAPSHOT stellar structure models with different core compositions, core masses and envelope masses. We first select a core composition (1A). Secondly, we select a core mass to go with this core composition (1B). Finally, we select an envelope mass (1C). Using a stellar evolution code, the models are allowed to relax to a state of hydrostatic and thermal equilibrium (2). The final stellar model produces both the surface properties, e.g. luminosity and effective temperature, as well as the interior profiles of the standard quantities, e.g. temperature, luminosity, and density (3). See Sec. 2 for more details.

instance, we often deduce the actual/initial mass of a star from its observed position in the HR diagram using stellar evolution models. The result from this procedure depends on the set of stellar evolution models that are used and their assumptions about convection, binary interaction etc. The SNAPSHOT model approach will allow us to better estimate the degree of uncertainty of these deductions and to determine the regions where it gives reliable and unreliable results. It may also provide some hints into what kinds of additional observations could help to reduce the degeneracy.

(v) The results from our SNAPSHOT models can be useful for improving the approximations used in rapid stellar evolution algorithms to compute single and binary population synthesis models (e.g., Eggleton et al. 1989; Pols et al. 1995; Tout et al. 1996, 1997; Hurley et al. 2000, 2002).

SNAPSHOT stellar structure models offer a complementary approach to stellar evolution models to study the lives of stars. Stellar evolution models allow us to obtain quantities such as age, to study connections between different evolutionary stages, to analyse short phases of stellar evolution such as those when the star is out of thermal equilibrium and to derive the frequency of evolutionary outcomes assuming a set of initial conditions. Our hope is that SNAPSHOT models can be used alongside stellar evolution models to help to progress our understanding of how stars evolve.

We describe our method for producing SNAPSHOT stellar structure models in detail in Sec. 2. We analyse our results for core-H burning stars and core-He burning stars in Sections 3 and 4 respectively. In Sec. 5, we discuss connections between our SNAPSHOT stellar structure models and the evolution of massive single and binary stars. We conclude our analysis in Sec. 6.

2 METHOD

A systematic method to compute stellar structure models with a range of core compositions, core masses and envelope masses requires an alternative approach to the usual methods for computing stellar evolution models¹. In Fig. 1, we provide a schematic outline of our approach to compute SNAPSHOT stellar structure models. We use the MESA software instrument (r10398; Paxton et al. 2011, 2013, 2015, 2018, 2019) to compute our models. Our method can be summarised in the following three steps:

(i) To produce the initial stellar structures with a given M_{core} , M_{env} and core composition, we compute a stellar evolution model with MESA from the zero-age main sequence until the end of core-He burning.

(ii) Using the stellar structures produced in (i), we modify some of the input controls to allow us to change the total mass of the star, without the star evolving.

(iii) We allow the modified structures from (ii) to relax to hydrostatic and thermal equilibrium.

We would like to emphasise that our approach is very flexible and can easily be updated to include new physics. Secondly, we will provide all our input files online and, as MESA is open-source, the SNAPSHOT method can easily be implemented by others. Thirdly, our method also benefits from the active development in the MESA code in improving and updating the physical ingredients in the models.

The first step involves computing a stellar evolution model with MESA from the zero-age main-sequence until the end of core-He burning. For these models, we adopt similar physical inputs as in the MIST grid of stellar evolution models (Choi et al. 2016), which were also computed using MESA. We discuss the potential effects of the input physics in Sec. 5.3. We choose to apply this technique to study massive stars ($> 8M_{\odot}$) at solar metallicity for this paper, but the same technique can also be applied to intermediate and low mass stars and also to stars at different metallicities. This simply requires computing a suitable initial stellar evolution model. Our core-He burning stellar structure models have Helium core masses of 2 to $9M_{\odot}$. These cores correspond to stellar evolution models with initial masses of 8 to $25M_{\odot}$ assuming our physical inputs detailed below. We explore a wide range of M_{env} from 0 to $50M_{\odot}$, so that the total masses of our core-H and core-He burning models range from 2 to $59M_{\odot}$. We explore core-H burning stellar structure models with values of X_{c} from 0.70 to 0.05 and core-He burning models with $Y_{\text{c}} = 0.50$ and 0.01. We summarise the physical ingredients that we use below.

(i) We adopt a solar metallicity of $Z = 0.020$ (with the solar abundance scale from Grevesse & Sauval (1998)) for all models, with an initial He abundance of 0.26. The exact value of the metallicity, C, N, O and Fe abundances affect the stellar properties.

(ii) For mass loss, we use the ‘Dutch’ wind scheme in MESA with the default scaling factor of 1.0. This wind scheme combines mass-

¹ In principle, it is possible to compute a stellar evolution model and fine-tune the input parameters governing various physical processes e.g. mass loss, convective core-overshooting or binary interaction to achieve a desired combination of core composition, M_{core} and M_{env} . However, this would be difficult to do in a systematic way as these processes often have complex interactions and feedback effects that affect the evolution of the star. For example, larger convective core overshooting produces a more massive core, a higher luminosity and higher mass-loss rates which can then affect the mass of the core.

loss rates from [Vink et al. \(2001\)](#) and [Nugis \(2000\)](#) for hot stars ($> 10^4\text{K}$) and from [de Jager et al. \(1988\)](#) for cool stars ($< 10^4\text{K}$).

(iii) We use the Ledoux criterion for convective stability, with a semi-convective efficiency of $\alpha_{\text{sc}} = 0.1$.

(iv) We use a time-dependent, diffusive convective core-overshooting parameter ([Herwig 2000](#); [Paxton et al. 2011](#)). We adopt the same overshooting parameters as in the MIST models ([Choi et al. 2016](#)) with core overshooting of $f_{\text{ov, core}} = 0.016$ (roughly equivalent to $\alpha_{\text{ov}} = 0.2$ in the step overshoot scheme), and $f_{\text{ov, shell}} = f_{\text{ov, env}} = 0.0174$.

(v) For most of the models, we use the standard mixing-length theory to model convective mixing, with a mixing-length parameter of $\alpha_{\text{mlt}} = 1.82$. For some of the higher mass models, in order to allow the models to converge it was necessary to use a modified treatment of convection known as MLT++ ([Paxton et al. 2013](#)). MLT++ reduces the temperature gradient in some radiation-dominated convective regions to make it closer to the adiabatic gradient. This boosts the efficiency of energy transport which allows the model to run with reasonable timesteps.

(vi) As a surface boundary condition, we use the `simple_photosphere` option in MESA ([Paxton et al. 2011](#)).

(vii) We adopt the `mesa_49.net` nuclear network in MESA which tracks and solves for the abundances of 49 species.

(viii) The models are all non-rotating.

For each stellar evolution model, we save snapshots at two points during core-H burning (for $X_{\text{C}} = 0.35$ and 0.05) and two points during core-He burning (for $Y_{\text{C}} = 0.50$ and 0.01). In principle, any core composition can be studied, as long as the star is in thermal equilibrium. We take the snapshot models we saved from the stellar evolution models and change the value of M_{env} without the star evolving. To do this, we modify the following inputs in MESA to effectively pause the evolution of the star:

(i) We turn off changes in abundances of the chemical elements due to nuclear burning by setting `dxdt_nuc_factor = 0` in MESA. This allows the nuclear energy generation rates to remain the same, but prevents the chemical abundances from changing.

(ii) We turn off element diffusion by setting `do_element_diffusion = 0` and turn off all other mixing by setting `mix_factor = 0`.

(iii) We turn mass loss off.

While the evolution of the star is paused, we use a routine in MESA called `mass_change` which allows an arbitrary mass-loss rate or mass-accretion rate from/to the surface of the star. We set the rate of mass loss/accretion to be $10^{-12}M_{\odot}/\text{yr}$. This low value ensures that the star will remain in thermal equilibrium while it is accreting or losing mass. We set the chemical abundance of the accreted material to be the same as the surface abundances. For each of the core masses and core compositions, we allow the star to lose mass until the H-rich envelope is stripped entirely, and to accrete mass until the star reaches an envelope mass of $50M_{\odot}$ (as defined when we start to modify the mass). For each core, we save models for a range of M_{env} .

We allow every model to relax to hydrostatic and thermal equilibrium by restarting the evolution, with mass loss turned off but with all other physical inputs unchanged from the initial stellar evolution. This allows the convective core to readjust to the modified structure. We set a stopping criterion for these models based on $L_{\text{nuc}}/L_{\text{total}}$, the ratio of the total nuclear energy generation to the total luminosity of the star. The time for the models to mix by

convection and relax to thermal equilibrium is typically on the order of ~ 1 kyr or less.

3 APPLICATION TO MAIN SEQUENCE STARS

In this section, we apply our `SNAPSHOT` method to MS stars i.e. core-H burning stellar structures. We analyse our core-H burning models in terms of three structural properties, the convective core mass (M_{core}), the envelope mass (M_{env}) and the central hydrogen abundance (X_{C}). We define the envelope as the rest of the star above the convective core. For models to which we have added mass, we find that the size of the convective core adjusts to the new stellar structure during the relaxation procedure. Material from the H-rich envelope mixes with H-depleted material in the core, the convective core increases in mass and the value of X_{C} increases. This so-called “rejuvenation” phenomenon in MS stars, in which a star can accrete from its companion and end up with a higher value of X_{C} than before the mass transfer episode, has been well studied in various stellar evolution contexts (e.g., [Hellings 1983, 1984](#); [Schneider et al. 2014](#)). Whether or not rejuvenation will take place depends on the treatment of convective stability and the choice of the semi-convective efficiency α_{sc} ([Braun & Langer 1995](#)).

Our core-H burning structure models have M_{core} ranging from 1 to $45M_{\odot}$, M_{env} from 6 to $18M_{\odot}$ and X_{C} from 0.70 to 0.05. We find that the combinations of M_{core} , M_{env} and core composition are quite limited (Figs. [A1](#) and [2](#)). We indicate the values of M_{core} , M_{env} and X_{C} in Fig. [A1](#) in Appendix [A](#), where we plot the values of M_{env} and M_{core} for different values of X_{C} . In Fig. [2](#), we plot the relationship between M_{core} and M_{total} . For a core-H burning star, the value of M_{core} is determined by the total mass of the star and the value of X_{C} . We fit the following function relating the total stellar mass M_{total} , the convective core mass M_{core} and X_{C} :

$$M_{\text{core}} = aM_{\text{total}}^d + bM_{\text{total}}X_{\text{C}} + c \quad (1)$$

We obtain best fit values of $a = 0.045$, $b = 0.304$, $c = -0.133$ and $d = 1.627$. For a star of a given total mass, the convective core mass is lower for models with lower X_{C} , as expected from stellar evolution models. Furthermore, the dependence of M_{core} on X_{C} is steeper for larger stellar masses. While the value of the convective core mass for a given total mass depends on our assumptions for convective overshooting, the overall trends observed in Fig. [2](#) do not depend on overshooting assumptions.

The mass of the convective core in core-H burning stars as a function of mass has been studied before for models at the beginning of the main sequence ([Schwarzschild & Härm 1958](#); [Schwarzschild 1961](#); [Stothers 1970, 1974](#); [Maeder 1980](#); [Maeder & Mermilliod 1981](#); [Maeder & Meynet 1987, 1988, 1989](#); [Langer et al. 1989](#); [Pols et al. 1998](#)), by [Stothers & Chin \(1985\)](#) at the beginning and end of the MS, and by many others as in the context of stellar evolution models. Here, we make a connection between the M_{core} , the total stellar mass and X_{C} (Fig. [2](#)), providing fits for the convective core mass for a range of stellar masses and core compositions that can be easily used by the community. These calculations are useful for a number of reasons, for instance in rapid binary stellar evolution algorithms for computing population synthesis models (e.g., [Belczynski et al. 2002](#); [van Bever & Vanbeveren 1998](#); [Hurley et al. 2000, 2002](#); [Izzard et al. 2006](#); [Belczynski et al. 2008](#); [Eldridge et al. 2008](#); [Eldridge & Stanway 2009](#); [de Mink & Belczynski 2015](#); [Eldridge et al. 2017](#)) where stellar properties need to be updated after a mass transfer episode.

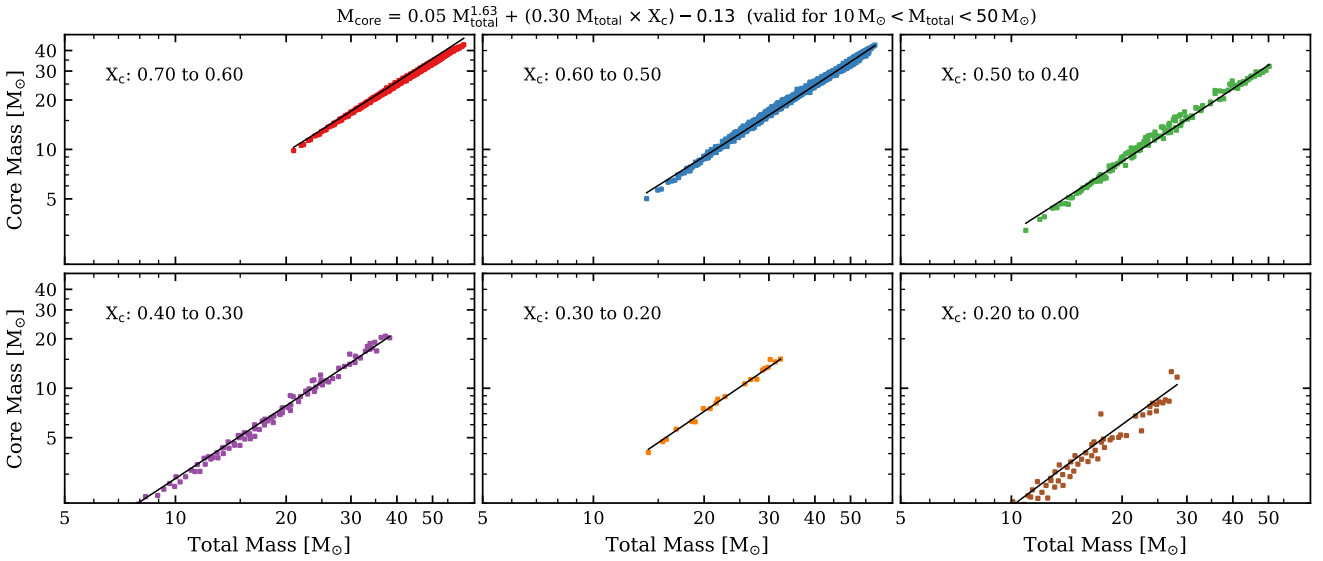


Figure 2. Convective core mass as a function of the total mass for core-H burning models. The models are divided up into bins according to X_c as indicated in each plot. The best fit line for each X_c is plotted in black and corresponding equations relating M_{core} and the total mass M_{total} are indicated in the upper left of each subplot.

We have compared the location of our core-H burning SNAPSHOT models in the HR diagram to standard MESA stellar evolution models (Choi et al. 2016) and they are consistent, as expected. For the sake of brevity we do not include these comparisons here, as it is a well known result (e.g. Henyey et al. 1959). Further tests show that the luminosity and T_{eff} of core-H burning SNAPSHOT stellar structure models not depend very much on the amount of overshooting. Models with no overshooting and with the overshooting assumptions we adopt in this paper differ by about 0.01 dex in $\log L/L_{\odot}$ and $\log T_{\text{eff}}$ despite the differences in convective core masses.

4 APPLICATION TO POST-MAIN SEQUENCE STARS

In this section, we apply our SNAPSHOT technique to post-MS core-Helium burning stars. We construct core-He burning SNAPSHOT structure models based on three structural properties: the Helium core mass M_{core} , the H-rich envelope mass M_{env} and the central He abundance Y_c . The He-core is defined as the central Hydrogen depleted region where $X < 10^{-4}$. The H-envelope is defined as the rest of the star above the He-core. Our models have He-core masses ranging from $M_{\text{core}} = 2$ to $9M_{\odot}$ ², envelope masses of $M_{\text{env}} = 0.001$ to $50M_{\odot}$ and a central Helium abundance of $Y_c = 0.50$ and 0.01 .

Figure 3 shows the values of M_{core} and M_{env} for our core-He burning models with $Y_c = 0.50$. Each point corresponds to an individual SNAPSHOT stellar structure model. A similar figure for models with $Y_c = 0.01$ is included in Appendix B. In contrast to core-H burning stars (Figs. 2 and A1), core-He burning stars in thermal equilibrium can have a wide range of combinations of M_{core} , M_{env} and Y_c (Fig. 3). The difference in the variety of stellar structures for core-He and core-H burning stars is due to the fact that there are (usually) two nuclear burning regions in core-He burning stars (the He-core and H-shell), while there is only one burning

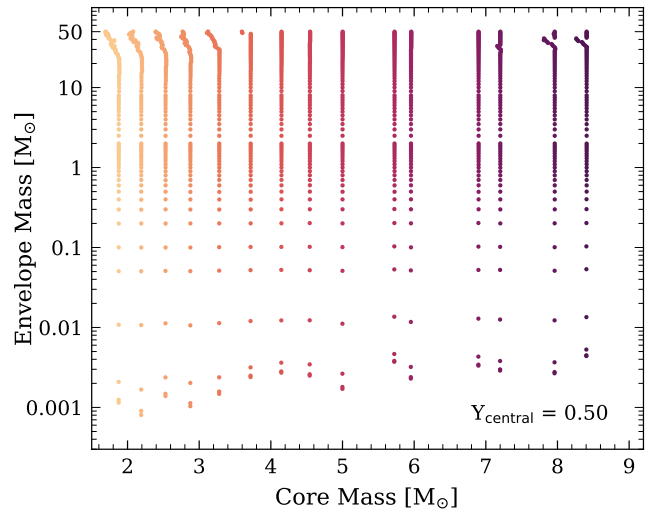


Figure 3. Envelope mass as a function of the core mass for our core-He burning models with $Y_c = 0.50$. The colours indicate structure models with the same core mass.

region in core-H burning stars. To understand the difference, we can consider what happens if we begin with a star in hydrostatic and thermal equilibrium with a given M_{core} and M_{env} , and then very slowly increase M_{env} , such that the star remains in thermal equilibrium. The star must respond by readjusting its structure to support the increased mass. With only one nuclear burning region, a core-H burning star can respond only by producing more energy in its core. An increased mass changes the mechanical equilibrium structure of the star. The pressure and temperature gradients inside the star must increase to support the increased mass. As a result, the central temperature increases and hence the nuclear reaction rates in the core increase. This will generally cause an increase in the mass of the convective core, depending on the assumptions for mixing,

² These He-core masses correspond to initial masses of $8-25M_{\odot}$, assuming single star evolution with our physical ingredients.

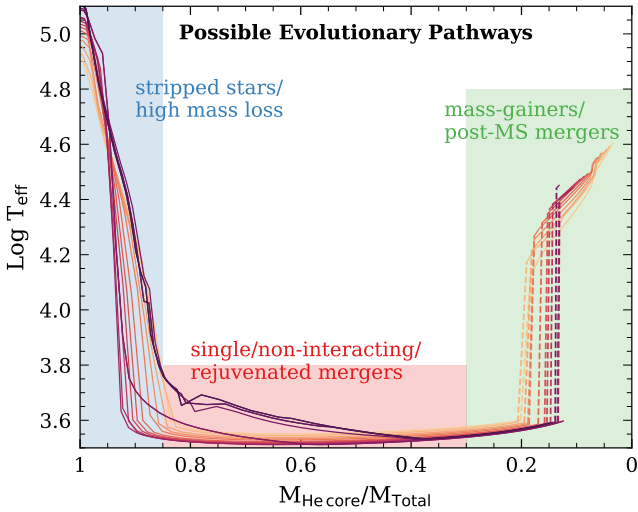


Figure 4. Effective temperature as a function of the core mass ratio for core-He burning models with constant M_{core} , $Y_{\text{c}} = 0.01$ and M_{env} varying from 0 to $50M_{\odot}$ (same models as in panel d of Fig. 12). We roughly sketch possible binary evolutionary pathways which may produce the same stellar structures as these models.

particularly semi-convection. In contrast, a core-He burning star, with two nuclear burning regions (the He-core and the H-shell), could respond to the increased mass by modifying its mechanical equilibrium in a way that results in an increase in the energy production in either the He-core, the H-shell or some combination. Our models show that, in almost all cases, core-He burning stars respond to an increase in the total mass in a way that increases the energy production in the H-shell. The value of M_{env} can change over a wide range without significantly modifying the conditions in the He-core, such as the central temperature (Appendix C). This leads to the wide variety of combinations of M_{core} and M_{env} for core-He burning stars.

In Fig. 4, we summarise the results we obtain for our core-He burning models by plotting the value of T_{eff} as a function of the core mass ratio. Each line consists of models with constant M_{core} , a constant $Y_{\text{c}} = 0.50$ and M_{env} varying from 0 to $50M_{\odot}$ (same models as Fig. 12d). Dashed lines indicate a sharp transition from red supergiants to hotter, more luminous stellar structures due to a bi-stability in the stellar structure equations. To put our results in context, we discuss connections between our `SNAPSHOT` models and stellar evolution pathways.

Stellar structures with high core mass ratios (shaded in blue in Fig. 4) correspond to stripped stars with low values of M_{env} . Most stripped stars are expected to form in binary systems when the primary star expands after the MS, fills its Roche-Lobe and is stripped of its envelope by the secondary (Podsiadlowski et al. 1992). Some may also form due to high mass loss from a single star (Groh et al. 2013). These stars correspond to Regime I of the core-He burning models discussed in Sec. 4.1. Stellar structures with intermediate core mass ratios (shaded in red in Fig. 4) are mostly red supergiants. They are expected to be formed by single stars, non-interacting stars in binary systems or stars that rejuvenate after accreting mass. These stars correspond to Regime II in Sec. 4.1. Stars with lower core mass ratios $\lesssim 0.2$ probably only form in binary systems, either as the product of mass-accretion or a post-MS merger (e.g., Eldridge et al. 2017; Zapartas et al. 2019). For example, a merger between a core-He burning star and a relatively

massive main sequence companion could produce a star with a small He-core and a very high mass H-rich envelope (e.g., Justham et al. 2014). These stars may resemble OB-type stars or blue supergiants (BSGs) and they correspond to Regime III from Sec. 4.1. They lie to the right of the MS in the HR diagram which may help to explain observations of a large number of stars in this location in the HR diagram (Castro et al. 2014).

In the following sections, we discuss our core-He burning models in detail and describe the connections between internal and surface properties when varying M_{env} (Sec. 4.1), M_{core} (Sec. 4.2), and Y_{c} (Sec. 4.3).

4.1 Effect of Envelope Mass

To analyse how the surface properties of a core-He burning star depend on the mass of the H-envelope, we discuss a representative set of models with the same He-core mass and composition ($M_{\text{core}} = 4.1M_{\odot}$ and $Y_{\text{c}} = 0.50$) and different envelope masses (M_{env} ranges from 0.0 to $50.0M_{\odot}$). We choose this particular set of models as its core properties are representative of massive core-He burning stars. A He-core mass of $4.1M_{\odot}$ corresponds to an initial mass of $\sim 14M_{\odot}$, assuming single star evolution and our physical ingredients. Additionally, $Y_{\text{c}} = 0.50$ corresponds to the middle of core-He burning phase.

In Fig. 5, we plot this set of models in the HR diagram. From these, we select 7 models, labelled A – G, which represent the qualitative trends in surface properties as a function of M_{env} . We indicate the location in the HR diagram and the value of M_{env} for each of the models A-G in Fig. 5. We summarise the internal and surface properties for models A-G in Table 1.

Based on the location in the HR diagram, we divide the models plotted in Fig. 5 into Regimes I, II and III. Regime I consists of stars with no H-envelope or low envelope masses and with mostly high effective temperatures T_{eff} . We define the transition between Regimes I and II at $\log(T_{\text{eff}}) = 3.7$ or $T_{\text{eff}} = 5011$ K. Regime II consists of stars with intermediate envelope masses, a radiative H-burning shell and a convective outer envelope. They are located near the Hayashi line in the HR diagram. The transition between Regime II and III is defined by an abrupt change in the solution of the stellar structure equations from a cool star with a convective outer envelope to a hotter, more luminous star with a convective H-burning shell and a radiative outer envelope. Stars with envelope masses above this transition are defined to be in Regime III.

In Fig. 6, we plot the surface luminosity, T_{eff} , surface gravity ($\log g$), radius (R) and $F_{\text{H-shell}}$ (the fraction of the total nuclear energy that is generated in the H-burning shell) as a function of M_{env} for the same set of models in Fig. 5. The transitions between Regimes I, II and III are indicated by grey vertical lines. We also label models A-G in each panel. Models A and B are in Regime I with envelope masses of 0.0 and $0.5M_{\odot}$ respectively. Models C, D and E are in Regime II, close to the Hayashi line, with envelope masses of 2.0, 6.0 and $17.0M_{\odot}$ respectively. Models F and G are in Regime III with envelope masses of 18.0 and $50.0M_{\odot}$ respectively.

To investigate the presence of convective regions as a function of M_{env} , we plot in Fig. 7 the envelope mass on the x-axis and the Lagrangian envelope mass coordinate on the y-axis for the same representative set of models as in Fig. 5. This is similar to a normal Kippenhahn plot, with convective regions indicated in solid color. In Fig. 8, we plot internal abundance profiles, internal temperature profiles and internal nuclear burning profiles for models A – G. Convective regions are hashed in the abundance and temperature profile plots.

Table 1. Summary of surface properties for Models A – G with a He-core mass of $4.1M_{\odot}$ and a central Helium abundance of 0.50. M_{env} indicates the mass of the H-rich envelope above the He-core. $F_{\text{H-shell}}$ refers to the fraction of the total nuclear energy that is generated by H-Shell burning.

Model	$M_{\text{core}} [M_{\odot}]$	$M_{\text{env}} [M_{\odot}]$	$M_{\text{total}} [M_{\odot}]$	$\log T_{\text{eff}} [\text{K}]$	$T_{\text{eff}} [\text{K}]$	$\log L/L_{\odot}$	$\log g$	$\log R/R_{\odot}$	$F_{\text{H-shell}}$
A	4.1	0.0	4.1	4.96	91700	4.37	5.48	-0.21	0.00
B	4.1	0.5	4.6	4.45	28000	4.53	3.32	0.89	0.17
C	4.1	2.0	6.1	3.53	3390	4.58	-0.28	2.76	0.28
D	4.1	6.0	10.1	3.54	3460	4.59	-0.04	2.74	0.30
E	4.1	17.0	21.1	3.58	3800	4.61	0.42	2.67	0.34
F	4.1	18.0	22.1	4.29	19620	5.04	2.87	1.46	0.75
G	4.1	50.0	54.1	4.51	32590	5.73	3.44	1.36	0.95

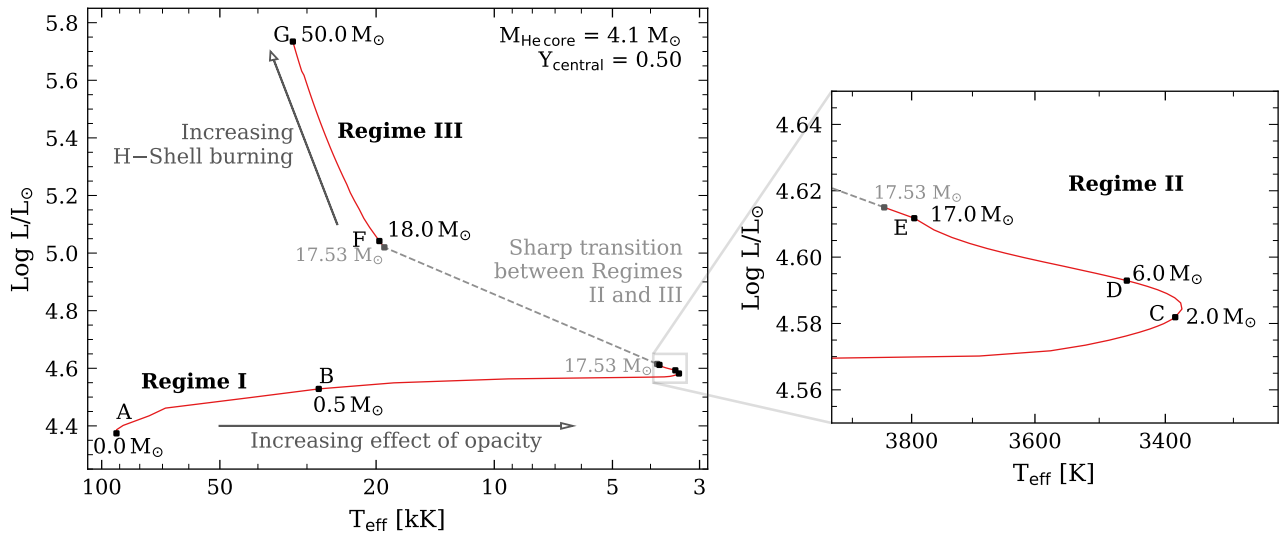


Figure 5. HR diagram showing core-He burning models with $M_{\text{core}} = 4.1M_{\odot}$, $Y_c = 0.50$ and varying H-rich envelope mass in the range $0 - 50M_{\odot}$ (M_{env} indicated in brackets). We label 7 representative models (A – G) to discuss the trends in the surface properties as a function of envelope mass (Sects. 4.1.1, 4.1.2 and 4.1.4). The right panel shows a zoom-in of the RSG region (models C, D and E).

In Sections 4.1.1 – 4.1.4 below, we discuss Figs. 5, 6, 7 and 8 in detail. We analyse the trends in surface properties as a function of envelope mass and establish connections between the internal and surface properties.

4.1.1 Regime I – Stripped Stars (Models A and B)

We begin by discussing a model with a $4.1M_{\odot}$ He-core and no envelope (Model A). It has a high T_{eff} of 92 000 K, is highly compact with a radius of $R = 0.62R_{\odot}$ and has a high surface gravity of $\log g = 5.48$ (middle panel of Fig. 6). The $4.1M_{\odot}$ He-core is composed of a $2.2M_{\odot}$ convective core, with $Y_c = 0.50$, and a $1.9M_{\odot}$ Helium rich shell (Fig. 8).

For only a modest increase in the envelope mass from $M_{\text{env}} = 0$ to $0.5M_{\odot}$ (Model B), the value of T_{eff} drops sharply from 92 000 K to 28 000 K. This is because the effect of opacity in the envelope increases with increasing M_{env} . The increased effect of opacity produces a larger stellar radius and a lower T_{eff} . While this effect has been identified before in stellar evolution models (e.g., Groh et al. 2014; Meynet et al. 2015), with our models we can investigate this behavior in a more systematic way as a function of M_{env} , M_{core} , and Y_c . We find that the luminosity increases slightly when increasing M_{env} from 0 (model A) to $0.5M_{\odot}$ (model B). This is due to the presence of a second nuclear energy generation region, i.e. the H-burning shell. In model B, 17 per cent of the total energy

is generated in the H-shell, compared to 0 per cent in model A (see Fig. 6 and Table 1). The presence of the H-burning shell and its contribution to the total luminosity can also be seen by comparing the energy generation profiles for models A and B in Fig. 8.

4.1.2 Regime II – Red Supergiants (Models C, D, E)

As the value of M_{env} increases, the star responds to the increased mass by increasing the energy generation in the H-burning shell. As the value of M_{env} increases from 2 to $17M_{\odot}$ (i.e. from model C to E), $F_{\text{H-shell}}$ increases from 0.28 to 0.34 (Fig. 6). As well as the increased energy generation in the H-shell, the mass of the convective region in the envelope increases greatly from model C to E (Figs. 7 and 8). Over a wide range of M_{env} , the mass of the convective region in the outer envelope increases with M_{env} almost as fast as M_{env} (Fig. 7). These changes in internal properties as a function of M_{env} can help to explain the trends in the HR diagram as a function of M_{env} .

The right panel of Fig. 5 shows a zoom-in of Regime II in the HR diagram. For $M_{\text{env}} < 2.5M_{\odot}$, T_{eff} decreases with increasing M_{env} . It reaches a minimum of $T_{\text{eff}} = 3380\text{K}$ at $M_{\text{env}} = 2.5M_{\odot}$ and increases with increasing M_{env} for $M_{\text{env}} > 2.5M_{\odot}$. Conversely, the radius increases with M_{env} to a maximum at $M_{\text{env}} = 2.5$ and then decreases with further increasing M_{env} (Fig. 6). The value of T_{eff} is affected by two factors in this regime. Firstly, the effect of opacity

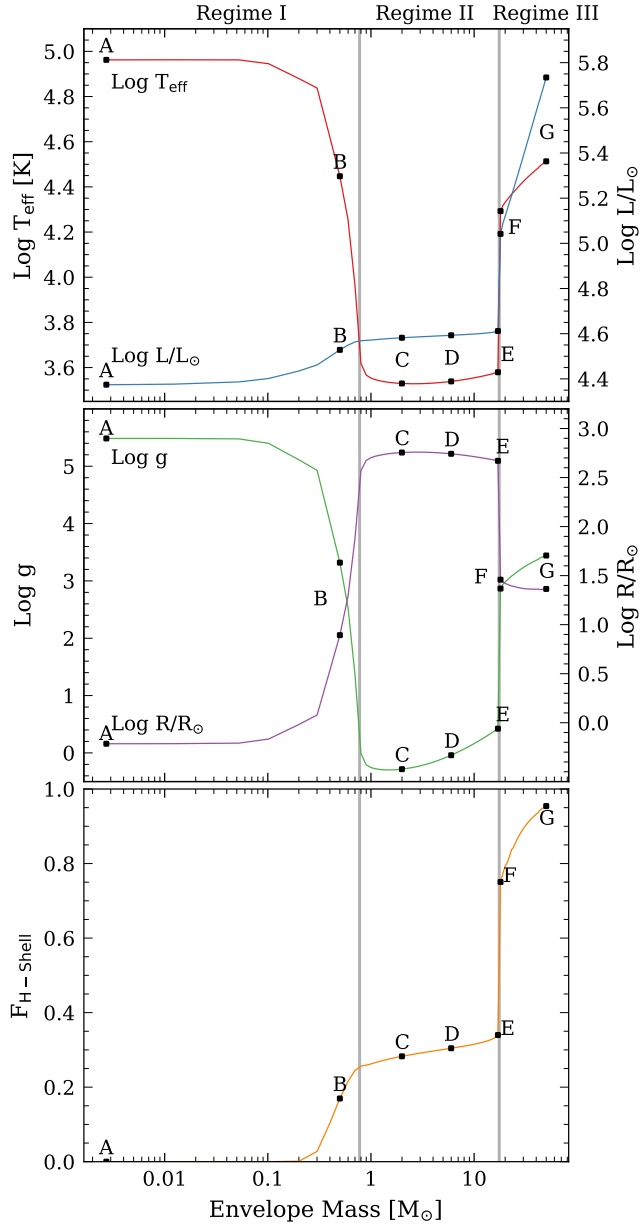


Figure 6. *Upper Panel:* Effective temperature (red curve) and luminosity (blue) as a function of M_{env} for the same models as in Fig. 5 (a constant He-Core mass of $4.1M_{\odot}$, $Y_c = 0.50$ and envelope mass varying from $0-50M_{\odot}$). Models A – G from Fig. 5 are indicated with black dots and labelled. *Middle Panel:* Surface gravity, $\log g$ and the stellar radius as a function of envelope mass for the same models as in the upper panel. *Lower Panel:* Proportion of the total nuclear energy that is produced by the H-burning shell as a function of envelope mass for the same models as in the upper panel.

increases with increasing M_{env} because there is more material in the envelope. This produces a larger radius and lower T_{eff} . Secondly, as M_{env} and $F_{\text{H-shell}}$ increases, the interior temperature profile changes and a larger mass of material is convective (Fig. 7). For stars on the Hayashi track, we expect the stellar radius to decrease with increasing mass (Eggleton 2006), resulting in a higher T_{eff} . The combination of these factors causes T_{eff} to decrease to a minimum and subsequently increase.

For a given M_{core} and Y_c , our models show that the surface

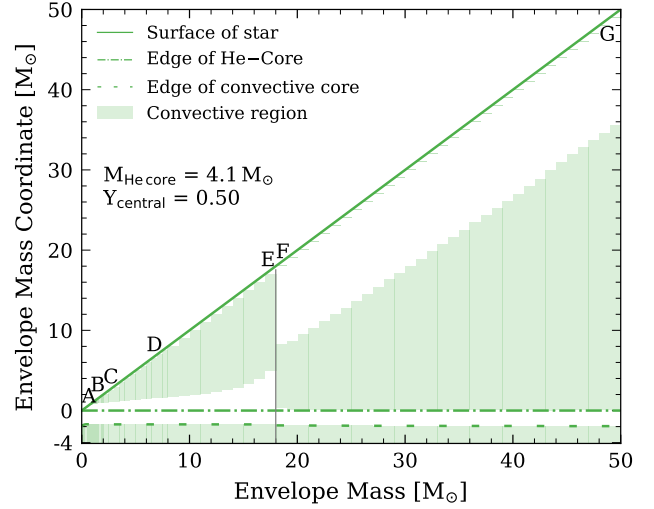


Figure 7. Kippenhahn-like diagram for the models in Figs. 5 and 6 with the envelope mass on the x-axis and the envelope mass coordinate on the y-axis, where 0 corresponds to the edge of the He-core and -4.1 corresponds to the centre of the $4.1M_{\odot}$ core. The convective regions are shaded in green and the boundary of the convective core, the He-core and the surface of the star are indicated with dashed, dash-dot, and solid lines respectively. A grey vertical line indicates the transition between Regimes II and III. Moving from left to right in this figure corresponds to increasing envelope mass.

properties of a RSG change very little over a wide range of envelope masses (Figs. 5, 6, 9, 10). For example, for $M_{\text{core}} = 4.1M_{\odot}$, as M_{env} increases from 2 to $17M_{\odot}$, the value of T_{eff} increases from 3390 K to 3800 K and the luminosity increases from $\text{Log}(L/L_{\odot}) = 4.58$ to 4.61 (Fig. 5). This means that there is a lot of degeneracy in the value of a stellar mass derived from a particular luminosity and T_{eff} for RSGs.

Our models indicate that the minimum envelope mass required to produce a RSG with $T_{\text{eff}} < 5000$ K is $M_{\text{env}} = 0.6M_{\odot}$ for $M_{\text{core}} = 1.9M_{\odot}$ and $M_{\text{env}} = 1.7M_{\odot}$ for $M_{\text{core}} = 8.9M_{\odot}$. In addition, they show that over a wide range of M_{core} , the minimum T_{eff} and maximum radius of a RSG occurs for a core mass ratio of $M_{\text{core}}/M_{\text{total}} \approx 0.60$.

Although we only plot the convective regions for models with one core mass ($M_{\text{core}} = 4.1M_{\odot}$) in Fig. 7, our models show that the mass of the convective region in the envelope depends only on M_{env} and is independent of M_{core} for a wide range of core masses, from $\sim 2 - 7M_{\odot}$.

4.1.3 Transition between Regime II and III

As we keep increasing M_{env} , we find a bi-stability in the solution of the stellar structure equations at an envelope mass of $M_{\text{transition}} = 17.532M_{\odot}$ (the exact value depends on the input physics). For $M_{\text{env}} < M_{\text{transition}}$, the star has a RSG structure with a radiative H-burning shell and a convective envelope (Figs. 7 and 8). As M_{env} increases towards $M_{\text{transition}}$, the pressure and temperature in the H-burning shell increase. This is accompanied by slightly increased nuclear energy generation in the H-burning shell (comparing models D and E in Fig. 8). At $M_{\text{transition}}$, the base of the envelope becomes unstable to convection due to the increased H-shell nuclear burning and the solution of the stellar structure changes. For $M_{\text{env}} > M_{\text{transition}}$, the star is more condensed and hotter, with a convective H-burning shell and a radiative envelope (see Fig. 7 and compare models E

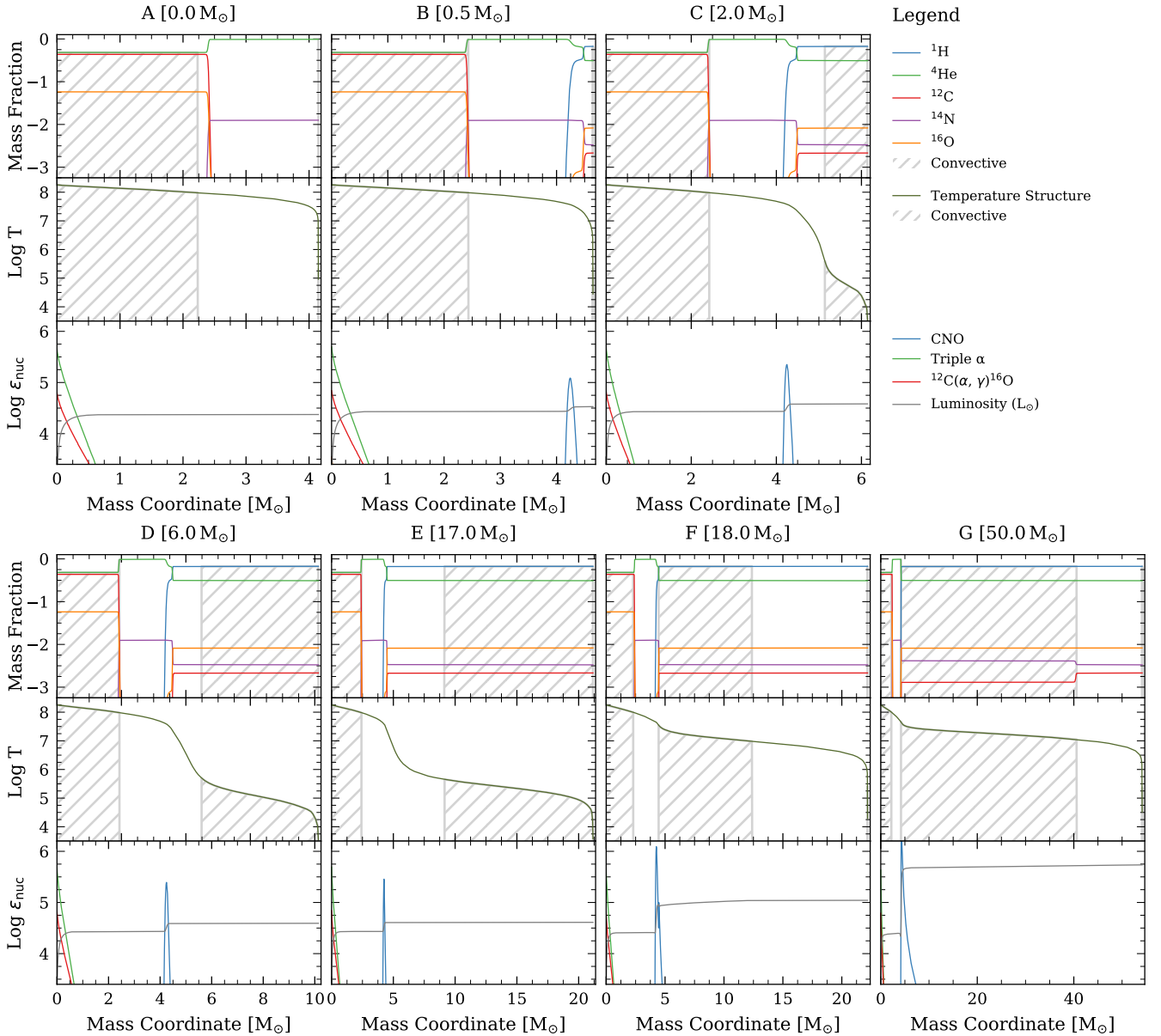


Figure 8. Internal structure of models from points labelled A to G in Figs. 5 and 6. The models have $M_{\text{core}} = 4.1 M_{\odot}$ and $Y_{\text{c}} = 0.50$. The values of M_{env} are indicated above each sub-figure. The convective regions are hashed in the upper and middle panels. The upper panels show the internal abundance profile of H (blue), He (green), C (red), N (purple) and O (orange). The middle panels show the internal temperature structure (solid line). The lower panels show $\log \epsilon_{\text{nuc}}$ in units of $\text{erg g}^{-1} \text{s}^{-1}$ for different reactions, and $\log L$, in units of L_{\odot} .

and F in Fig. 8). Although we have only included structure models at intervals of $1 M_{\odot}$ in Figs. 5, 6 and 7, we observe in our paused models that the star ‘jumps’ from a RSG solution to a BSG solution with no change in mass.

4.1.4 Regime III – High Envelope Mass (Models F and G)

For $M_{\text{env}} \geq 18 M_{\odot}$, our models present a hot, convective H-shell above the He-core and a radiative envelope (models F and G). The presence of a convective region at the base of the envelope results in a modified internal structure with a greatly increased temperature and nuclear energy generation rate in the H-shell. This increased energy production in the H-shell causes a much higher surface luminosity

as compared to models with lower M_{env} in Regime II. The modified structure of the envelope also results in a much smaller stellar radius and a higher T_{eff} compared to Regime II.

The energy generation of models in Regime III is dominated by H-shell burning (see Fig. 6 and energy generation profiles in Fig. 8). More than 75 per cent of the total nuclear energy generation occurs in the H-shell, compared to Regime II stars which have $F_{\text{H-shell}} \sim 0.30$. The mass of the region that is convective increases with increasing M_{env} (Fig. 7). For $M_{\text{env}} = 50 M_{\odot}$ (model G), the envelope dominates the structure and surface properties of the star. The value of $F_{\text{H-shell}} \sim 0.90$ and the star has a similar structure to a core-H burning star but with a $4.1 M_{\odot}$ He-core in the centre. Regime III stars will appear as blue stars in the HR diagram with

$\log g$ of 1.8 – 3.9 dex. Models with lower core masses can produce blue stars with lower values of $\log g$. Some may resemble OB-type stars and others may resemble blue supergiants.

4.2 Effect of Core Mass

We now discuss stellar structure models with M_{core} ranging from 1.9 to $8.9M_{\odot}$, M_{env} ranging from 0.0 to $50.0M_{\odot}$, and Y_c of 0.50 (corresponding to the middle of core-He burning).

We plot these models in the HR diagram in Fig. 9a, and Fig. 10a shows the effect of M_{env} on T_{eff} for models with the same M_{core} and $Y_c = 0.50$. Qualitatively, models with $M_{\text{core}} < 7M_{\odot}$ show similar trends as a function of M_{env} as the model with $M_{\text{core}} = 4.1M_{\odot}$ (Sec. 4.1). We discuss these models below and examine models with $M_{\text{core}} > 7M_{\odot}$ in Sec. 4.2.1.

For models with $M_{\text{env}} \lesssim 0.5M_{\odot}$, the value of T_{eff} increases with M_{core} at constant M_{env} (Fig. 10a). This is due to an increase in luminosity with M_{core} at constant M_{env} , mostly due to higher energy generation in the He-core. For some models, there is also an increase in energy generation in the H-Shell with increasing M_{core} at constant M_{env} , which also contributes to the higher luminosity.

As the envelope mass increases from 0.1 to $1M_{\odot}$, the value of T_{eff} decreases sharply. This is due to the increasing effect of opacity with increasing M_{env} . The value of M_{env} at which T_{eff} begins to decrease increases with M_{core} (Fig. 10a). Additionally, the rate of decrease of T_{eff} as a function of M_{env} increases with M_{core} . The value of T_{eff} depends on the structure of the envelope and, in particular, on the presence and mass of any convective regions in the outer envelope. Models with higher M_{core} can support a higher M_{env} before the outer envelope becomes convective. This allows the envelope to remain compact (i.e. higher T_{eff}) up to a higher M_{env} .

For intermediate envelope masses from ~ 1 to $10M_{\odot}$, models with higher M_{core} have lower T_{eff} for the same M_{env} (Fig. 10a). Models with higher M_{core} have more extended, lower density envelopes, larger radii which results in a lower T_{eff} .

For each value of M_{core} , the location of the bi-stability of the stellar structure equations at the transition between Regimes II and III is indicated in Fig. 10a by dashed lines. At this point, the solution of the stellar structure transitions from a RSG structure with a convective envelope and radiative H-shell to a structure with a radiative envelope and a convective H-shell. The value of M_{env} at which the transition occurs increases with M_{core} . Models with higher M_{core} are able to support a higher M_{env} before the base of the envelope becomes unstable to convection.

Models with higher envelope mass generally converge towards a similar T_{eff} as a function of M_{env} , independent of M_{core} . In this regime, $\gtrsim 80$ per cent of the mass of the star is contained in the envelope and the surface properties are dominated by the nature of the H-shell burning, which depends mostly on M_{env} .

To assess the relative contributions of the core and the envelope to the overall structure of the star, we compute the fraction of the total nuclear energy that is generated in the H-shell ($F_{\text{H-shell}}$) as a function of M_{env} for models with constant M_{core} (Fig. 10c). In all models, the value of $F_{\text{H-shell}}$ is ≈ 0 for $M_{\text{env}} \lesssim 0.1M_{\odot}$. For stars with these envelope masses, very little burning takes place in the H-shell. As the value of M_{env} increases from $\sim 0.1 - 1M_{\odot}$, $F_{\text{H-shell}}$ increases sharply from 0 up to $F_{\text{H-shell}} \approx 0.1 - 0.3$ for $M_{\text{env}} = 1M_{\odot}$. As M_{env} further increases, the star must respond to support the extra mass. It does this by producing more energy in the H-shell. For models with M_{env} of 1 – 10, the value of $F_{\text{H-shell}}$ increases only slightly (by a factor of ~ 0.25) over a large range of M_{env} (a factor of ~ 10). The value of $F_{\text{H-shell}}$ decreases with M_{core}

at constant M_{env} (Fig. 10c). The luminosity generated in the core and in the H-shell both increase with increasing M_{core} at constant M_{env} . However, the luminosity generated in the core increases at a higher rate as a function of core mass than the H-shell (see Sec. 4.2.2 and Fig. 11). As a consequence, for models with higher M_{core} , a lower fraction of the overall energy comes from the H-shell.

For models in Regime III (high envelope mass), > 70 per cent of the total energy production occurs in the H-shell (Fig. 10c). The envelope has a structure similar to a massive core-H burning star with a nuclear burning region at the base, and a radiative outer region. The structure of the star is dominated by the H-shell burning at the base of the envelope, and the energy generated in the H-shell increases with increasing M_{env} .

In Fig. 10a, c, we see that the bi-stability between RSG structures and more luminous, blue stars occurs over a very wide range of M_{env} for different M_{core} . To further explore this transition, we plot T_{eff} and $F_{\text{H-shell}}$ as a function of the core mass ratio, i.e. M_{core} divided by total mass (Fig. 12a, c). Moving from left to right in this figure corresponds to increasing envelope mass.

In Fig. 12a, T_{eff} shows similar trends as a function of $M_{\text{core}}/M_{\text{total}}$ for each M_{core} . The value of T_{eff} decreases sharply from a core mass ratio of 1.0 to about 0.8. For core mass ratios $\approx 0.8 - 0.2$, most models have a RSG structure (Regime II). For models with $M_{\text{core}} < 7M_{\odot}$, the transition from Regime II to III occurs at a core mass ratio of ≈ 0.2 . We can also see the different behaviour of models with $M_{\text{core}} > 7.0M_{\odot}$, the value of T_{eff} decreases much more slowly than models with lower M_{core} .

Looking in more detail at Fig. 10a, we notice that for models with $M_{\text{core}} \lesssim 3M_{\odot}$ and very high envelope masses of $M_{\text{env}} \approx 20 - 50M_{\odot}$, there are some small sharp increases in T_{eff} . This is due to a small amount of convective mixing of material from the edge of the He-core into the envelope for some models with particularly extreme core mass ratios. The mixing occurs only for some models with a core mass ratio of $M_{\text{core}}/M_{\text{total}} \lesssim 0.15$ and it results in a slight decrease in M_{core} and slight increase in M_{env} .

Our *SNAPSHOT* models indicate that the maximum core mass ratio that a RSG can have increases with increasing He-core mass. We note that [Eggleton et al. \(1998\)](#) finds a maximum allowed core mass ratio of ≈ 0.64 for composite polytropic models of red giants, which is consistent with the trend as a function of M_{core} that we observe in our models.

4.2.1 Models with $M_{\text{core}} > 7M_{\odot}$ and $Y_c = 0.50$

These models exhibit qualitatively different behaviour to models with $M_{\text{core}} < 7M_{\odot}$. Unlike models with lower M_{core} , they do not easily develop an outer convective envelope. Small convective shells are formed in the envelope for intermediate $M_{\text{env}} \approx 6 - 20$. The location and mass of the convective shells in the envelope affect the radius R and hence T_{eff} . These cause the small ‘bumps’ visible for models with $M_{\text{core}} = 8.0$ and $8.4M_{\odot}$ in Fig. 10c. Interestingly, models with $Y_c = 0.01$ and $M_{\text{core}} > 7M_{\odot}$ do produce a convective envelope, suggesting that whether or not a star with a given core produces a RSG may depend on Y_c .

The value of M_{env} at which models with $M_{\text{core}} > 7M_{\odot}$ form a convective H-burning shell with a radiative outer envelope is much lower than the models with $M_{\text{core}} = 5.7, 6.0$ and 6.9 . This is the opposite to the trend for lower core masses. The increase in $F_{\text{H-shell}}$ as a function of M_{env} is different for these core masses as well.

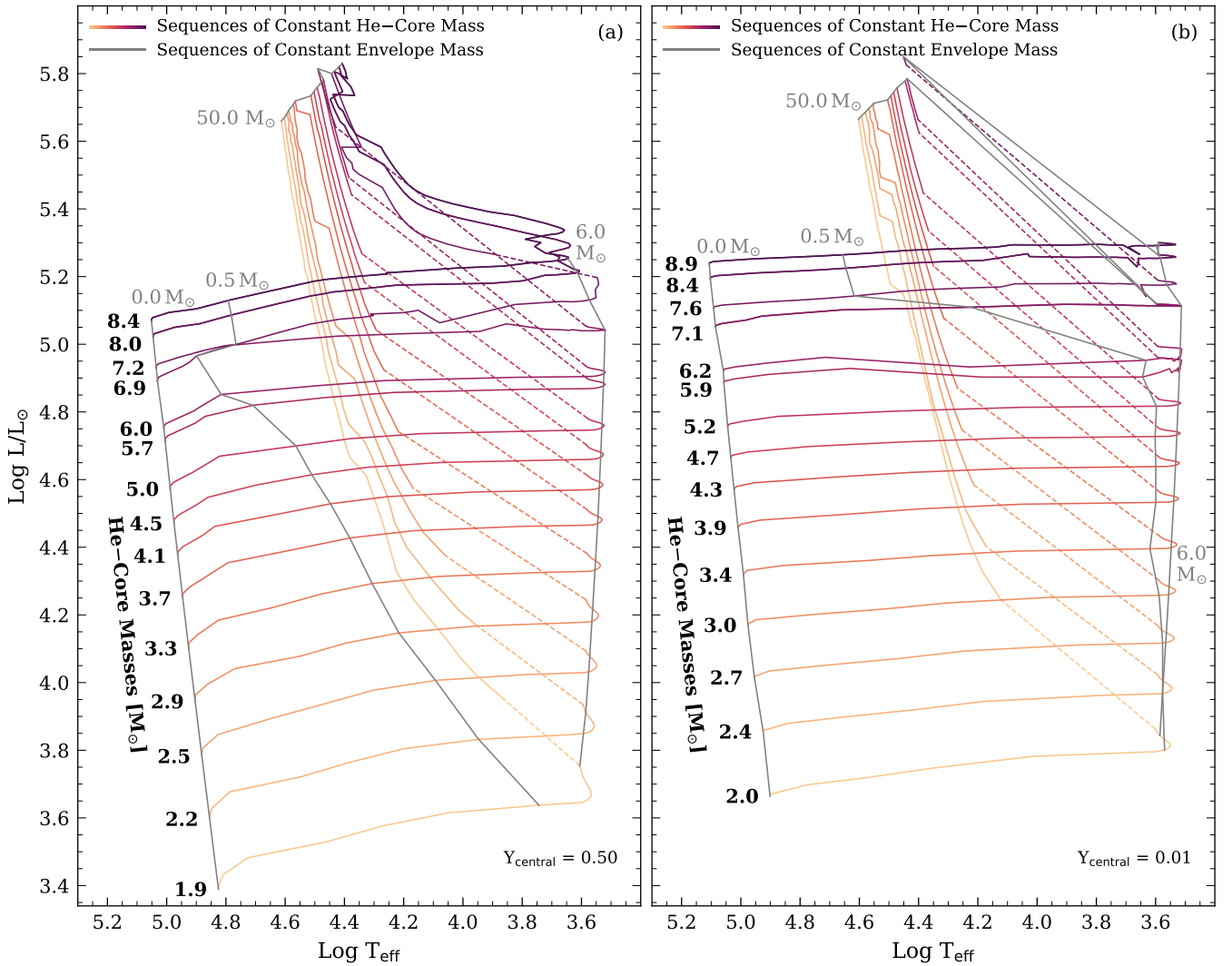


Figure 9. *Left Panel:* Coloured lines indicate constant He-core mass, constant $Y_c = 0.50$ and envelope masses varying from 0.0 to $50.0 M_\odot$ (colours indicate different He-core masses). The He-core masses are indicated in bold along the left-hand side. We also plot four lines of constant envelope mass and varying He-core mass in grey, with the envelope mass in M_\odot indicated in grey text above each line. As in Fig. 5, the dashed coloured lines indicate a transition between two stable solutions of the stellar structure equations. *Right Panel:* Same as left panel but for models with $Y_c = 0.01$.

4.2.2 Effect of Core Mass on H-Shell

The grey lines in Fig. 9a indicate that the surface luminosity increases with M_{core} for constant M_{env} and Y_c . This is not unexpected, as a higher mass core is typically hotter, can generate more energy and produce a higher surface luminosity. Many authors have provided relationships between the luminosity and M_{core} for core-He burning stars (e.g., Eggleton et al. 1989; Tout et al. 1997; Hurley et al. 2000).

Our grid of SNAPSHOT models allows us to test the separate contributions from the core and H-shell to the luminosity. In Fig. 11, we plot the surface luminosity, the luminosity of the He-core and the luminosity of the H-shell against M_{core} for a set of models with $M_{\text{env}} = 3.0 M_\odot$ and $Y_c = 0.50$ and M_{core} from $2 - 9 M_\odot$. As we observed in Fig. 9, the surface luminosity increases with M_{core} for constant M_{env} and Y_c . However the increased luminosity does not all originate in the He-core. The energy produced in both the He-core and the H-shell increases with increasing M_{core} . The value

of M_{core} modifies the temperature structure in the H-shell in two ways. Firstly, the temperature of the H-shell increases (by a small amount) with M_{core} , because the higher mass He-cores are hotter and produce a higher temperature just above the core. Secondly, the mass of the region in which significant energy generation takes place increases. These two changes result in hotter, higher mass H-shells and higher nuclear energy generation rates in the H-shell.

4.3 Effect of Core Composition

Our grid of SNAPSHOT stellar structure models also allows us to isolate the effect of the core composition on the surface properties of the star, independent of the effects of the core mass and envelope mass. This analysis is difficult to accomplish with stellar evolution models, in which the three interior quantities listed above change simultaneously. Models with $Y_c = 0.50$ and 0.01 exhibit qualitative differences in the internal and surface properties (Figs. 10 and 12). In this section, we discuss the effect of the core composition.

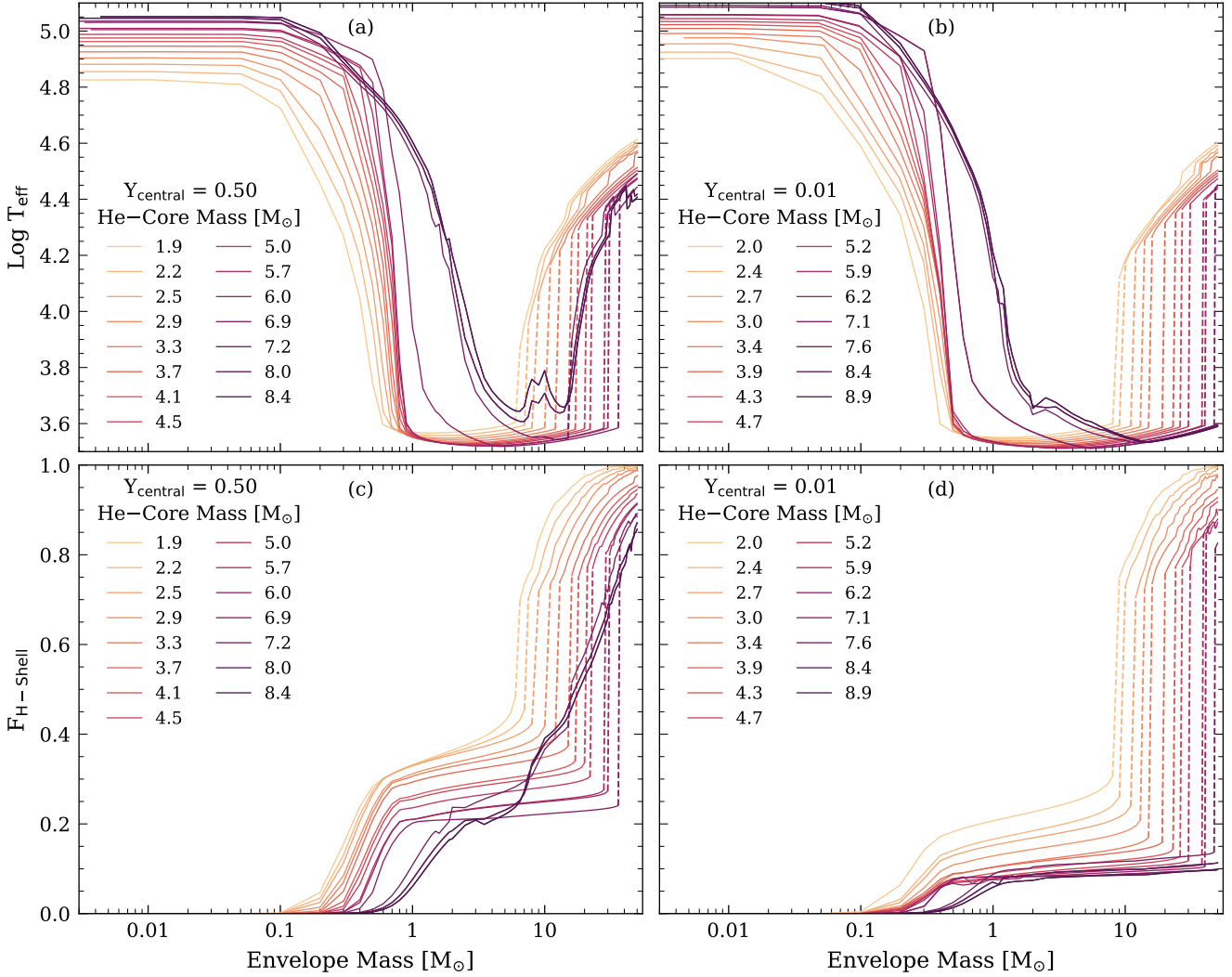


Figure 10. (a): Effective temperature vs. envelope mass for models with constant He-core mass and $Y_{\text{C}} = 0.50$. The dashed lines indicate the bi-stability between Regimes II and III. (b): Same as (a) but for models with $Y_{\text{C}} = 0.01$. (c): The fraction of the total nuclear energy generated in the H-Shell ($F_{\text{H-shell}}$) vs. envelope mass for the same models as in (a). (d): Same as (c) but for models with $Y_{\text{C}} = 0.01$.

Figure 13a, b, c compares the surface luminosity as function of M_{core} at constant M_{env} for core compositions of $Y_{\text{C}} = 0.50$ (dashed line) and $Y_{\text{C}} = 0.01$ (solid line). The models in panel A have $M_{\text{env}} = 0M_{\odot}$. For these models, the surface luminosity is higher for models with $Y_{\text{C}} = 0.01$ than for $Y_{\text{C}} = 0.50$. This is due to the higher mean molecular weight of the core (μ_{core}) for models with $Y_{\text{C}} = 0.01$ compared to 0.50. For the same core mass, a higher μ_{core} results in a higher central temperature, T_{central} , through the equation of state, and hence higher nuclear energy generation rates, ϵ_{nuc} , in the core. As these models have no H-envelope, the He-core is the only region of nuclear energy generation. This means that a higher ϵ_{nuc} in the core caused by with higher μ_{core} corresponds to a higher surface luminosity. We find mass-luminosity relationships of $L \propto M^{2.56}$ for $Y_{\text{C}} = 0.50$ and $L \propto M^{2.43}$ for $Y_{\text{C}} = 0.01$. These are consistent with the mass-luminosity relationships found by Langer (1989).

In contrast, for models with $M_{\text{env}} = 3M_{\odot}$, the value of Y_{C} (and thus μ_{core}) does not affect the surface luminosity (Fig. 13b). For these models, there are two regions of nuclear energy generation,

the He-core and the H-shell. The surface luminosity depends on the energy from both of these regions. While a lower Y_{C} corresponds to a higher μ_{core} , T_{central} and ϵ_{nuc} in the core, it does not correspond to a higher surface luminosity. This is because the energy generation in the H-shell decreases with decreasing Y_{C} . To illustrate this, we plot the total luminosity generated in the He-core, L_{core} and the total luminosity generated in the H-shell, $L_{\text{H-shell}}$ (Fig. 14) for models with $M_{\text{env}} = 3M_{\odot}$. Models with $Y_{\text{C}} = 0.50$ and 0.01 are indicated in dashed and solid lines respectively. For the same core mass, the L_{core} is lower for $Y_{\text{C}} = 0.50$ than for $Y_{\text{C}} = 0.01$. In contrast, the $L_{\text{H-shell}}$ is lower for $Y_{\text{C}} = 0.50$ than for $Y_{\text{C}} = 0.01$. These effects nearly cancel out so that the total luminosity at the surface is similar for $Y_{\text{C}} = 0.50$ and 0.01. For example, models with the same values of M_{core} and M_{env} and Y_{C} of 0.50 and 0.01, the luminosity differs by ~ 0.02 dex and T_{eff} differs by ~ 0.007 dex. The same effect is observed for $M_{\text{env}} = 6M_{\odot}$ and for a wide range of envelope masses. This means that changes in the luminosity of a RSG as it evolves are due mostly to changes in M_{core} and not due to changes in Y_{C} or M_{env} .

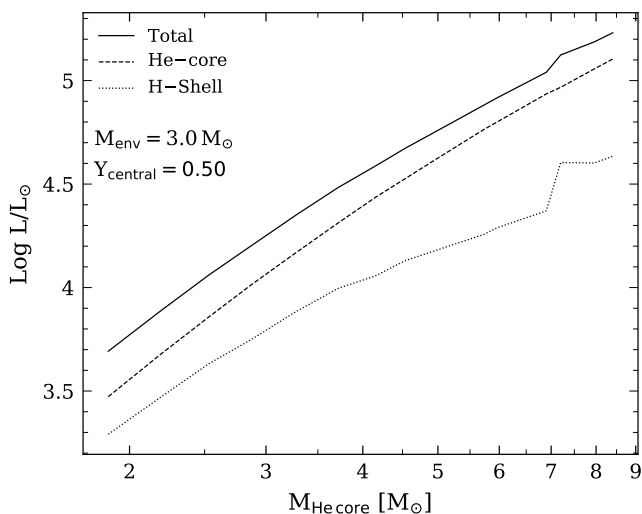


Figure 11. Luminosity vs. core mass for models with the same $Y_c = 0.50$ and $M_{\text{env}} = 3.0M_{\odot}$ and with core masses ranging from $M_{\text{core}} = 2$ to $8M_{\odot}$. The luminosities of the He-core, the H-shell and the total luminosity are indicated by a dash-dot, dotted and solid lines respectively.

We also study the trend in T_{eff} as a function of M_{core} for $Y_c = 0.50$ and 0.01 (Fig. 13d, e, f). For models with no H-envelope (Fig. 13d), the luminosity and T_{eff} are higher for models with $Y_c = 0.01$ compared to $Y_c = 0.50$, while the radius is smaller. For models with $M_{\text{env}} = 3$ and $6M_{\odot}$ and a convective envelope, the value of T_{eff} does not depend on Y_c . This result holds for a wide range of envelope masses. In some cases for $M_{\text{core}} > 7M_{\odot}$, T_{eff} is slightly higher for $Y_c = 0.50$ than 0.01 . This is due to differences in the formation of convective shells in the envelope.

In Fig. 13g, h, i, we plot the radius of the core as a function of the core mass. For a given core mass, models with $Y_c = 0.50$ have cores with larger radii than models with $Y_c = 0.01$. For the same M_{core} , cores with lower values of Y_c must be denser and hotter to produce the same amount of energy to compensate for the decreasing Y_c . This results in a smaller core radius. We also plot the radius of the envelope against the core mass for the same M_{env} (Fig. 13j, k, l). The envelope radius increases with M_{core} at constant M_{env} and Y_c . For the same M_{env} , the mass of the outer envelope that is unstable to convection decreases with increasing M_{core} . At constant M_{env} , envelopes with a more massive outer convective region have lower radii.

5 DISCUSSION

5.1 Uncertain Masses of Red Supergiants

For a RSG with a given luminosity and T_{eff} , our models show that there is a large range of allowed total masses. This means that for all known RSGs in the Galaxy, it is impossible to know the current mass based on the luminosity and T_{eff} alone. For instance, Betelgeuse and VY CMa may have quite different current masses to what we think they do. This degeneracy may be broken with an accurate measure for the surface gravity. However, this quantity is typically derived from evolutionary mass and either angular diameter (if the star can be resolved) or luminosity and T_{eff} in spectroscopic analyses of RSGs, rather than derived based on diagnostics.

The core of a RSG is mostly unaffected of the presence of the

envelope. The luminosity of the core is determined by M_{core} and Y_c , which is the classical result obtained for Helium stars (Maeder & Meynet 1987; Langer et al. 1989). However, the envelope is affected by the core. The energy produced in the H burning shell depends on the temperature profile at the base of the envelope, which in turn depends on M_{core} and Y_c . It contributes 10 – 30 per cent of the total luminosity (for $0.50 > Y_c > 0.01$ and $M_{\text{core}} < 7M_{\odot}$) in such a way that the role of Y_c in the total energy production is almost eliminated. This means that the mass of the RSG envelope does not significantly impact the total luminosity.

Our finding about the uncertain current value of M_{env} of a RSG (and thus total current mass) has several implications for massive star evolution. First, two RSGs at a similar location in the HR diagram may have very different M_{env} and total mass. Second, not knowing the value of M_{env} makes it difficult to estimate the fraction of the envelope that will be lost as the star evolves during He core burning. This has effects on the duration of the plateau in the supernova lightcurve for those stars that are able to retain their H envelope. This is particularly relevant in light of the recent downward revision of the mass-loss rates of RSGs (e.g., Beasor et al. 2020). Our SNAPSHOT models open the possibility that RSGs could have much lower or much higher M_{env} than currently thought, however binary population synthesis models are needed to assess the distribution of M_{env} . The distribution of allowed M_{env} is not flat and based on our current knowledge of single and binary star evolution, some masses are preferred (Zapartas et al. 2019).

This analysis can be extended to RSGs at the end of their lives, which is especially interesting for the fate of the star, supernova light curve properties and the compact remnant mass. Farrell et al. (2020) applied the SNAPSHOT model approach to investigate RSGs at the end of their lives and found that it is not possible to determine the final mass of a red supergiant (RSG) at the pre-supernova (SN) stage from its luminosity L and effective temperature T_{eff} alone. This result applies to RSG progenitors of core collapse supernovae, failed supernovae and direct collapse black holes.

We now turn our attention to the radius and T_{eff} of RSGs. These quantities have significant impact on the morphological appearance of these stars and on the post-explosion properties, such as the early time lightcurve (e.g., Dessart et al. 2013; González-Gaitán et al. 2015; Morozova et al. 2015, 2018; Hillier & Dessart 2019). Because of their deep convective envelopes, RSGs are also ideal laboratories for studying the properties of convective mixing. For instance, it is well known that the T_{eff} of RSGs in stellar models are strongly affected by the choice of mixing length parameter, α_{mlt} (e.g., Henyey et al. 1965; Stothers & Chin 1995; Chun et al. 2018). In the models of Chun et al. (2018), the T_{eff} of RSGs varies by up to ~ 800 K for different choices of α_{mlt} . Our models show that, in addition to convective mixing, different envelope masses produce a variation of up to ~ 400 K for the same core mass. This suggests that when calibrating the mixing length parameter α_{mlt} by using the T_{eff} of RSGs, it may be important to consider that the core and envelope masses may be substantially different to what is predicted by stellar evolution models. Possible processes that would modify M_{core} and M_{env} include convective overshooting on the MS or mass loss during the RSG phase.

Our results about the behavior of the stellar radius as a function of envelope mass are also relevant for RSGs in binary systems, of which there are many observations (e.g., Hansen & M 1944; McLaughlin 1950; Wright 1970; Stencel et al. 1984; Hagen Bauer & Bennett 2014; Harper et al. 2016; Neugent et al. 2018, 2019). When a RSG undergoes RLOF, it often results in non-conservative mass-

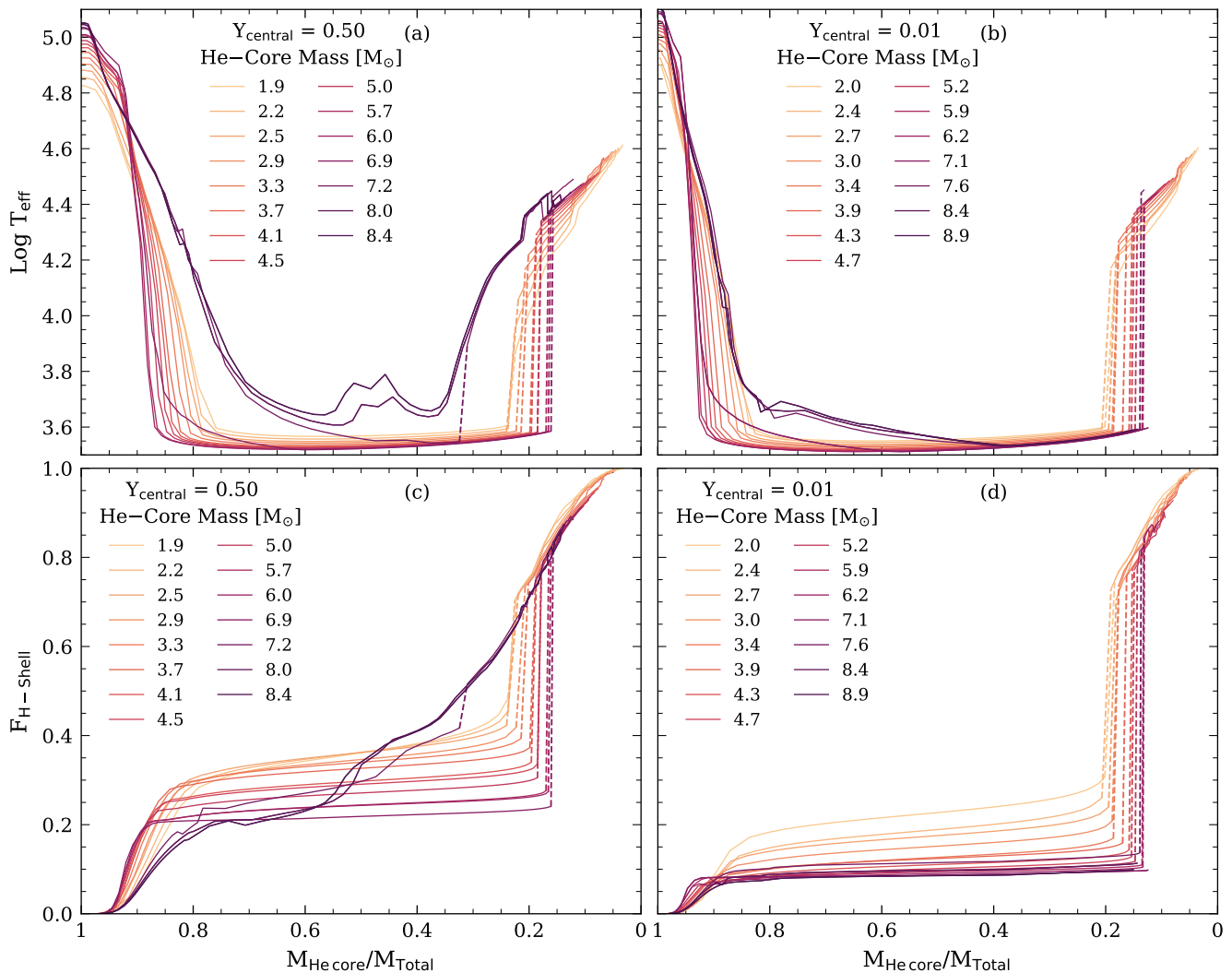


Figure 12. (a): Effective temperature vs. core mass ratio ($M_{\text{core}}/M_{\text{total}}$) for models with constant He-core mass and $Y_{\text{c}} = 0.50$. The dashed lines indicate the bi-stability between Regimes II and III. (b): Same as (a) but for models with $Y_{\text{c}} = 0.01$. (c): The fraction of the total nuclear energy generated in the H-Shell ($F_{\text{H-shell}}$) vs. envelope mass for the same models as in (a). (d): Same as (c) but for models with $Y_{\text{c}} = 0.01$.

transfer. As the star loses mass via RLOF, the radius of the star increases faster than the Roche-Lobe increases (Eggleton 2006).

Our models show that the maximum radius of RSGs occurs for a core mass ratio of ≈ 0.6 . This means that even in thermal equilibrium, as envelope mass is lost from the star, we expect that the envelope will continue to increase in radius until the core mass ratio increases above 0.6. For higher core mass ratios, the radius decreases with decreasing M_{env} and the mass transfer episode may finish.

5.2 Stripped stars

Based on the number of stars in binary systems, we expect a large number of stars to exist that are stripped of their hydrogen-rich envelope (Sana et al. 2012). However, only a small number have actually been observed (e.g., Gies et al. 1998; Groh et al. 2008; Peters et al. 2013; Wang et al. 2017; Chojnowski et al. 2018). This may be due to the presence of companion stars that are brighter at visual wavelengths (Götberg et al. 2018) or as a result of biases

and selection effects (de Mink et al. 2014; Schootemeijer & Langer 2018).

Our results have implications for the detectability of stripped stars. Our results show that the surface properties of stripped stars, in particular the effective temperature, strongly depend on the mass of the envelope left after binary interaction. This will change the flux distribution in different filters, and impact the completeness limit of future observing surveys that will aim to detect those objects.

By interpolating between our SNAPSHOT models, it is possible to determine the allowed values of M_{core} and M_{env} for a given observed luminosity and T_{eff} of a stripped star. Knowledge of the core and envelope masses of stripped stars can provide constraints on the physics of RLOF in binary models. When combined with a mass-loss rate, the values of M_{core} and M_{env} can be used to infer their final fates. Depending on the mass of hydrogen left in the envelope at the end of their evolution, these stripped stars are likely to produce SNe IIb or Ib (Podsiadlowski et al. 1993; Woosley & Weaver 1994; Filippenko 1997; Stancliffe & Eldridge 2009; Gal-Yam 2012; Götberg et al. 2017).

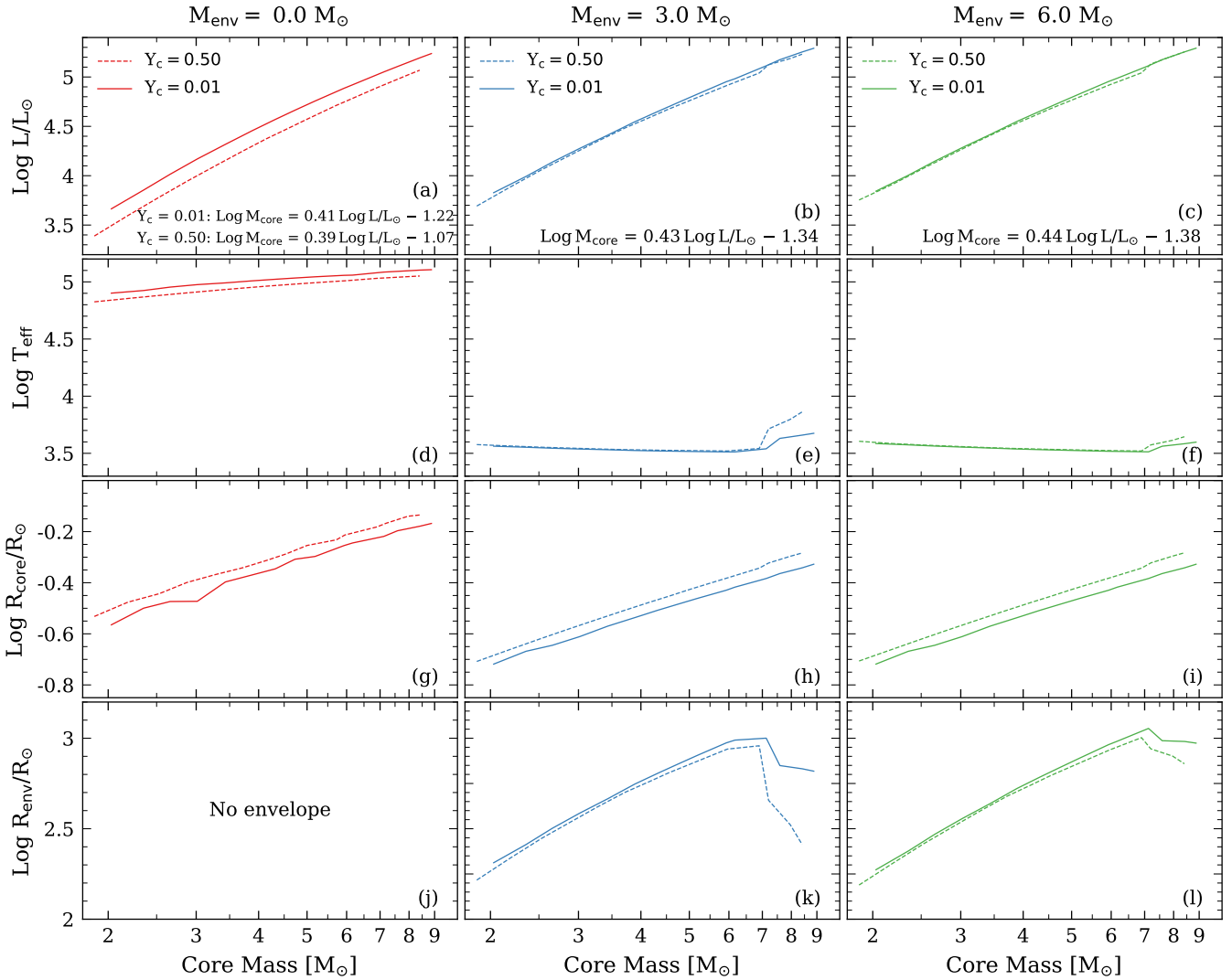


Figure 13. *Left panels (a, d, g, and j):* Surface luminosity, effective temperature, radius of the core and radius of the envelope as a function of core mass for models with no H-envelope. The dashed lines and solid lines indicate models with $Y_c = 0.50$ and $Y_c = 0.01$ respectively. *Middle panels (b, e, h, and k):* Same as left panels but for models with a constant envelope mass of $3M_\odot$ and varying core mass. *Right panels (c, f, i, and l):* Same as left panels but for models with a constant envelope mass of $6M_\odot$ and varying core mass.

Most stripped stars detected so far have low mass, with HD 45166 being the most massive and only detected system within the mass range that can be compared to our models. Based on orbital dynamics, the primary star has a current mass of $4.2 M_\odot$ (Steiner & Oliveira 2005). Spectroscopic analysis using CMFGEN radiative transfer models derived a luminosity of $\log L/L_\odot = 3.75$, T_{eff} of 50 000K and mass-loss rate of $2.2 \times 10^{-7} M_\odot/\text{yr}$ (Groh et al. 2008). Using our models, and assuming $Y_c = 0.50$ (the middle of core-He burning), we derive $M_{\text{core}} = 2.30 \pm 0.15 M_\odot$ and $M_{\text{env}} = 0.15 \pm 0.02 M_\odot$. Taking into account the range of possible values of Y_c from 0.98 to 0.00, we obtain $M_{\text{core}} = 2.30^{+0.35}_{-0.23} M_\odot$ and $M_{\text{env}} = 0.15^{+0.11}_{-0.08} M_\odot$.

This mass is consistent with detailed binary models (e.g., Göteborg et al. 2018). However it is lower than the mass of $4.2 \pm 0.7 M_\odot$ obtained by Steiner & Oliveira (2005). There are several possibilities for this discrepancy. First, it may be due to the assumptions for the secondary star to HD 45166, which is assumed to be $4.8 M_\odot$ based on its B7V spectral type (Steiner & Oliveira 2005). For example, the

secondary star may be out of thermal equilibrium. Assuming our primary mass is correct, the secondary star has a mass of $2.70 M_\odot$ based on the mass ratio derived by Steiner & Oliveira (2005). Secondly, it is possible that the primary star is out of thermal and/or hydrostatic equilibrium, in which case our models would not be applicable. It is also possible, but less likely, that HD45166 is a post core-He burning star, but in this case the derived value of M_{core} and total mass would be even lower. Regardless of the exact mass of HD 45166, its He core is massive enough to explode as a CCSN. We expect that this mass discrepancy is much larger than potential uncertainties in our SNAPSHOT models (see Sec. 5.3.)

The energy generation of core-He burning stripped stars is dominated by M_{core} . For stripped stars with high T_{eff} , a given luminosity and T_{eff} could correspond to a high value of M_{core} and high Y_c or a lower value of M_{core} and low Y_c . For a given luminosity and T_{eff} , most of the uncertainty in the value of M_{core} is due to the degeneracy between M_{core} and Y_c , rather than the observational uncertainty in the luminosity and T_{eff} . For a given T_{eff} , the value

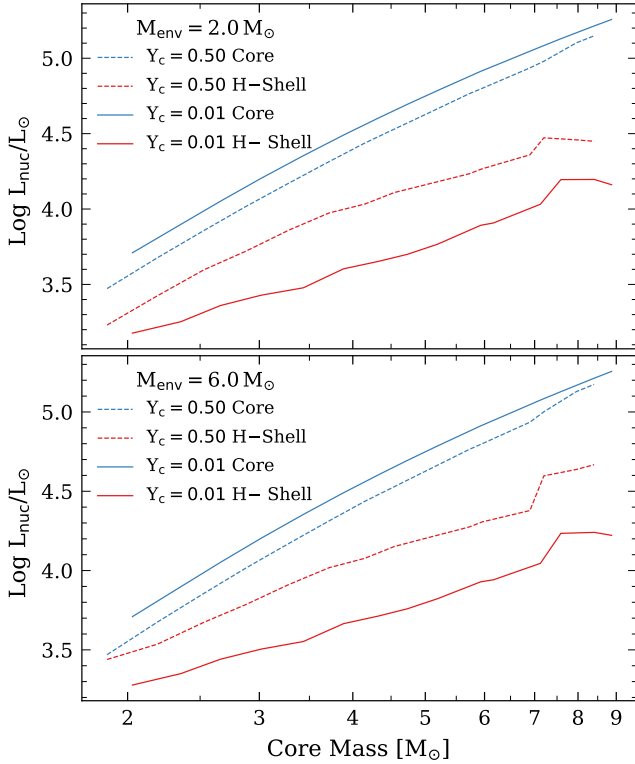


Figure 14. *Upper panel:* Luminosity from the core (blue) and the H-shell (red) as a function of core mass for a constant envelope mass of $3M_{\odot}$ and for $Y_c = 0.50$ (dashed line) and $Y_c = 0.01$ (solid line) – the same models as panels b, e, h, and K in Fig. 13. *Lower panel:* Same as upper panel but for models with a constant envelope mass of $6M_{\odot}$ – the same models as panels c, f, i, and l in Fig. 13

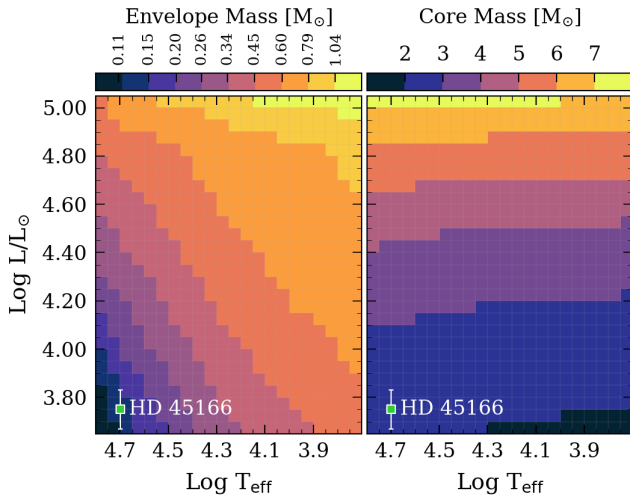


Figure 15. *Left:* Envelope Mass M_{env} that we derive by interpolating between our *SNAPSHOT* models of stripped stars (with $Y_c = 0.50$) for a range of luminosities and T_{eff} . *Right:* Same as *left* but for the Core Mass M_{core} .

of M_{core} and M_{env} increases with increasing luminosity while for a given luminosity, the value of M_{core} increases and M_{env} decreases with increasing T_{eff} . This behaviour is illustrated in Fig. 15, where we show the different values allowed for M_{env} and M_{core} for a given position in the HR diagram.

We will provide an online tool to derive the values of M_{core} , M_{env} of stripped stars and the associated uncertainties based on the luminosity and T_{eff} which we hope will be of great benefit to interpret future observations of stripped stars. When such further observations are available, by deriving the values of M_{core} and M_{env} of a population of stripped stars, and with knowledge of the lifetimes of these burning stages, it may be possible to estimate a mass loss rate for hot, stripped stars.

5.3 Additional Caveats

One of the advantages of studying *SNAPSHOT* stellar structure models is that they are independent of many of the usual sources of uncertainty that affect stellar evolution models. These include mass loss by stellar winds, mass-exchange during a binary interaction, the evolutionary effects of rotation and of convective overshooting. However, our approach is still subject to uncertainties of physical inputs to the models. We discuss these below.

We use Type I and Type II opacities from OPAL (Iglesias & Rogers 1993, 1996) at high temperatures and opacities from Ferguson et al. (2005) at low temperatures. The opacities for H, He, C, N and O are quite well known. Most of the uncertainty arises in the Fe opacities (Bailey et al. 2015) and these can have quite substantial effects on the structure of the star. Changes to the opacities could in some cases systematically shift the T_{eff} of our models.

The equation of state (EOS) used in *MESA* is from OPAL (Rogers & Nayfonov 2002), SCVH (Saumon et al. 1995) and the HELM EOS (Timmes & Swesty 2000). For stars during core-H and core-He burning, the EOS is expected to be relatively accurate (Timmes & Swesty 2000). Therefore, it is likely that any uncertainties associated with the EOS do not have large effects on the models in this grid.

The nuclear reaction rates are a third potential source of uncertainty. The uncertainties in the reactions during the CNO-cycle and in the triple alpha reaction are relatively small, however there is some uncertainty in the rate of $^{12}\text{C}(\alpha, \gamma)^{16}\text{O}$ (deBoer et al. 2017). The effect of any uncertainties associated with these nuclear reaction rates on the *SNAPSHOT* structure models in this work is likely small.

We use *MESA*'s `simple_photosphere` atmosphere boundary condition which applies a simple grey atmosphere. This treatment of the outer boundary is likely appropriate for our models as they are still far from the Eddington limit. Stellar evolution models have shown that the treatment of the outer boundary will have a larger effect on the radius for high mass stars close to the Eddington limit (Langer 1989; Schaerer et al. 1996; Schaerer 1996; Gräfelder et al. 2012; Groh et al. 2014).

All of our models are non-rotating. Massive stars exhibit a range of rotational velocities (Hunter et al. 2008; Huang et al. 2010; Ramírez-Agudelo et al. 2013, 2015; Dufton et al. 2019) and rotation can have an important impact on their evolution (Maeder & Meynet 1987; Meynet & Maeder 2000; Heger et al. 2005; Brott et al. 2011b). However as our models are not evolving, only the hydrostatic effect of rotation could potentially affect the results in this paper. This effect is small, except for fast rotating stars (Maeder & Meynet 2000).

Our models do not take into account the effect of internal or surface magnetic fields. However, as we consider only structure models in this paper, the evolutionary effects of magnetic fields on mass-loss rates and angular momentum loss rates (e.g., [Meynet et al. 2011](#); [Keszthelyi et al. 2019](#)) likely do not have significant effects on our analysis. The hydrostatic effect of a magnetic field may have a small impact on the structure and energy transport inside the star, but further work is needed to properly address this effect.

We adopt a mixing length parameter of $\alpha_{\text{mlt}} = 1.82$ for the models in this paper. This value was calibrated based on solar observations by [Choi et al. \(2016\)](#). The choice of α_{mlt} can significantly affect the T_{eff} of RSGs. A higher value of α_{mlt} produces RSGs with lower values of T_{eff} . [Chun et al. \(2018\)](#) compared observations of RSGs to stellar evolution models and found that models $\alpha_{\text{mlt}} = 2$ or 2.5 best reproduced the observations.

In this paper, we select 3 key structural properties, i.e. the M_{core} , M_{env} and core composition in terms of X_c and Y_c , and draw connections with the surface properties. However, these structural properties clearly do not fully describe the interior of a star. Other structural properties, such as different abundance profiles in the envelope due to mixing, mass-accretion from a companion or mergers, may have important effects on the surface properties. For example, [Schootemeijer et al. \(2019\)](#) studied the properties and lifetimes of red and blue supergiants in terms of the H-gradient outside the He-core.

Most stars are in hydrostatic and in thermal equilibrium, that is the radial acceleration is zero and that the luminosity emitted at the surface is equal to the rate of energy production by nuclear reactions in the interior. The method described in this paper to construct SNAPSHOT stellar structure models is only appropriate for stars that are in hydrostatic and thermal equilibrium. It is not possible to construct stellar structure model after the end of core-He burning or close to core-collapse as the envelope is out of thermal equilibrium during these stages. The latest stage in the evolution of a star at which it is possible to consistently construct SNAPSHOT structure models is the end of core-He burning.

5.4 Directions for Future Work

Our SNAPSHOT model approach provides the foundation for several possible directions for future work. We briefly outline some of them below.

In this work, we studied models at solar metallicity. Our analysis can be extended for stars at lower metallicity. Several papers have studied the evolution of stars at different metallicities (e.g., [Brott et al. 2011a](#); [Yoon et al. 2012](#); [Szécsi et al. 2015](#); [Choi et al. 2016](#); [Groh et al. 2019](#)). SNAPSHOT models may help us to understand the effects of metallicity on stellar structure, independent of the evolutionary effects of mass loss, rotation and binaries.

While we cannot compute stellar structure models in hydrostatic and thermal equilibrium at the end of central carbon burning (due to the fact that the envelopes are out of thermal equilibrium at this point), the structure models at the end of core-He burning could be evolved to the end of core-C burning to study the surface properties of supernova progenitors. Furthermore, these models could be evolved to core-collapse and exploded in 1-D explosion models, similar to the approach of [Ugliano et al. \(2012\)](#), [Sukhbold et al. \(2016\)](#) and others. This would allow us to systematically study the appearance of supernovae as a function of progenitor structure.

SNAPSHOT stellar structure models may help to shed light on what affects the T_{eff} of post-main sequence massive stars. As well as insight into stellar evolution, understanding which stars live as

BSGs and RSGs has implications for the number of ionising photons emitted by stars, the kinetic energy feedback to a galaxy and chemical yields from massive stars.

Our SNAPSHOT models will benefit greatly from current and future astero-seismological results for massive stars, such as from the TESS and PLATO space missions. In particular, improvements in our understanding of stellar structure from astero-seismological studies ([Buldgen et al. 2015](#); [Eggenberger et al. 2017](#); [Aerts et al. 2019](#)) could be implemented in our models in the future. SNAPSHOT stellar structure models could also be applied to low mass stars which benefit from larger observational samples.

Gravitational wave observations of double neutron star mergers ([Abbott et al. 2017a,b](#)) and double black hole mergers ([Abbott et al. 2016](#)) have opened a new frontier in astrophysics. These observations have provided new insights into compact objects and the endpoints of massive stars. Our SNAPSHOT stellar structure models could be used to study the mass function of compact remnants and the boundaries between white dwarfs and neutron stars, and neutron stars and black holes.

6 CONCLUSIONS

In this paper, we introduced our SNAPSHOT technique to construct stellar structure models in hydrostatic and thermal equilibrium. We then applied our approach to study the surface properties of core-H and core-He burning stars with a range of core and envelope masses and core compositions.

(i) We find that there is a limited range of core masses, envelope masses and core compositions that can form core-H burning structures in hydrostatic and thermal equilibrium. We quantified the relationship between the convective core mass and the total mass for different central H mass fractions.

(ii) Over a wide range of He-core masses ($M_{\text{core}} \approx 2 - 9M_{\odot}$), core-He burning stars show similar trends in luminosity and T_{eff} as a function of the core mass ratio ($M_{\text{core}}/M_{\text{total}}$).

(iii) Our models with core mass ratios of $M_{\text{core}}/M_{\text{total}} > 0.8$ correspond to stripped stars produced as a consequence of significant mass loss or binary interaction. They show that T_{eff} has a strong dependence on M_{env} (due to the increased effect of opacity from the H-rich envelope), M_{core} and the core composition. When a large observational sample of stripped stars becomes available, our results can be used to constrain their M_{core} , M_{env} , mass-loss rates and the physics of binary interaction. Our models also show that the surface luminosity of these stars increases slightly with increasing envelope mass due to increased energy generation in the H-shell, in which 0 – 25 per cent of the total nuclear energy is generated.

(iv) Stars with $M_{\text{core}}/M_{\text{total}}$ from 0.2 to 0.8 have convective outer envelopes, low T_{eff} and will appear as RSGs. They exhibit a small variation in luminosity (0.02 dex) and T_{eff} ($\sim 400\text{K}$), over a wide range of envelope masses ($\sim 2 - 17M_{\odot}$). This means that given current uncertainties in the physics driving stellar evolution, it is not possible to derive red supergiant masses from luminosities and T_{eff} alone. In these stars, we find that 10 to 35 per cent of the nuclear energy generation occurs in the H-shell, depending on the core mass (M_{core}) and the central He mass fraction (Y_c). We derive the following relationship between M_{core} and the total luminosity of a red supergiant during core He burning: $\log M_{\text{core}} \approx 0.44 \log L/L_{\odot} - 1.38$.

(v) At $M_{\text{core}}/M_{\text{total}} \approx 0.2$, our models exhibit a bi-stability in the solution of stellar structure equations. The solution of the stellar structure equations switches from a convective outer envelope with

a radiative H-burning shell to a radiative outer envelope with a convective H-burning shell. This switch is accompanied by a large increase in luminosity and T_{eff} .

(vi) Stars with greater than 80 per cent of the mass in the H-envelope correspond to mass gainers and merger products. The luminosity and T_{eff} of these stars are dominated by properties of the envelope. More than 70 per cent of their energy generation comes from the H-shell. Some of these stars may resemble OB-type stars and others may resemble blue supergiants.

(vii) For a constant envelope mass and He-core composition, the total energy produced in the H-shell increases with increasing core mass. This is because higher mass cores produce a larger, hotter H-burning shell which increases CNO burning in the shell. Despite this, the fraction of energy produced in the H-shell decreases with increasing core mass. This is because higher mass cores are hotter and produce more energy which means the stars requires less energy generation in the H-shell to support an envelope of a given mass.

(viii) For core-He burning stars with the same core mass (M_{core}) and envelope mass (M_{env}), the luminosity of the He-core increases with decreasing Y_{C} , due to the effect of the mean molecular weight of the core (μ_{core}). For stars with envelope masses of $M_{\text{env}} \lesssim 1M_{\odot}$, the increased luminosity of the He-core results in an increased surface luminosity. However, for stars with $M_{\text{env}} \gtrsim 1M_{\odot}$, the increased luminosity in the He-core is nearly cancelled out by a corresponding decrease in the luminosity of the H-shell. As a result, in these stars the luminosity at the surface is not strongly affected by μ_{core} , and is set by M_{core} and M_{env} .

ACKNOWLEDGEMENTS

We thank the referee, Prof. Alex de Koter, for his detailed review and comments that improved our manuscript. We would like to thank the MESA (Modules for Experiments in Stellar Astrophysics) collaboration for making their software package freely available to the astrophysics community (Paxton et al. 2011, 2013, 2015, 2018, 2019). E.F. would like to thank GG for helping to create Fig. 1 and acknowledges funding from IRC Project 208026, Award 15330. GM, SE, and CG have received funding from the European Research Council (ERC) under the European Union's Horizon 2020 research and innovation program (grant agreement No 833925, project STAREX).

REFERENCES

- Abbott B. P., et al., 2016, *Phys. Rev. Lett.*, 116, 061102
 Abbott B. P., et al., 2017a, *Phys. Rev. Lett.*, 119, 161101
 Abbott B. P., et al., 2017b, *ApJ*, 848, L12
 Aerts C., et al., 2019, *A&A*, 624, A75
 Aguilera-Dena D. R., Langer N., Moriya T. J., Schootemeijer A., 2018, *ApJ*, 858, 115
 Almeida L. A., et al., 2017, *A&A*, 598, A84
 Bailey J. E., et al., 2015, *Nature*, 517, 56
 Beasor E. R., Davies B., 2018, *MNRAS*, 475, 55
 Beasor E. R., Davies B., Smith N., van Loon J. T., Gehrz R. D., Figer D. F., 2020, arXiv:2001.07222 [astro-ph]
 Belczynski K., Kalogera V., Bulik T., 2002, *ApJ*, 572, 407
 Belczynski K., Kalogera V., Rasio F. A., Taam R. E., Zezas A., Bulik T., Maccarone T. J., Ivanova N., 2008, *ApJ Supplement Series*, 174, 223
 Boian I., Groh J. H., 2018, *A&A*, 617, A115
 Braun H., Langer N., 1995, *A&A*, 297, 483
 Brott I., et al., 2011a, *A&A*, 530, A115
 Brott I., et al., 2011b, *A&A*, 530, A116
 Buldgen G., Reese D. R., Dupret M. A., 2015, *A&A*, 583, A62
 Castro N., Fossati L., Langer N., Simón-Díaz S., Schneider F. R. N., Izzard R. G., 2014, *A&A*, 570, L13
 Chieffi A., Limongi M., 2013, *ApJ*, 764, 21
 Chini R., Hoffmeister V. H., Nasserri A., Stahl O., Zinnecker H., 2012, *MNRAS*, 424, 1925
 Chiosi C., Maeder A., 1986, *ARA&A*, 24, 329
 Choi J., Dotter A., Conroy C., Cantiello M., Paxton B., Johnson B. D., 2016, *ApJ*, 823, 102
 Chojnowski S. D., et al., 2018, *ApJ*, 865, 76
 Chun S.-H., Yoon S.-C., Jung M.-K., Kim D. U., Kim J., 2018, *ApJ*, 853, 79
 Cox J. P., Salpeter E. E., 1961, *ApJ*, 133, 764
 De Beck E., Decin L., de Koter A., Justanont K., Verhoelst T., Kemper F., Menten K. M., 2010, *A&A*, 523, A18
 Dessart L., Hillier D. J., Waldman R., Livne E., 2013, *MNRAS*, 433, 1745
 Dominik M., Belczynski K., Fryer C., Holz D. E., Berti E., Bulik T., Mandel I., O'Shaughnessy R., 2012, *ApJ*, 759, 52
 Dufton P. L., Evans C. J., Hunter I., Lennon D. J., Schneider F. R. N., 2019, *A&A*, 626, A50
 Dunstall P. R., et al., 2015, *A&A*, 580, A93
 Eggenberger P., et al., 2017, *A&A*, 599, A18
 Eggleton P., 2006, *Evolutionary Processes in Binary and Multiple Stars*. Cambridge University Press
 Eggleton P. P., Fitchett M. J., Tout C. A., 1989, *ApJ*, 347, 998
 Eggleton P. P., Faulkner J., Cannon R. C., 1998, *MNRAS*, 298, 831
 Ekström S., et al., 2012, *A&A*, 537, A146
 Eldridge J. J., Stanway E. R., 2009, *MNRAS*, 400, 1019
 Eldridge J. J., Tout C. A., 2004, *MNRAS*, 353, 87
 Eldridge J. J., Izzard R. G., Tout C. A., 2008, *MNRAS*, 384, 1109
 Eldridge J. J., Stanway E. R., Xiao L., McClelland L. A. S., Taylor G., Ng M., Greis S. M. L., Bray J. C., 2017, *Publ. Astron. Soc. Australia*, 34, e058
 Farrell E. J., Groh J. H., Meynet G., Eldridge J. J., 2020, *MNRAS*,
 Ferguson J. W., Alexander D. R., Allard F., Barman T., Bodnarik J. G., Hauschildt P. H., Heffner-Wong A., Tamanai A., 2005, *ApJ*, 623, 585
 Filippenko A. V., 1997, *ARA&A*, 35, 309
 Fragos T., Andrews J. J., Ramirez-Ruiz E., Meynet G., Kalogera V., Taam R. E., Zezas A., 2019, *ApJ*, 883, L45
 Fraser M., et al., 2013, *MNRAS*, 433, 1312
 Fuller J., 2017, *MNRAS*, 470, 1642
 Gal-Yam A., 2012, *Science*, 337, 927
 Gal-Yam A., Leonard D. C., 2009, *Nature*, 458, 865
 Gal-Yam A., et al., 2014, *Nature*, 509, 471
 Garmany C. D., Conti P. S., Massey P., 1980, *ApJ*, 242, 1063
 Georgy C., 2012, *A&A*, 538, L8
 Giannone P., 1967, *Z. Astrophys.*, 65, 226
 Giannone P., Kohl K., Weigert A., 1968, *Z. Astrophys.*, 68, 107
 Gies D. R., Bagnuolo W. G., Ferrara E. C., Kaye A. B., Thaller M. L., Penny L. R., Peters G. J., 1998, *ApJ*, 493, 440
 González-Gaitán S., et al., 2015, *MNRAS*, 451, 2212
 Götzberg Y., de Mink S. E., Groh J. H., 2017, *A&A*, 608, A11
 Götzberg Y., de Mink S. E., Groh J. H., Kupfer T., Crowther P. A., Zapartas E., Renzo M., 2018, *A&A*, 615, A78
 Gräfener G., Owocki S. P., Vink J. S., 2012, *A&A*, 538, A40
 Grevesse N., Sauval A. J., 1998, *Space Science Reviews*, 85, 161
 Groh J. H., 2014, *A&A*, 572, L11
 Groh J. H., Oliveira A. S., Steiner J. E., 2008, *A&A*, 485, 245
 Groh J. H., Georgy C., Ekström S., 2013, *A&A*, 558, L1
 Groh J. H., Meynet G., Ekström S., Georgy C., 2014, *A&A*, 564, A30
 Groh J. H., et al., 2019, *A&A*, 627, A24
 Hagen Bauer W., Bennett P. D., 2014, *ApJ Supplement Series*, 211, 27
 Hansen V., M J., 1944, *ApJ*, 100, 8
 Harper G. M., Griffin R. E. M., Bennett P. D., O'Riain N., 2016, *MNRAS*, 456, 1346
 Heger A., Langer N., Woosley S. E., 2000, *ApJ*, 528, 368
 Heger A., Woosley S. E., Spruit H. C., 2005, *ApJ*, 626, 350
 Hellings P., 1983, *Ap&SS*, 96, 37
 Hellings P., 1984, *Ap&SS*, 104, 83

- Heney L. G., Lelevier R., Levee R. D., 1959, *ApJ*, 129, 2
- Heney L., Vardya M. S., Bodenheimer P., 1965, *ApJ*, 142, 841
- Herwig F., 2000, *A&A*, p. 17
- Higgins E. R., Vink J. S., 2019, *A&A*, 622, A50
- Hillier D. J., Dessart L., 2019, *A&A*, 631, A8
- Huang W., Gies D. R., McSwain M. V., 2010, *ApJ*, 722, 605
- Hunter I., et al., 2008, *ApJ*, 676, L29
- Hurley J. R., Pols O. R., Tout C. A., 2000, *MNRAS*, 315, 543
- Hurley J. R., Tout C. A., Pols O. R., 2002, *MNRAS*, 329, 897
- Iglesias C. A., Rogers F. J., 1993, *ApJ*, 412, 752
- Iglesias C. A., Rogers F. J., 1996, *ApJ*, 464, 943
- Ivanova N., 2018, *ApJ*, 858, L24
- Izzard R. G., Dray L. M., Karakas A. I., Lugaro M., Tout C. A., 2006, *A&A*, 460, 565
- Justham S., Podsiadlowski P., Vink J. S., 2014, *ApJ*, 796, 121
- Keszthelyi Z., Meynet G., Georgy C., Wade G. A., Petit V., David-Uraz A., 2019, *MNRAS*, 485, 5843
- Kobulnicky H. A., Fryer C. L., 2007, *ApJ*, 670, 747
- Kobulnicky H. A., et al., 2014, *ApJSupplement Series*, 213, 34
- Kotak R., Vink J. S., 2006, *A&A*, 460, L5
- Langer N., 1989, *A&A*, 210, 93
- Langer N., El Eid M. F., Baraffe I., 1989, *A&A*, 224, L17
- Lauterborn D., Refsdal S., Weigert A., 1971a, *A&A*, 10, 97
- Lauterborn D., Refsdal S., Roth M. L., 1971b, *A&A*, 13, 119
- Maeder A., 1980, *A&A*, 92, 101
- Maeder A., 2009, *Physics, Formation and Evolution of Rotating Stars*. Springer Berlin Heidelberg, doi:10.1007/978-3-540-76949-1
- Maeder A., Mermilliod J. C., 1981, *A&A*, 93, 136
- Maeder A., Meynet G., 1987, *A&A*, 182, 243
- Maeder A., Meynet G., 1988, *A&ASupplement Series*, 76, 411
- Maeder A., Meynet G., 1989, *A&A*, 210, 155
- Maeder A., Meynet G., 2000, *ARA&A*, 38, 143
- Maeder A., Meynet G., 2012, *Reviews of Modern Physics*, 84, 25
- Martins F., Palacios A., 2013, *A&A*, 560, A16
- Mauron N., Josselin E., 2011, *A&A*, 526, A156
- McLaughlin D. B., 1950, *ApJ*, 111, 449
- Meynet G., Maeder A., 2000, *A&A*, p. 20
- Meynet G., Maeder A., Schaller G., Schaerer D., Charbonnel C., 1994, *A&ASupplement Series*, 103, 97
- Meynet G., Eggenberger P., Maeder A., 2011, *A&A*, 525, L11
- Meynet G., et al., 2015, *A&A*, 575, A60
- Moe M., Di Stefano R., 2017, *ApJSupplement Series*, 230, 15
- Morozova V., Piro A. L., Renzo M., Ott C. D., Clausen D., Couch S. M., Ellis J., Roberts L. F., 2015, *ApJ*, 814, 63
- Morozova V., Piro A. L., Valenti S., 2018, *ApJ*, 858, 15
- Neugent K. F., Levesque E. M., Massey P., 2018, *ApJ*, 156, 225
- Neugent K. F., Levesque E. M., Massey P., Morrell N. I., 2019, *ApJ*, 875, 124
- Nugis T., 2000, *A&A*, p. 18
- Paczynski B., 1971, *Acta Astron.*, 21, 417
- Pastorello A., et al., 2007, *Nature*, 447, 829
- Paxton B., Bildsten L., Dotter A., Herwig F., Lesaffre P., Timmes F., 2011, *ApJSupplement Series*, 192, 3
- Paxton B., et al., 2013, *ApJSupplement Series*, 208, 4
- Paxton B., et al., 2015, *ApJSupplement Series*, 220, 15
- Paxton B., et al., 2018, *ApJSupplement Series*, 234, 34
- Paxton B., et al., 2019, *ApJSupplement Series*, 243, 10
- Peters G. J., Pewett T. D., Gies D. R., Touhami Y. N., Grundstrom E. D., 2013, *ApJ*, 765, 2
- Podsiadlowski P., Joss P. C., Hsu J. J. L., 1992, *ApJ*, 391, 246
- Podsiadlowski P., Hsu J. J. L., Joss P. C., Ross R. R., 1993, *Nature*, 364, 509
- Pols O. R., Tout C. A., Eggleton P. P., Han Z., 1995, *MNRAS*, 274, 964
- Pols O. R., Schröder K.-P., Hurley J. R., Tout C. A., Eggleton P. P., 1998, *MNRAS*, 298, 525
- Ramírez-Agudelo O. H., et al., 2013, *A&A*, 560, A29
- Ramírez-Agudelo O. H., et al., 2015, *A&A*, 580, A92
- Renzo M., Ott C. D., Shore S. N., de Mink S. E., 2017, *A&A*, 603, A118
- Rogers F. J., Nayfonov A., 2002, *ApJ*, 576, 1064
- Sana H., et al., 2012, *Science*, 337, 444
- Sana H., et al., 2013, *A&A*, 550, A107
- Saumon D., Chabrier G., van Horn H. M., 1995, *ApJSupplement Series*, 99, 713
- Schaerer D., 1996, *A&A*, 309, 129
- Schaerer D., de Koter A., Schmutz W., Maeder A., 1996, *A&A*, 310, 837
- Schneider F. R. N., et al., 2014, *ApJ*, 780, 117
- Schootemeijer A., Langer N., 2018, *A&A*, 611, A75
- Schootemeijer A., Langer N., Grin N. J., Wang C., 2019, *A&A*, 625, A132
- Schwarzschild M., 1961, *ApJ*, 134, 1
- Schwarzschild M., Härm R., 1958, *ApJ*, 128, 348
- Smith N., 2014, *ARA&A*, 52, 487
- Smith N., et al., 2007, *ApJ*, 666, 1116
- Sota A., Apellániz J. M., Morrell N. I., Barbá R. H., Walborn N. R., Gamen R. C., Arias J. I., Alfaro E. J., 2014, *ApJSupplement Series*, 211, 10
- Stancliffe R. J., Eldridge J. J., 2009, *MNRAS*, 396, 1699
- Steiner J. E., Oliveira A. S., 2005, *A&A*, 444, 895
- Stencel R. E., Hopkins J. L., Hagen W., Fried R., Schmidtke P. C., Kondo Y., Chapman R. D., 1984, *ApJ*, 281, 751
- Stothers R., 1970, *MNRAS*, 151, 65
- Stothers R., 1974, *ApJ*, 194, 699
- Stothers R. B., Chin C.-W., 1985, *ApJ*, 292, 222
- Stothers R. B., Chin C.-W., 1995, *ApJ*, 440, 297
- Sukhbold T., Ertl T., Woosley S. E., Brown J. M., Janka H.-T., 2016, *ApJ*, 821, 38
- Szécsi D., Langer N., Yoon S.-C., Sanyal D., de Mink S., Evans C. J., Dermine T., 2015, *A&A*, 581, A15
- Timmes F. X., Swesty F. D., 2000, *ApJSupplement Series*, 126, 501
- Tout C. A., Pols O. R., Eggleton P. P., Han Z., 1996, *MNRAS*, 281, 257
- Tout C. A., Aarseth S. J., Pols O. R., Eggleton P. P., 1997, *MNRAS*, 291, 732
- Ugliano M., Janka H.-T., Marek A., Arcones A., 2012, *ApJ*, 757, 69
- Vanbeveren D., Van Bever J., Belkus H., 2007, *ApJ*, 662, L107
- Vink J. S., de Koter A., Lamers H. J. G. L. M., 2001, *A&A*, 369, 574
- Wang L., Gies D. R., Peters G. J., 2017, *ApJ*, 843, 60
- Woosley S. E., Weaver T. A., 1994, *ApJ*, 423, 371
- Wright K. O., 1970, *Vistas in Astronomy*, 12, 147
- Yaron O., et al., 2017, *NaturePhysics*, 13, 510
- Yoon S.-C., 2015, *Publ. Astron. Soc. Australia*, 32, e015
- Yoon S.-C., Dierks A., Langer N., 2012, *A&A*, 542, A113
- Zapartas E., et al., 2019, *A&A*, 631, A5
- de Jager C., Nieuwenhuijzen H., van der Hucht K. A., 1988, *A&ASupplement Series*, 72, 259
- de Mink S. E., Belczynski K., 2015, *ApJ*, 814, 58
- de Mink S. E., Langer N., Izzard R. G., Sana H., de Koter A., 2013, *ApJ*, 764, 166
- de Mink S. E., Sana H., Langer N., Izzard R. G., Schneider F. R. N., 2014, *ApJ*, 782, 7
- deBoer R. J., et al., 2017, *Reviews of Modern Physics*, 89, 035007
- van Bever J., Vanbeveren D., 1998, *A&A*, 334, 21

APPENDIX A: CORE AND ENVELOPE MASSES FOR CORE-H BURNING MODELS**APPENDIX B: CORE AND ENVELOPE MASSES FOR CORE-HE BURNING MODELS****APPENDIX C: CENTRAL TEMPERATURE VS. CORE MASS RATIO****APPENDIX D: SURFACE PROPERTIES FOR CORE-HE BURNING MODELS****APPENDIX E: INTERIOR GRAPHS****APPENDIX F: KIPPENHAHN-LIKE FIGURES**

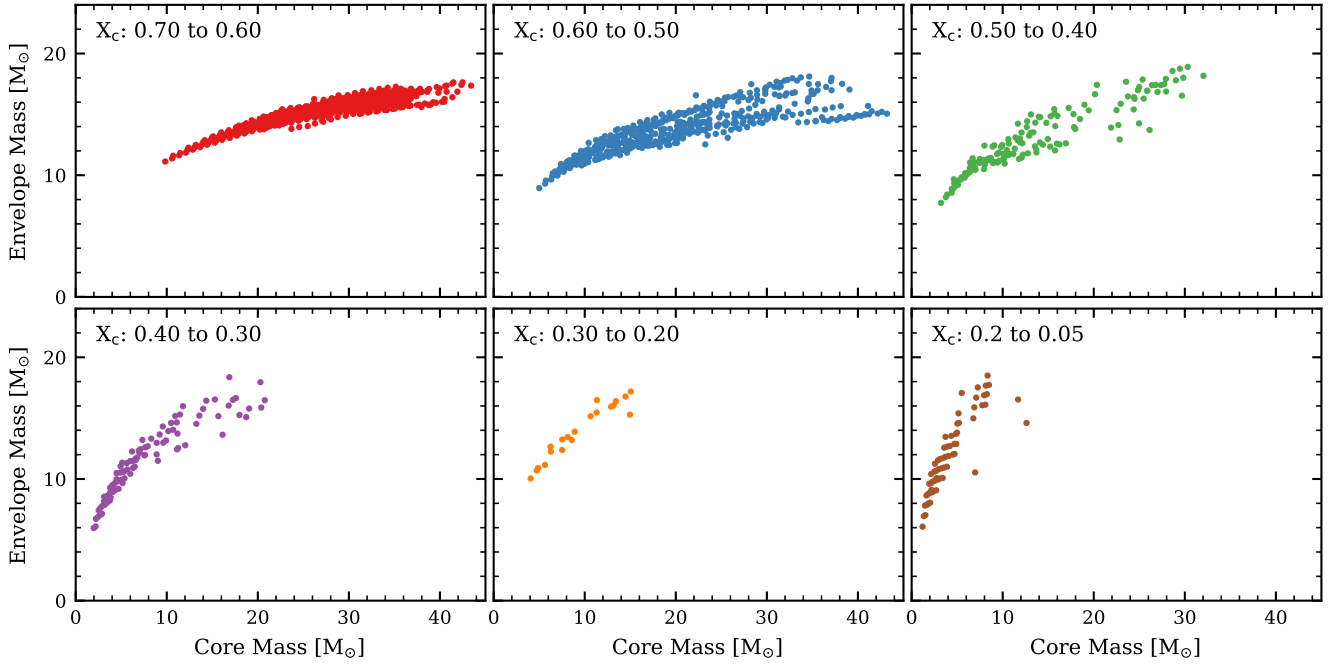


Figure A1. Summary of the 3 key structural parameters (convective core mass, envelope mass and core composition) for each of our core-H burning structure models. Each dot represents an individual core-H burning stellar structure model with the given core mass and envelope mass in M_{\odot} . The models are divided up into bins by their central H mass fraction (X_c) as indicated in each plot.

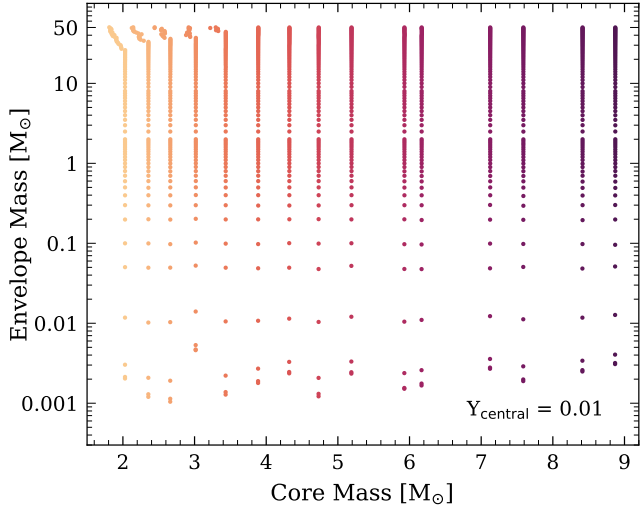


Figure B1. Each dot represents a core-He burning structure, similar to Fig. 3, but with $Y_c = 0.01$

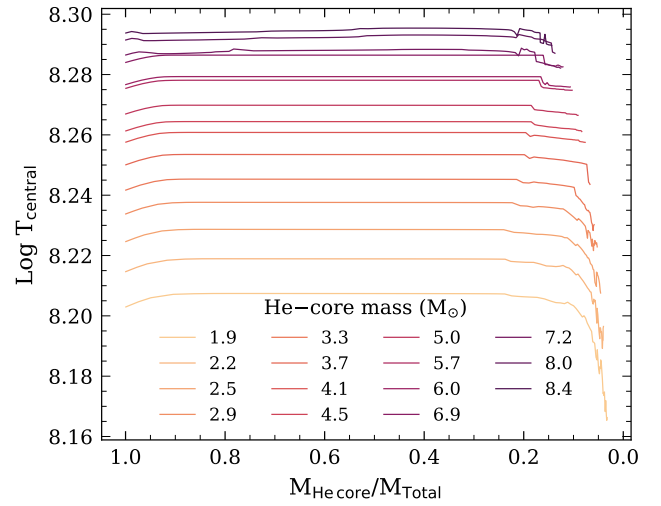


Figure C1. The central temperature as a function of envelope mass for core-He burning models of constant core mass. For most combinations of core and envelope masses, the central temperature of the core is not affected by the mass of the envelope.

Table D1. Summary of surface properties for core-He burning models with a He-core mass of $4.1M_{\odot}$, a central Helium abundance of 0.50 and envelope masses from $10^{-3} - 25M_{\odot}$. $F_{\text{H-shell}}$ refers to the fraction of the total nuclear energy generated in the H-Shell. The same table for envelope masses from $25 - 50M_{\odot}$ can be found below in Table D2.

$M_{\text{core}} [M_{\odot}]$	$M_{\text{env}} [M_{\odot}]$	$\log T_{\text{eff}} [\text{K}]$	$T_{\text{eff}} [\text{K}]$	$\log L/L_{\odot}$	$\log g$	$\log R/R_{\odot}$	$F_{\text{H-shell}}$
4.1	2×10^{-3}	4.96	91700	4.37	5.48	-0.21	0.00
4.1	4×10^{-3}	4.96	91700	4.37	5.48	-0.21	0.00
4.1	0.01	4.96	91750	4.38	5.48	-0.21	0.00
4.1	0.05	4.96	91680	4.39	5.48	-0.21	0.00
4.1	0.1	4.95	88160	4.40	5.40	-0.17	0.00
4.1	0.2	4.88	75700	4.43	5.11	-0.02	0.00
4.1	0.3	4.84	68800	4.46	4.93	0.08	0.03
4.1	0.4	4.62	41630	4.50	4.03	0.53	0.10
4.1	0.5	4.45	28000	4.53	3.32	0.89	0.17
4.1	0.6	4.26	18010	4.55	2.54	1.29	0.22
4.1	0.7	3.96	9200	4.56	1.37	1.88	0.24
4.1	0.8	3.62	4150	4.57	-0.01	2.57	0.26
4.1	0.9	3.57	3690	4.57	-0.21	2.67	0.26
4.1	1.0	3.55	3580	4.57	-0.26	2.70	0.26
4.1	1.1	3.55	3520	4.57	-0.28	2.72	0.27
4.1	1.2	3.54	3480	4.57	-0.29	2.73	0.27
4.1	1.3	3.54	3460	4.58	-0.29	2.73	0.27
4.1	1.4	3.54	3440	4.58	-0.30	2.74	0.27
4.1	1.5	3.53	3420	4.58	-0.30	2.74	0.28
4.1	1.6	3.53	3410	4.58	-0.30	2.75	0.28
4.1	1.7	3.53	3400	4.58	-0.29	2.75	0.28
4.1	1.8	3.53	3400	4.58	-0.29	2.75	0.28
4.1	1.9	3.53	3390	4.58	-0.29	2.75	0.28
4.1	2.0	3.53	3390	4.58	-0.28	2.76	0.28
4.1	2.5	3.53	3380	4.58	-0.26	2.76	0.29
4.1	3.0	3.53	3380	4.59	-0.23	2.76	0.29
4.1	3.5	3.53	3390	4.59	-0.19	2.76	0.29
4.1	4.0	3.53	3400	4.59	-0.16	2.76	0.30
4.1	4.5	3.53	3410	4.59	-0.13	2.75	0.30
4.1	5.0	3.53	3430	4.59	-0.10	2.75	0.30
4.1	5.5	3.54	3440	4.59	-0.07	2.75	0.30
4.1	6.0	3.54	3460	4.59	-0.04	2.74	0.30
4.1	6.5	3.54	3470	4.59	-0.01	2.74	0.31
4.1	7.0	3.54	3490	4.59	0.02	2.73	0.31
4.1	7.5	3.54	3510	4.60	0.04	2.73	0.31
4.1	8.0	3.55	3520	4.60	0.07	2.73	0.31
4.1	9.0	3.55	3550	4.60	0.12	2.72	0.31
4.1	10.0	3.55	3590	4.60	0.16	2.71	0.32
4.1	11.0	3.56	3620	4.60	0.21	2.71	0.32
4.1	12.0	3.56	3650	4.60	0.25	2.70	0.32
4.1	13.0	3.57	3680	4.60	0.29	2.69	0.32
4.1	14.0	3.57	3700	4.60	0.32	2.69	0.33
4.1	15.0	3.57	3730	4.61	0.36	2.68	0.33
4.1	16.0	3.58	3760	4.61	0.39	2.68	0.33
4.1	17.0	3.58	3800	4.61	0.42	2.67	0.34
4.1	18.0	4.29	19620	5.04	2.87	1.46	0.75
4.1	19.0	4.32	20770	5.09	2.94	1.43	0.77
4.1	20.0	4.33	21490	5.12	2.98	1.42	0.79
4.1	21.0	4.34	22080	5.15	3.02	1.41	0.80
4.1	22.0	4.36	22710	5.18	3.05	1.40	0.82
4.1	23.0	4.37	23270	5.21	3.08	1.39	0.84
4.1	24.0	4.38	23740	5.24	3.11	1.39	0.84
4.1	25.0	4.38	24260	5.26	3.13	1.39	0.85

Table D2. Same as Table D1 but for envelope masses from 25 – 50 M_{\odot} .

$M_{\text{core}} [M_{\odot}]$	$M_{\text{env}} [M_{\odot}]$	$\log T_{\text{eff}} [\text{K}]$	$T_{\text{eff}} [\text{K}]$	$\log L/L_{\odot}$	$\log g$	$\log R/R_{\odot}$	$F_{\text{H-shell}}$
4.1	26.0	4.39	24760	5.29	3.15	1.38	0.86
4.1	27.0	4.40	25230	5.32	3.18	1.38	0.87
4.1	28.0	4.41	25690	5.34	3.20	1.37	0.88
4.1	29.0	4.42	26120	5.36	3.22	1.37	0.89
4.1	30.0	4.42	26530	5.39	3.23	1.37	0.89
4.1	31.0	4.43	26940	5.41	3.25	1.37	0.90
4.1	32.0	4.44	27320	5.43	3.27	1.37	0.90
4.1	33.0	4.44	27690	5.45	3.28	1.36	0.91
4.1	34.0	4.45	28050	5.47	3.29	1.36	0.91
4.1	35.0	4.45	28400	5.49	3.31	1.36	0.92
4.1	36.0	4.46	28730	5.51	3.32	1.36	0.92
4.1	37.0	4.46	29060	5.53	3.33	1.36	0.92
4.1	38.0	4.47	29380	5.55	3.34	1.36	0.93
4.1	39.0	4.47	29680	5.57	3.35	1.36	0.93
4.1	40.0	4.48	29970	5.58	3.36	1.36	0.93
4.1	41.0	4.48	30250	5.60	3.37	1.36	0.93
4.1	42.0	4.48	30520	5.62	3.38	1.36	0.94
4.1	43.0	4.49	30940	5.63	3.40	1.36	0.94
4.1	44.0	4.49	31200	5.65	3.40	1.36	0.94
4.1	45.0	4.50	31450	5.66	3.41	1.36	0.95
4.1	46.0	4.50	31690	5.68	3.42	1.36	0.95
4.1	47.0	4.50	31930	5.69	3.42	1.36	0.95
4.1	48.0	4.51	32150	5.71	3.43	1.36	0.95
4.1	49.0	4.51	32370	5.72	3.44	1.36	0.95
4.1	50.0	4.51	32590	5.73	3.44	1.36	0.95

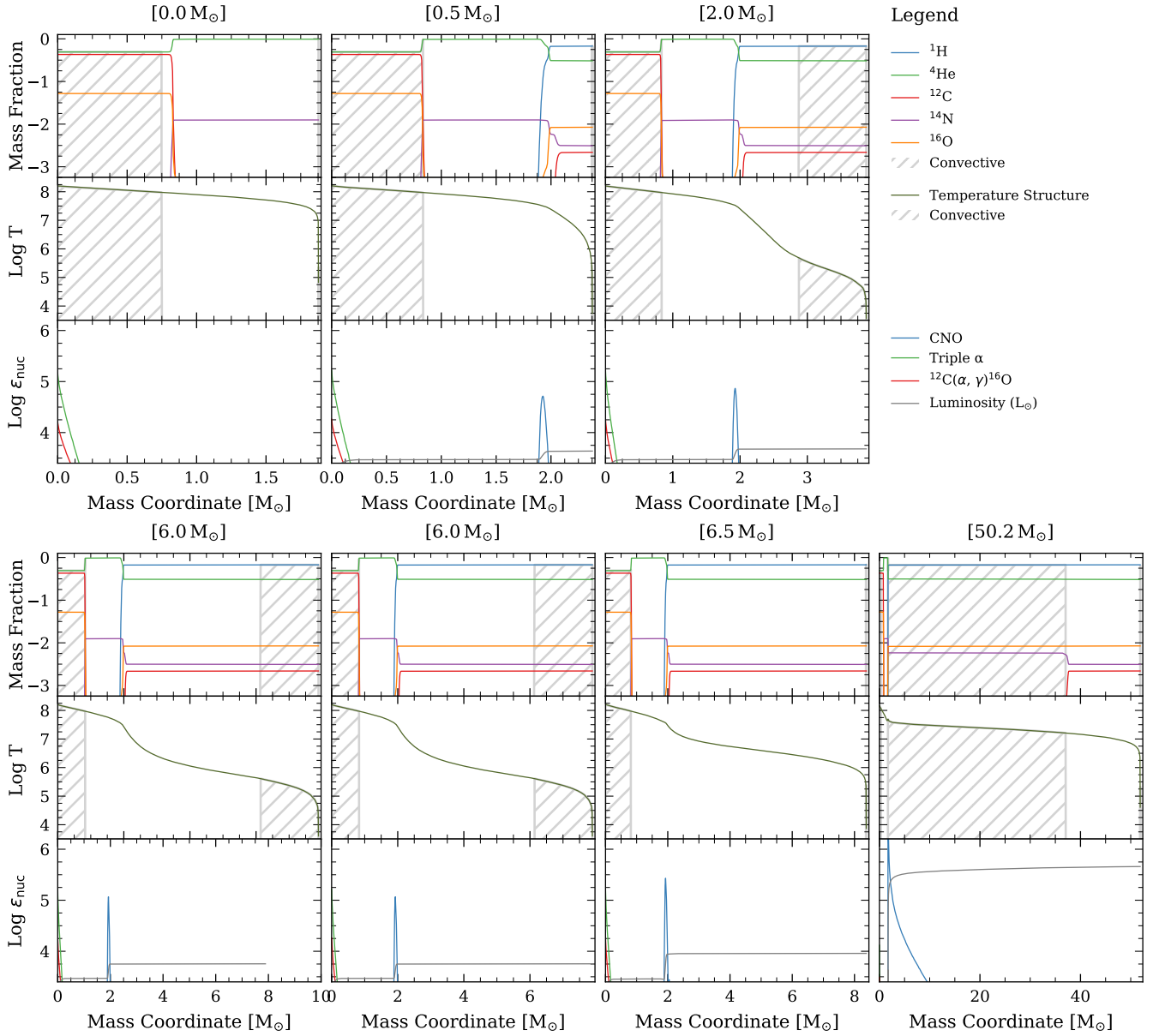


Figure E1. Internal structure profiles of core-He burning models with $M_{\text{core}} = 1.9 M_{\odot}$, $Y_{\text{c}} = 0.50$, and a range of envelope masses (indicated at top of each panel) selected to represent the qualitative behaviour of the models. See caption of Fig. 8 for further details.

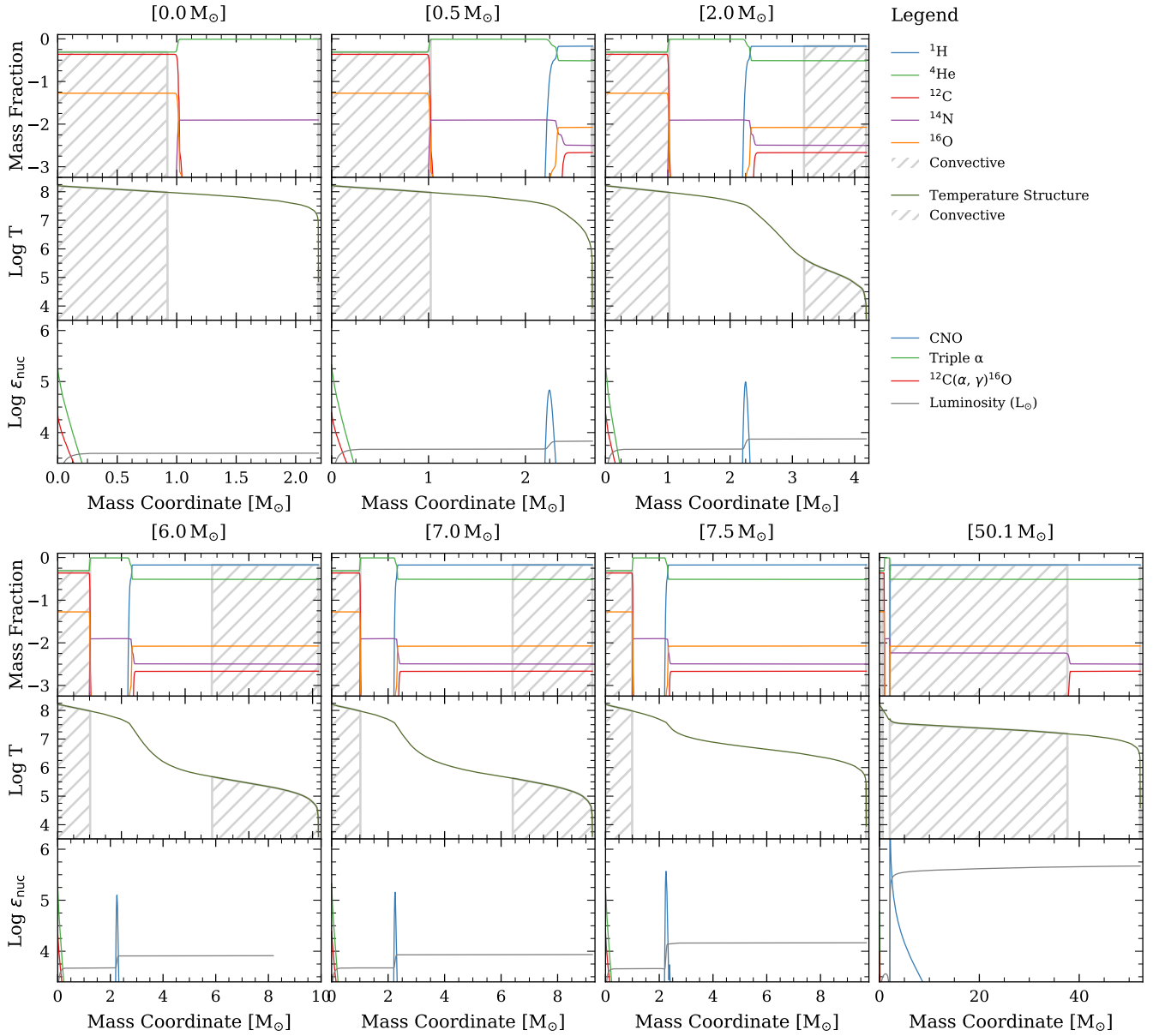


Figure E2. Internal structure profiles of core-He burning models with $M_{\text{core}} = 2.2 M_{\odot}$, $Y_c = 0.50$, and a range of envelope masses (indicated at top of each panel) selected to represent the qualitative behaviour of the models. See caption of Fig. 8 for further details.

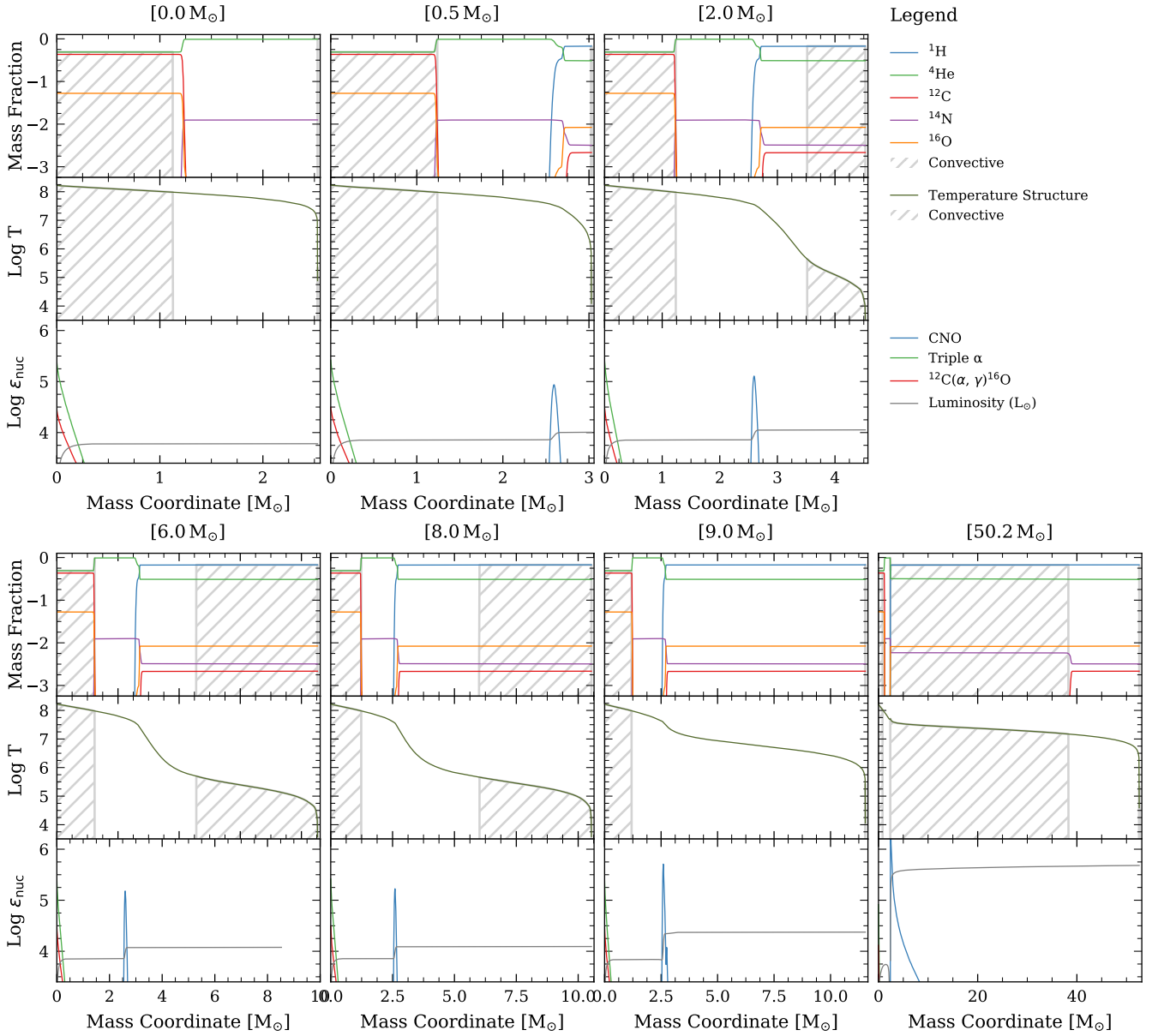


Figure E3. Internal structure profiles of core-He burning models with $M_{\text{core}} = 2.5 M_{\odot}$, $Y_{\text{c}} = 0.50$, and a range of envelope masses (indicated at top of each panel) selected to represent the qualitative behaviour of the models. See caption of Fig. 8 for further details.

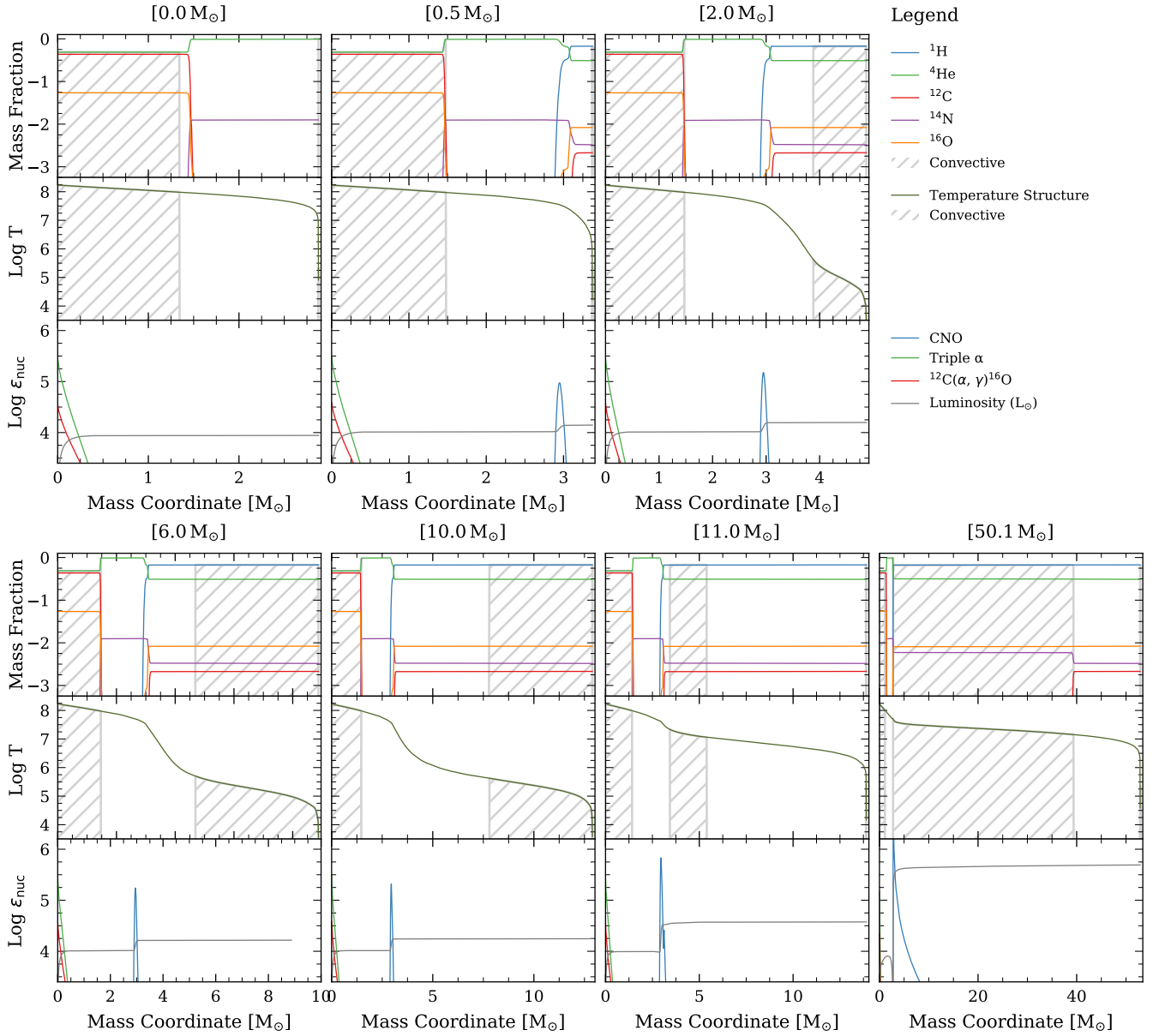


Figure E4. Internal structure profiles of core–He burning models with $M_{\text{core}} = 2.9M_{\odot}$, $Y_{\text{c}} = 0.50$, and a range of envelope masses (indicated at top of each panel) selected to represent the qualitative behaviour of the models. See caption of Fig. 8 for further details.

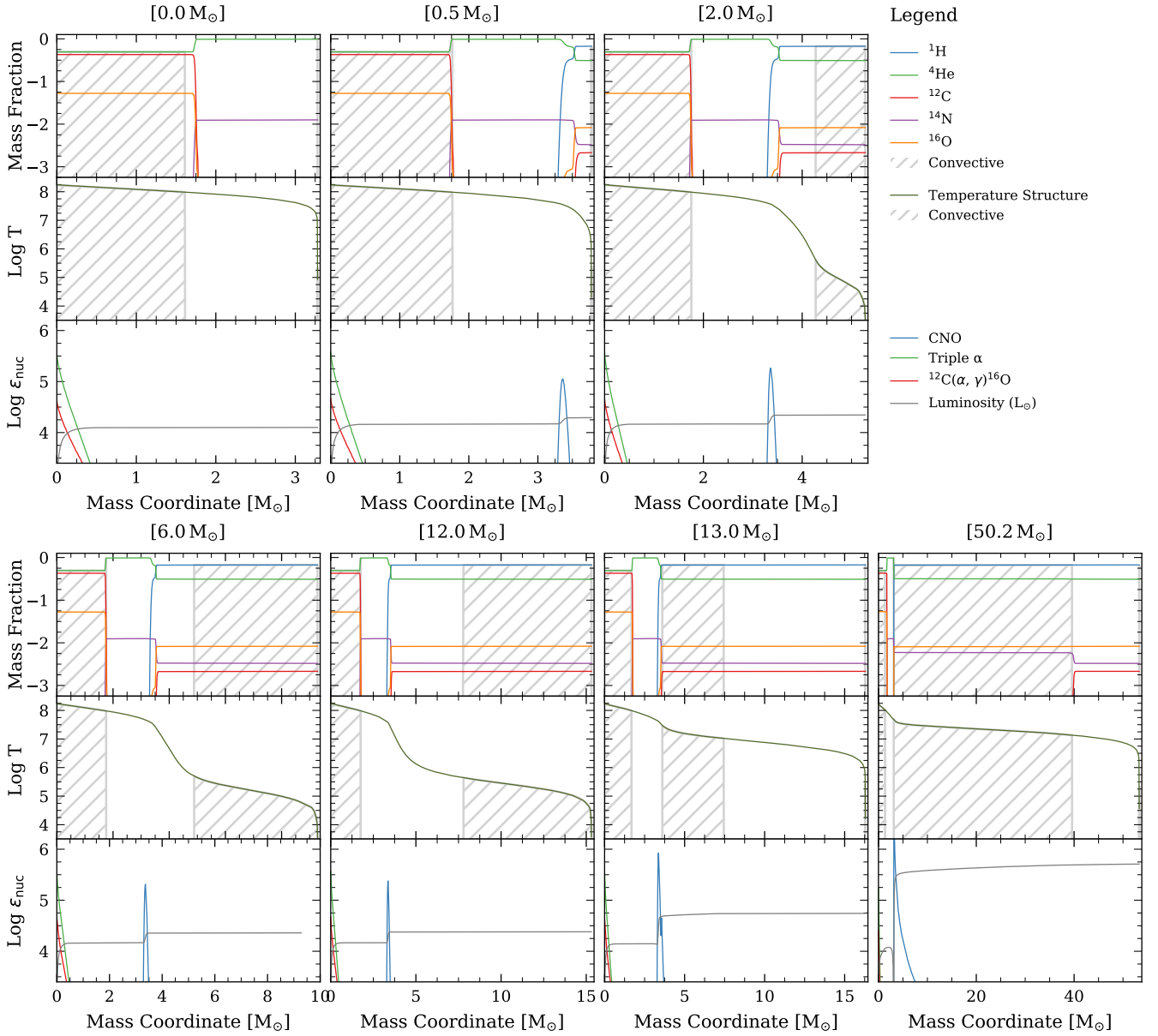


Figure E5. Internal structure profiles of core-He burning models with $M_{\text{core}} = 3.3 M_{\odot}$, $Y_c = 0.50$, and a range of envelope masses (indicated at top of each panel) selected to represent the qualitative behaviour of the models. See caption of Fig. 8 for further details.

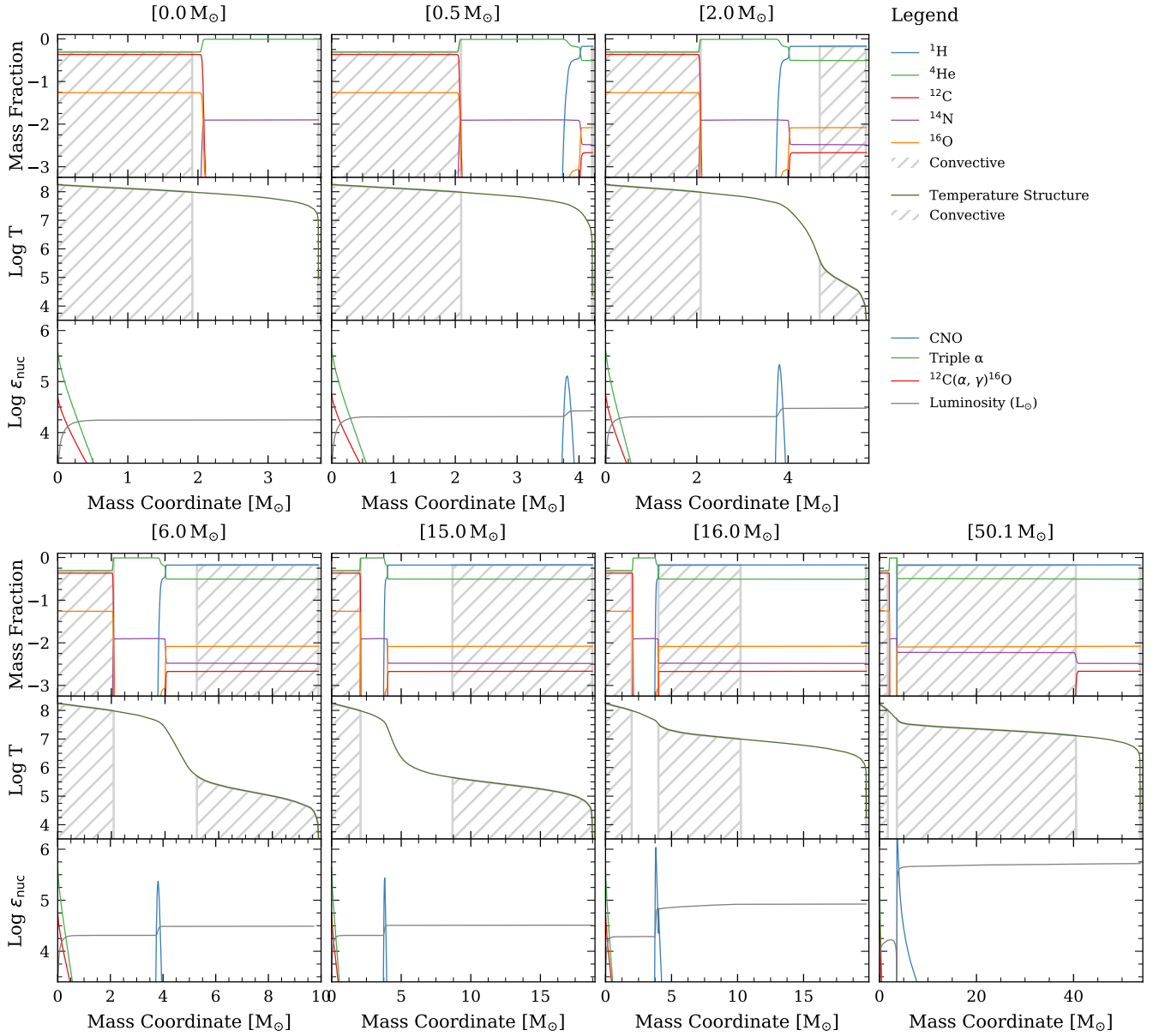


Figure E6. Internal structure profiles of core–He burning models with $M_{\text{core}} = 3.7M_{\odot}$, $Y_{\text{c}} = 0.50$, and a range of envelope masses (indicated at top of each panel) selected to represent the qualitative behaviour of the models. See caption of Fig. 8 for further details.

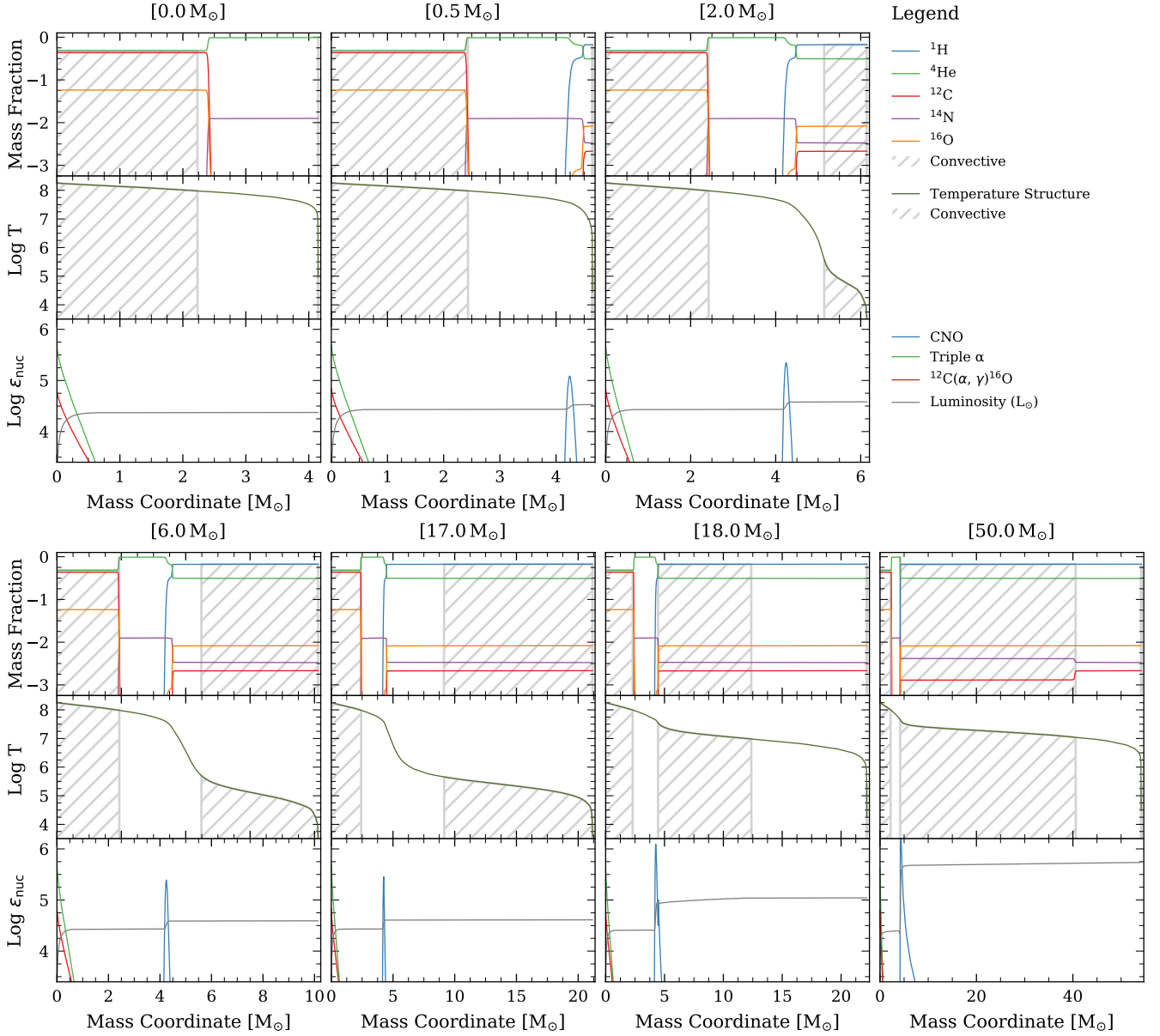


Figure E7. Internal structure profiles of core-He burning models with $M_{\text{core}} = 4.1 M_{\odot}$, $Y_{\text{c}} = 0.50$, and a range of envelope masses (indicated at top of each panel) selected to represent the qualitative behaviour of the models. See caption of Fig. 8 for further details.

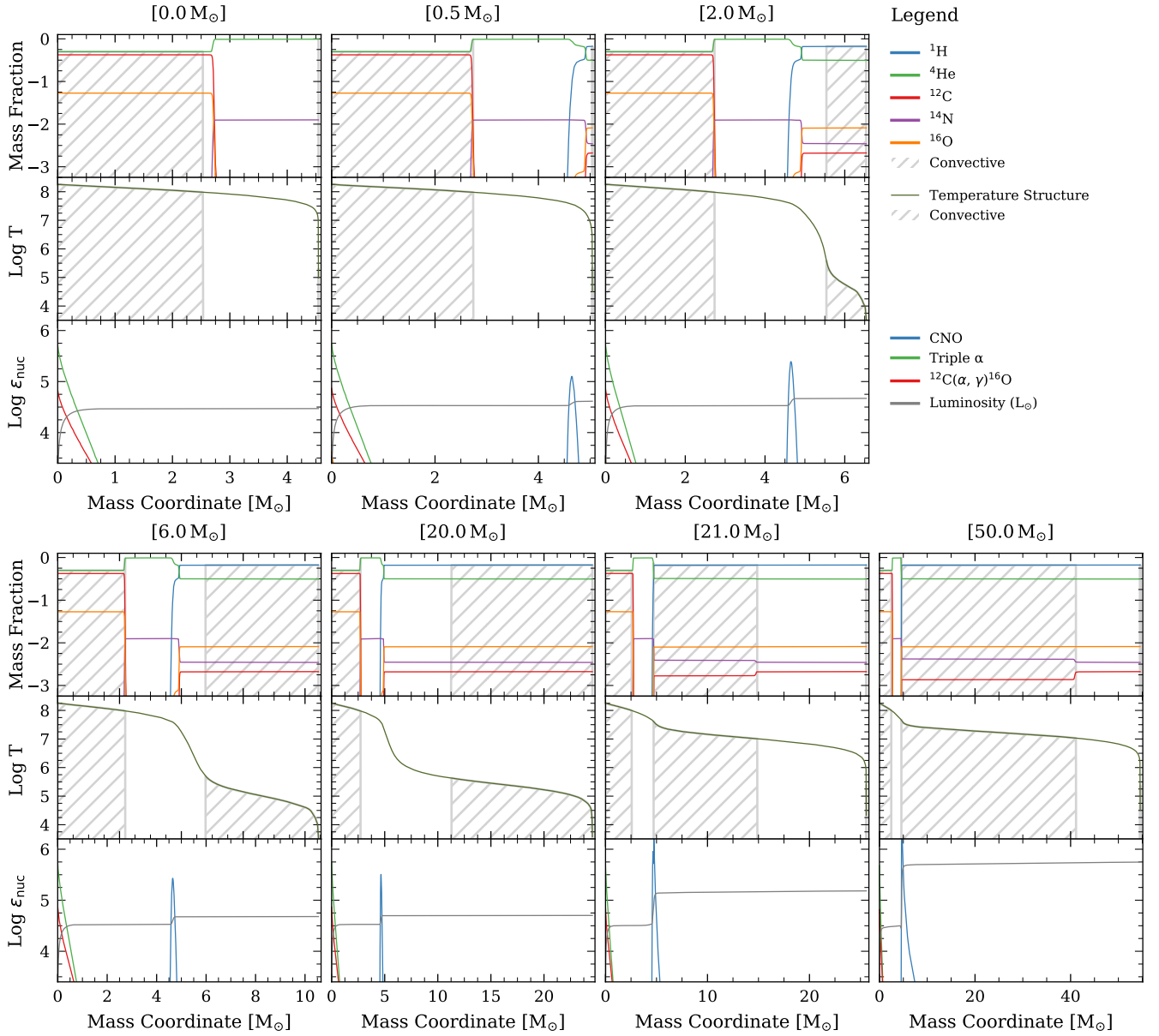


Figure E8. Internal structure profiles of core-He burning models with $M_{\text{core}} = 4.5 M_{\odot}$, $Y_{\text{c}} = 0.50$, and a range of envelope masses (indicated at top of each panel) selected to represent the qualitative behaviour of the models. See caption of Fig. 8 for further details.

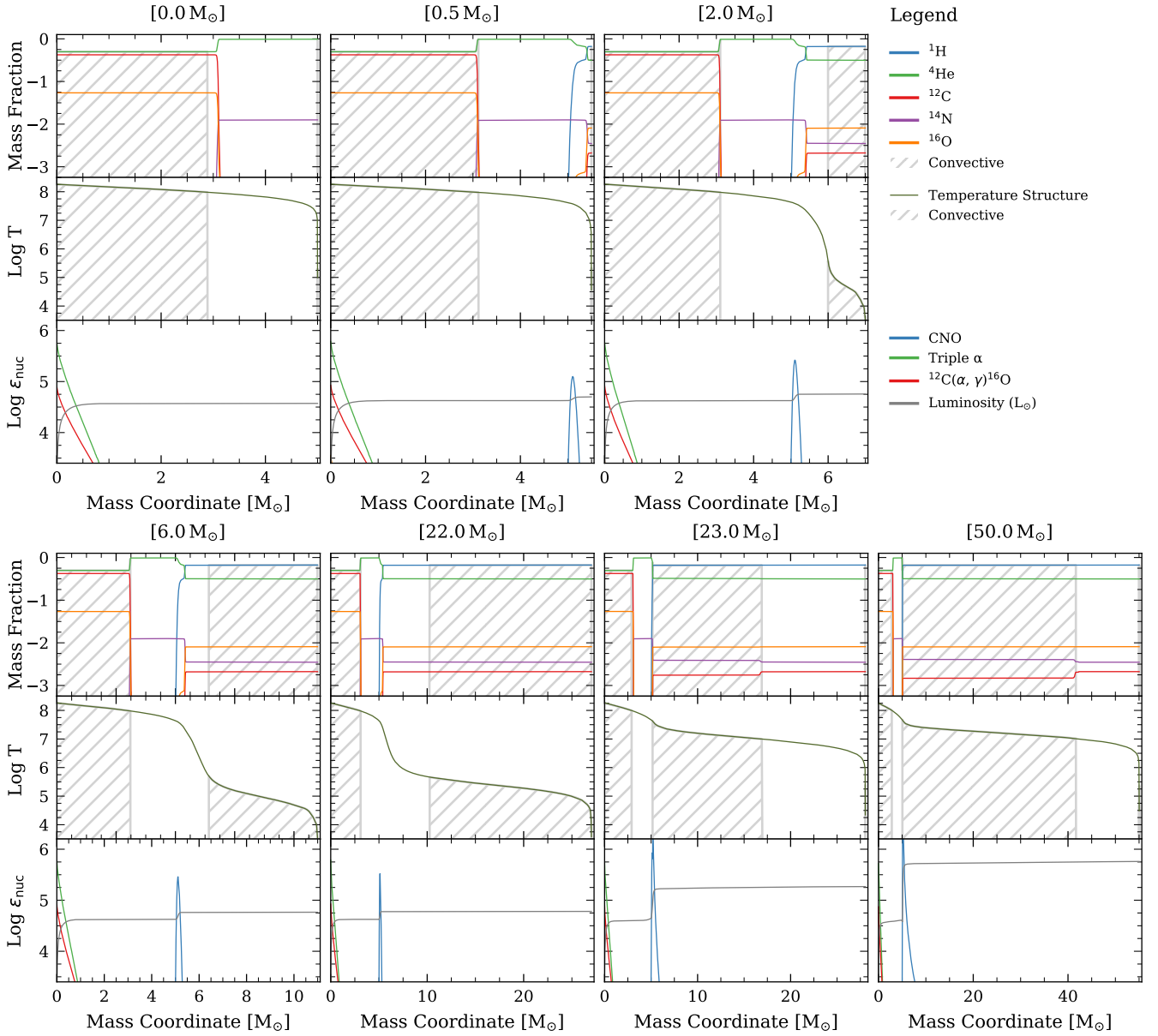


Figure E9. Internal structure profiles of core-He burning models with $M_{\text{core}} = 5.0 M_{\odot}$, $Y_{\text{c}} = 0.50$, and a range of envelope masses (indicated at top of each panel) selected to represent the qualitative behaviour of the models. See caption of Fig. 8 for further details.

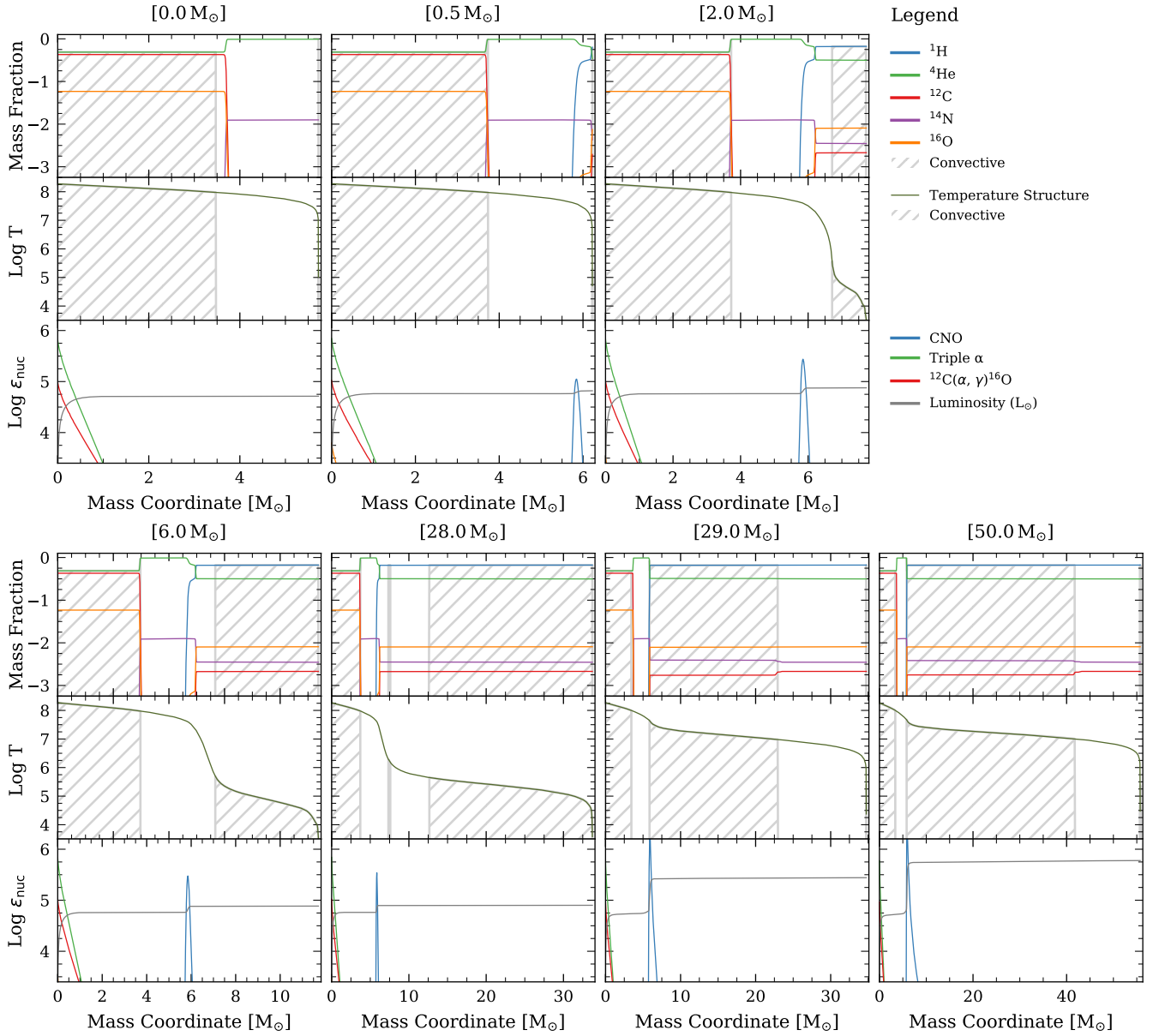


Figure E10. Internal structure profiles of core-He burning models with $M_{\text{core}} = 5.7 M_{\odot}$, $Y_c = 0.50$, and a range of envelope masses (indicated at top of each panel) selected to represent the qualitative behaviour of the models. See caption of Fig. 8 for further details.

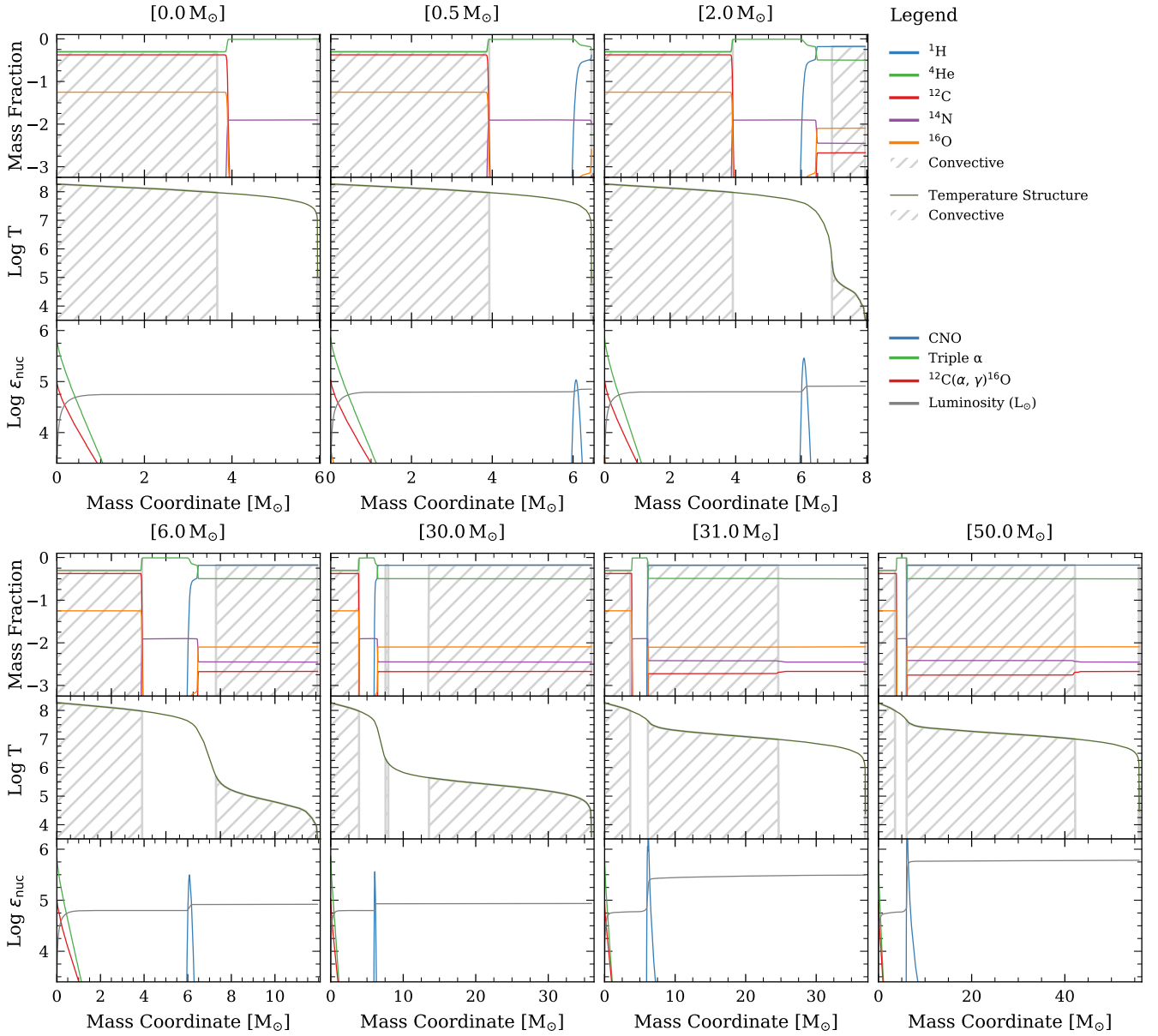


Figure E11. Internal structure profiles of core-He burning models with $M_{\text{core}} = 6.0 M_{\odot}$, $Y_{\text{c}} = 0.50$, and a range of envelope masses (indicated at top of each panel) selected to represent the qualitative behaviour of the models. See caption of Fig. 8 for further details.

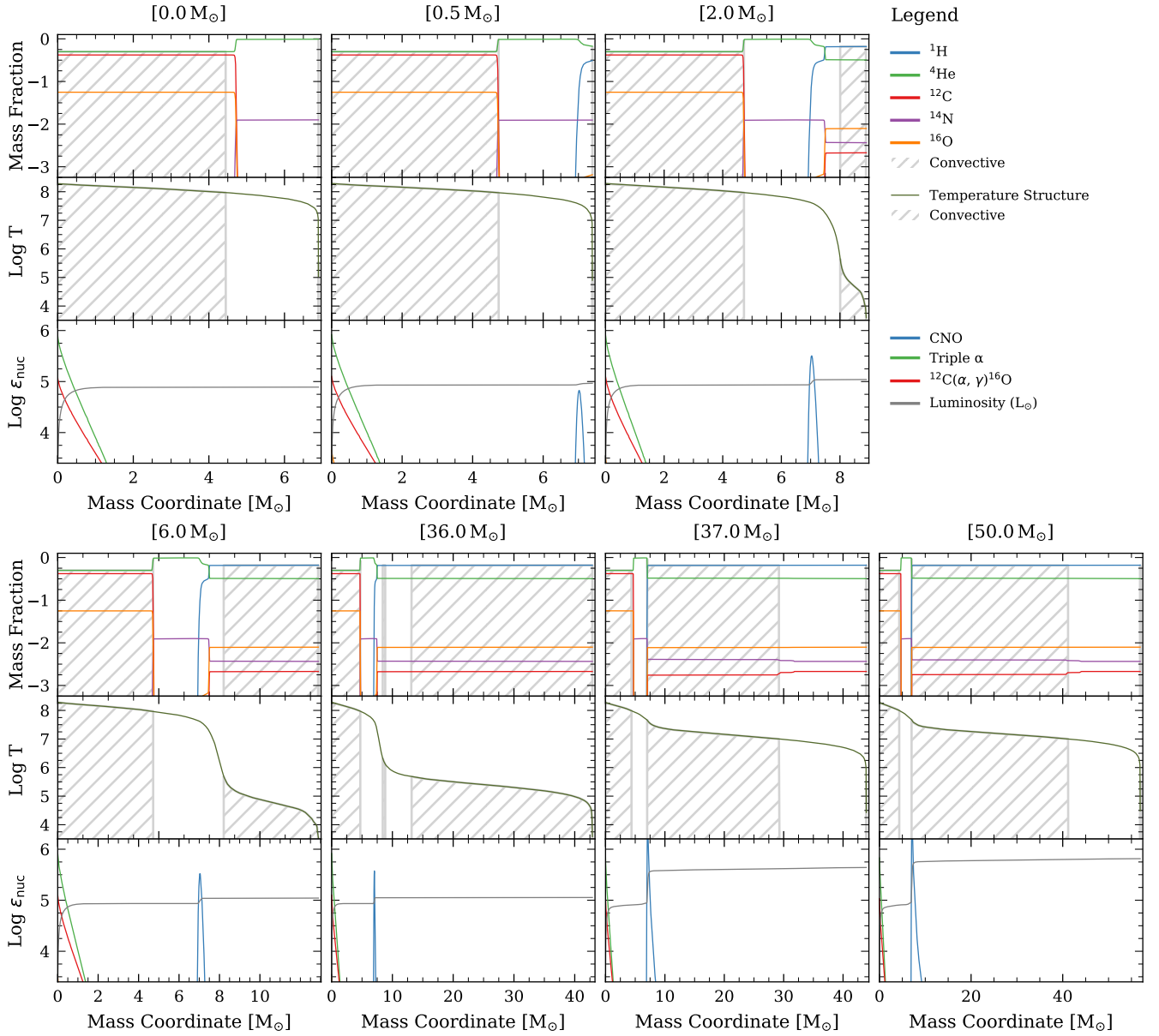


Figure E12. Internal structure profiles of core-He burning models with $M_{\text{core}} = 6.9 M_{\odot}$, $Y_{\text{c}} = 0.50$, and a range of envelope masses (indicated at top of each panel) selected to represent the qualitative behaviour of the models. See caption of Fig. 8 for further details.

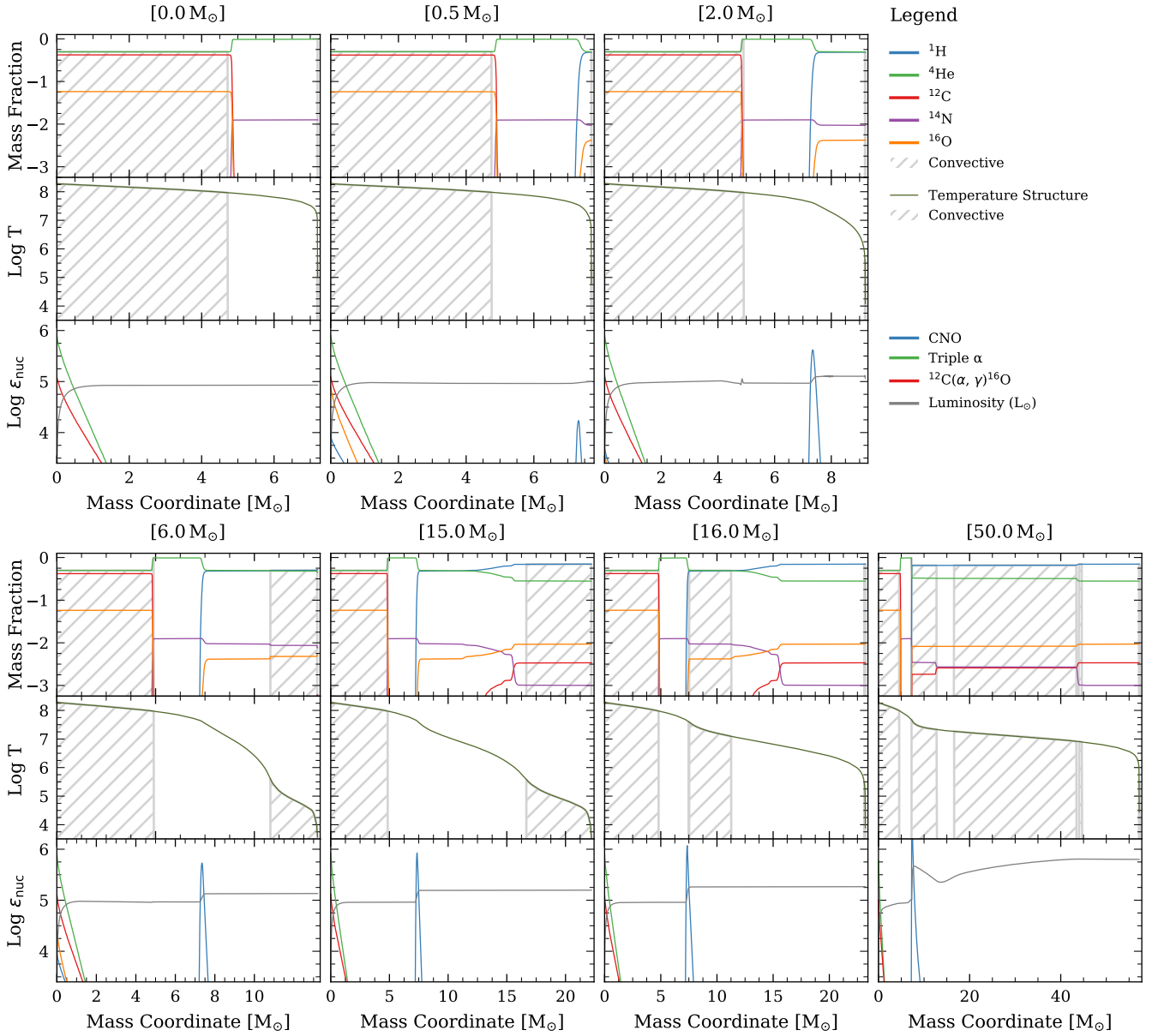


Figure E13. Internal structure profiles of core-He burning models with $M_{\text{core}} = 7.2 M_{\odot}$, $Y_c = 0.50$, and a range of envelope masses (indicated at top of each panel) selected to represent the qualitative behaviour of the models. See caption of Fig. 8 for further details.

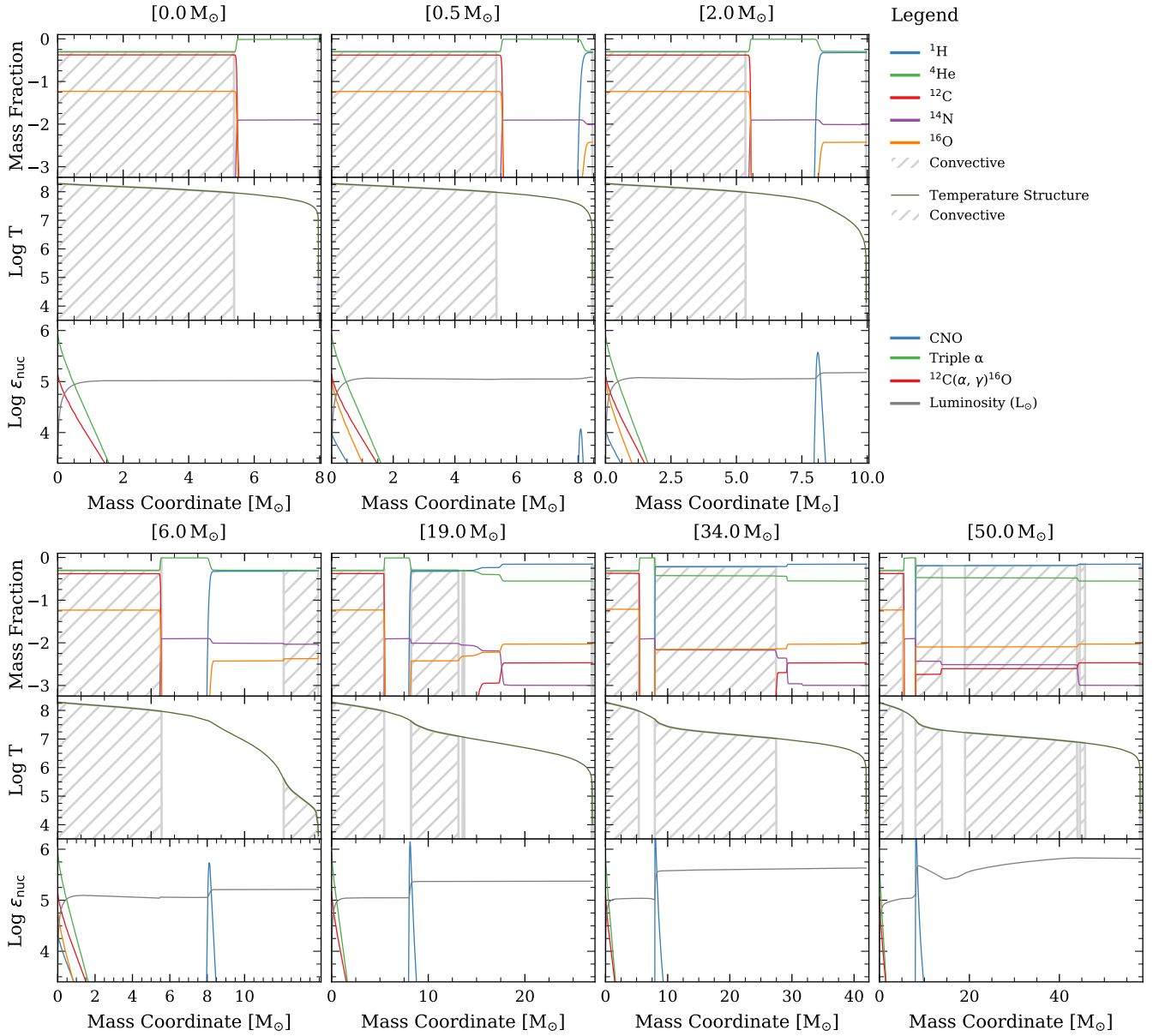


Figure E14. Internal structure profiles of core-He burning models with $M_{\text{core}} = 8.0 M_{\odot}$, $Y_c = 0.50$, and a range of envelope masses (indicated at top of each panel) selected to represent the qualitative behaviour of the models. See caption of Fig. 8 for further details.

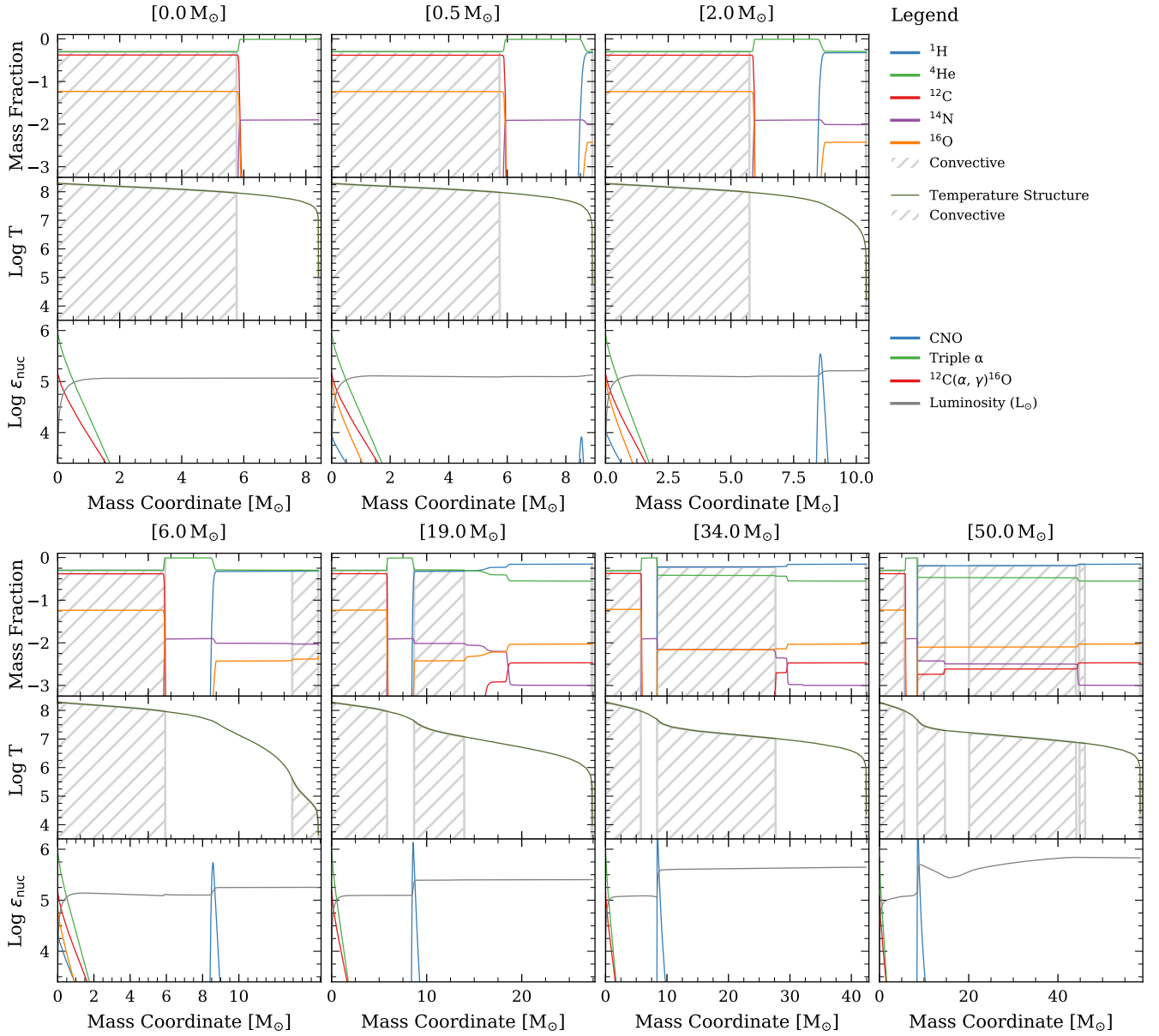


Figure E15. Internal structure profiles of core-He burning models with $M_{\text{core}} = 8.4M_{\odot}$, $Y_{\text{c}} = 0.50$, and a range of envelope masses (indicated at top of each panel) selected to represent the qualitative behaviour of the models. See caption of Fig. 8 for further details.

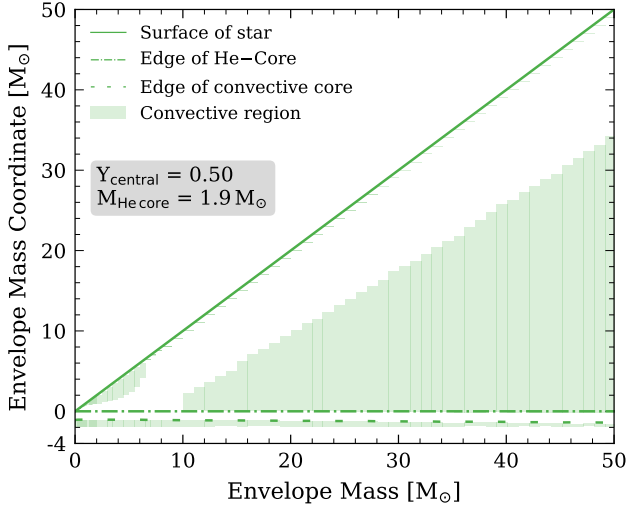


Figure F1. Kippenhahn-like diagram for core–He burning models with a constant $M_{\text{core}} = 1.9M_{\odot}$ and varying envelope mass. See caption of Fig. 7 for further details.

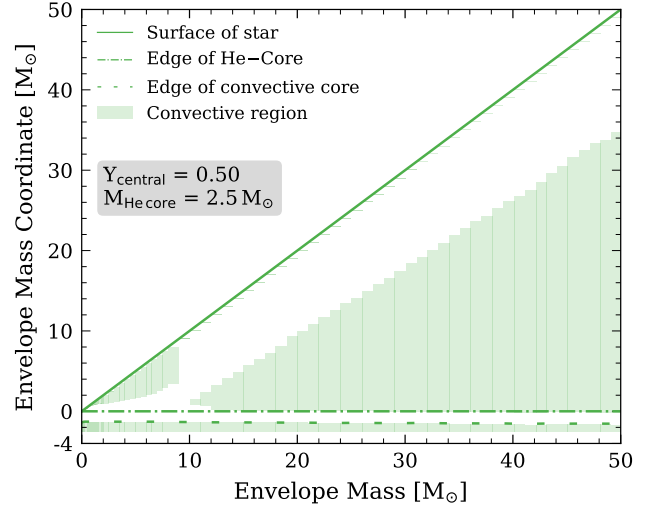


Figure F3. Kippenhahn-like diagram for core–He burning models with a constant $M_{\text{core}} = 2.5M_{\odot}$ and varying envelope mass. See caption of Fig. 7 for further details.

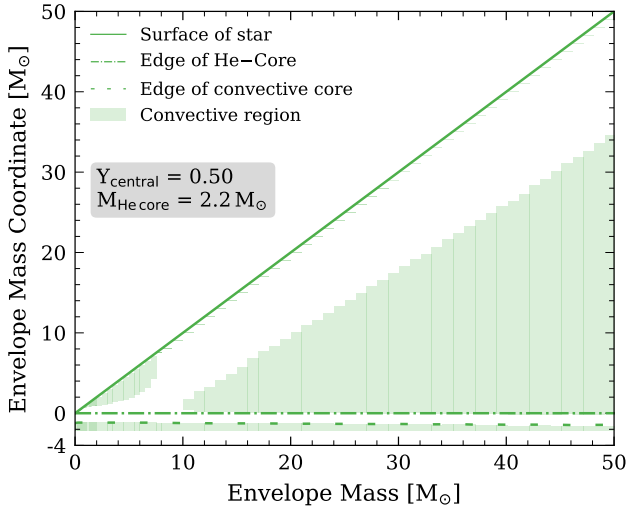


Figure F2. Kippenhahn-like diagram for core–He burning models with a constant $M_{\text{core}} = 2.2M_{\odot}$ and varying envelope mass. See caption of Fig. 7 for further details.

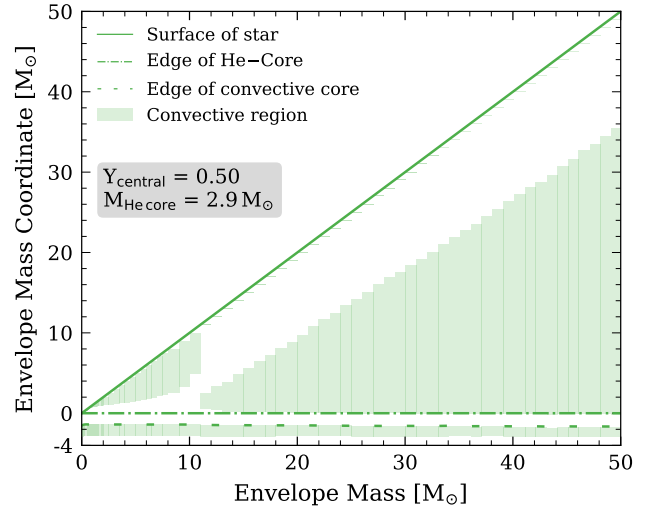


Figure F4. Kippenhahn-like diagram for core–He burning models with a constant $M_{\text{core}} = 2.9M_{\odot}$ and varying envelope mass. See caption of Fig. 7 for further details.

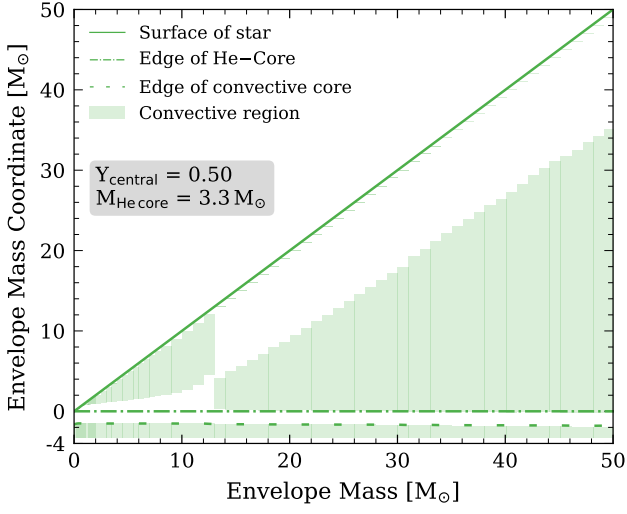


Figure F5. Kippenhahn-like diagram for core–He burning models with a constant $M_{\text{core}} = 3.3M_{\odot}$ and varying envelope mass. See caption of Fig. 7 for further details.

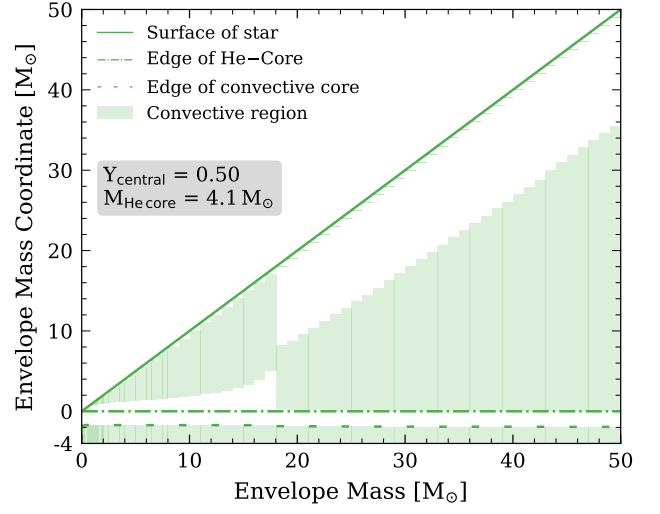


Figure F7. Kippenhahn-like diagram for core–He burning models with a constant $M_{\text{core}} = 4.1M_{\odot}$ and varying envelope mass. See caption of Fig. 7 for further details.

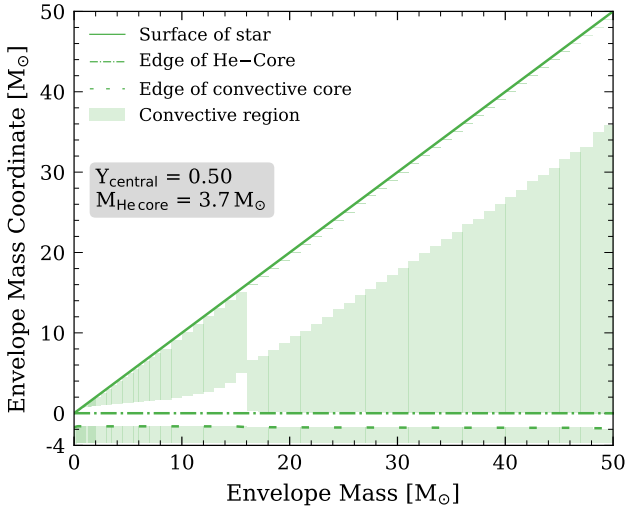


Figure F6. Kippenhahn-like diagram for core–He burning models with a constant $M_{\text{core}} = 3.7M_{\odot}$ and varying envelope mass. See caption of Fig. 7 for further details.

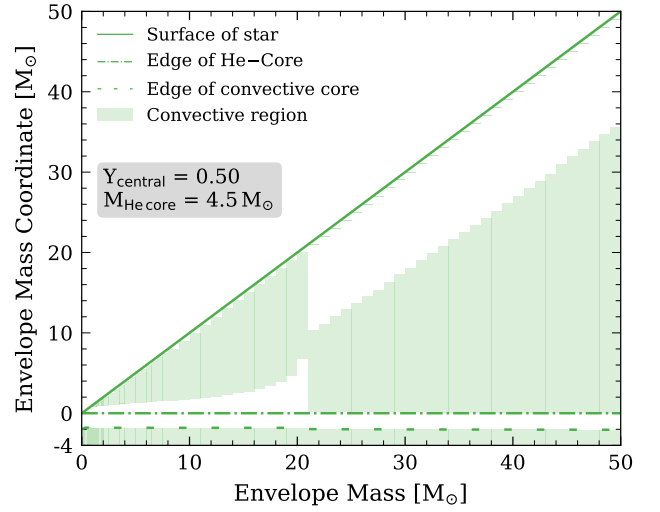


Figure F8. Kippenhahn-like diagram for core–He burning models with a constant $M_{\text{core}} = 4.5M_{\odot}$ and varying envelope mass. See caption of Fig. 7 for further details.

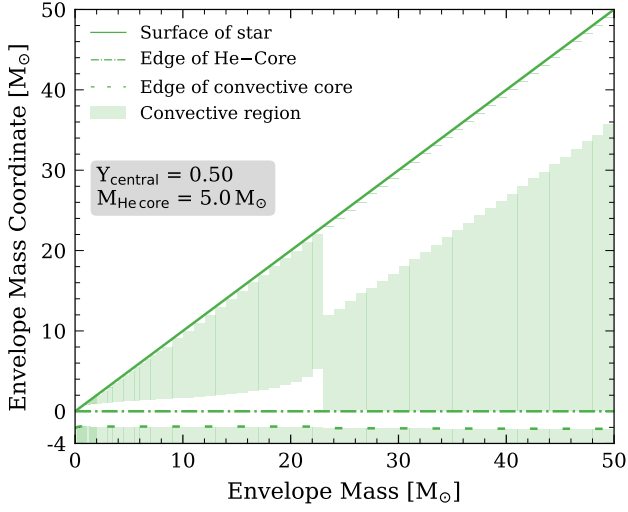


Figure F9. Kippenhahn-like diagram for core-He burning models with a constant $M_{\text{core}} = 5.0 M_{\odot}$ and varying envelope mass. See caption of Fig. 7 for further details.

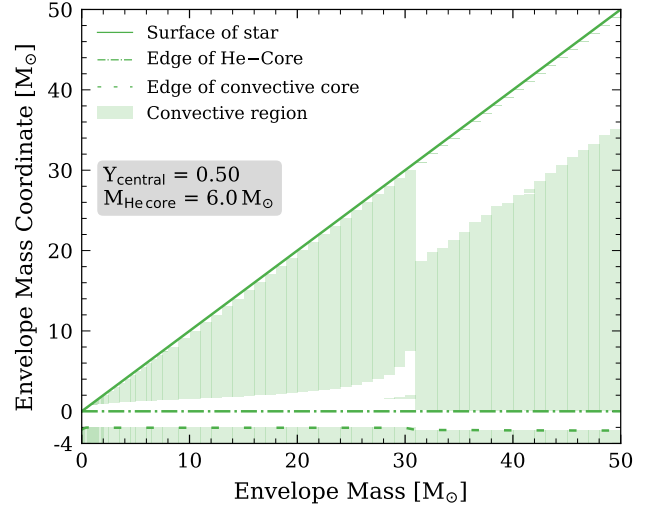


Figure F11. Kippenhahn-like diagram for core-He burning models with a constant $M_{\text{core}} = 6.0 M_{\odot}$ and varying envelope mass. See caption of Fig. 7 for further details.

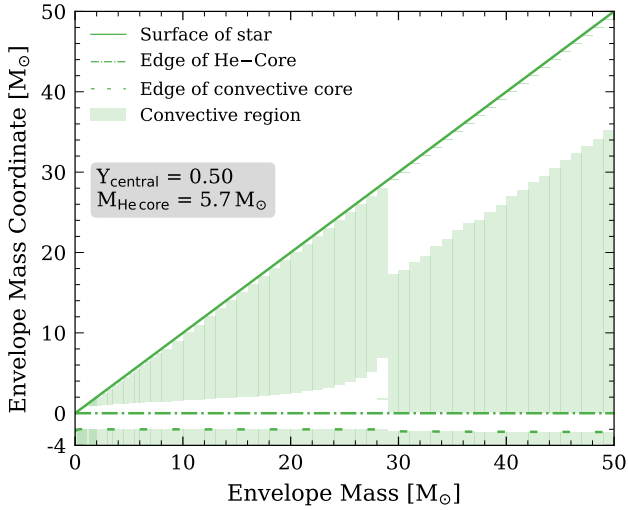


Figure F10. Kippenhahn-like diagram for core-He burning models with a constant $M_{\text{core}} = 5.7 M_{\odot}$ and varying envelope mass. See caption of Fig. 7 for further details.

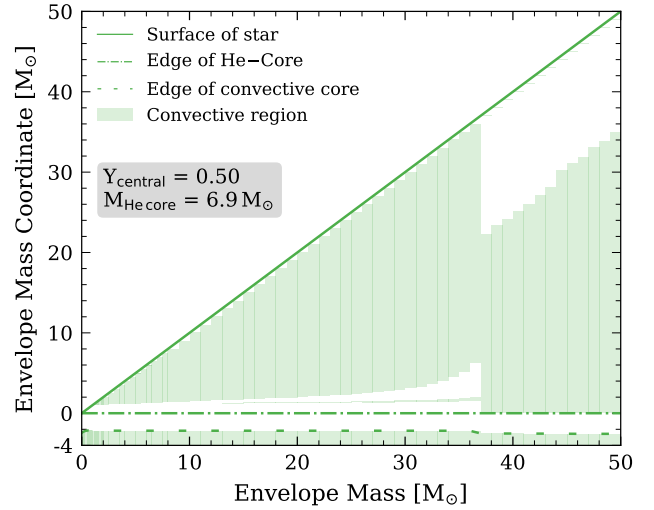


Figure F12. Kippenhahn-like diagram for core-He burning models with a constant $M_{\text{core}} = 6.9 M_{\odot}$ and varying envelope mass. See caption of Fig. 7 for further details.

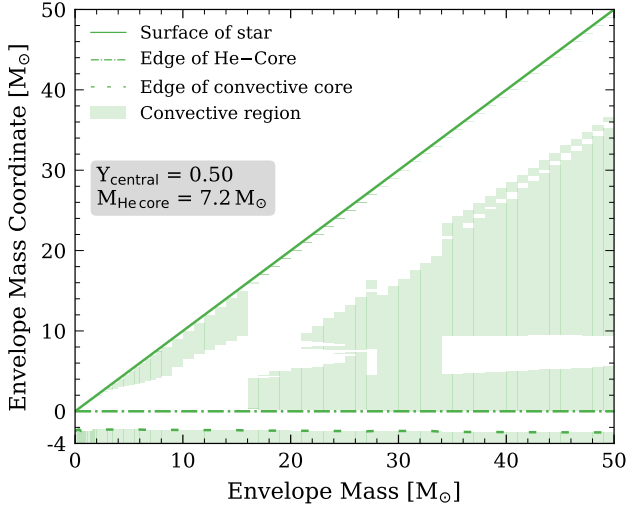


Figure F13. Kippenhahn-like diagram for core-He burning models with a constant $M_{\text{core}} = 7.2M_{\odot}$ and varying envelope mass. See caption of Fig. 7 for further details.

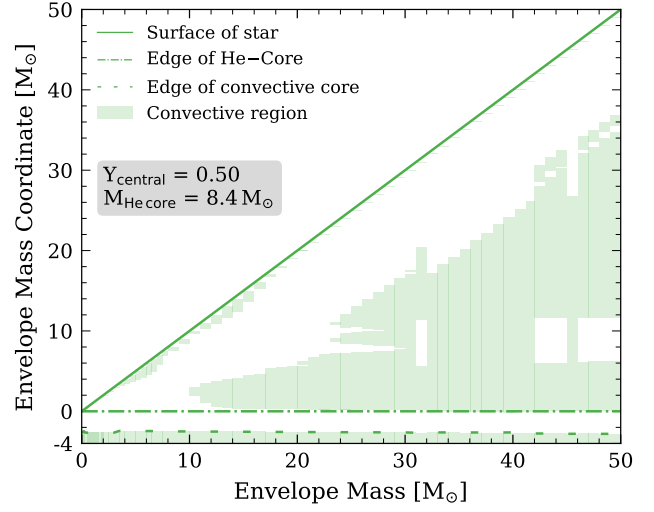


Figure F15. Kippenhahn-like diagram for core-He burning models with a constant $M_{\text{core}} = 8.4M_{\odot}$ and varying envelope mass. See caption of Fig. 7 for further details.

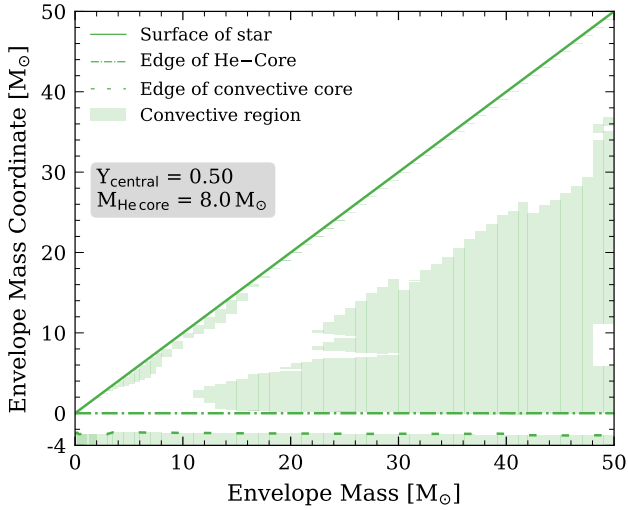


Figure F14. Kippenhahn-like diagram for core-He burning models with a constant $M_{\text{core}} = 8.0M_{\odot}$ and varying envelope mass. See caption of Fig. 7 for further details.

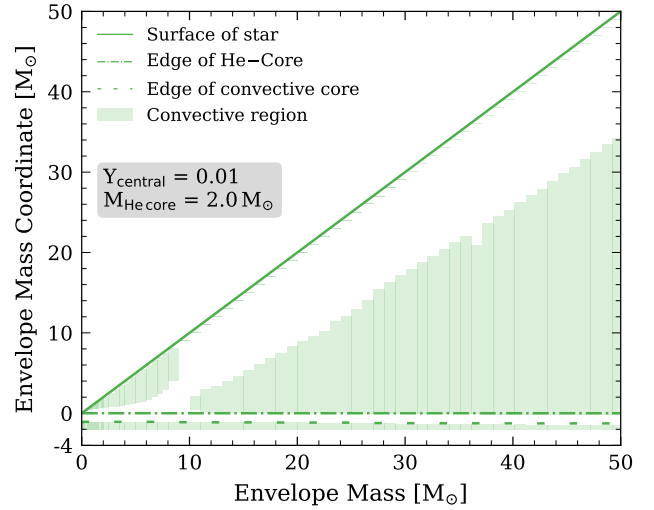


Figure F16. Kippenhahn-like diagram for core-He burning models with a constant $M_{\text{core}} = 2.0M_{\odot}$ and varying envelope mass. See caption of Fig. 7 for further details.

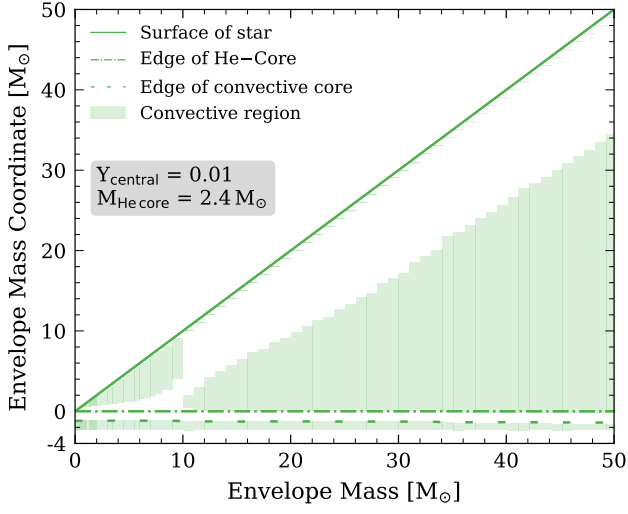


Figure F17. Kippenhahn-like diagram for core-He burning models with a constant $M_{\text{core}} = 2.4M_{\odot}$ and varying envelope mass. See caption of Fig. 7 for further details.

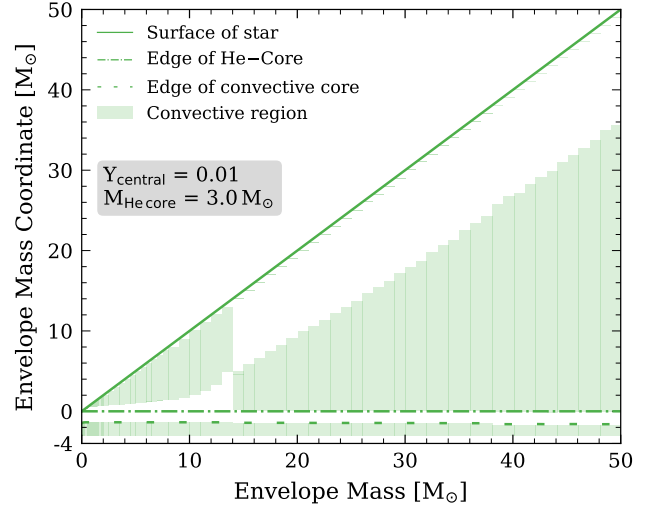


Figure F19. Kippenhahn-like diagram for core-He burning models with a constant $M_{\text{core}} = 3.0M_{\odot}$ and varying envelope mass. See caption of Fig. 7 for further details.

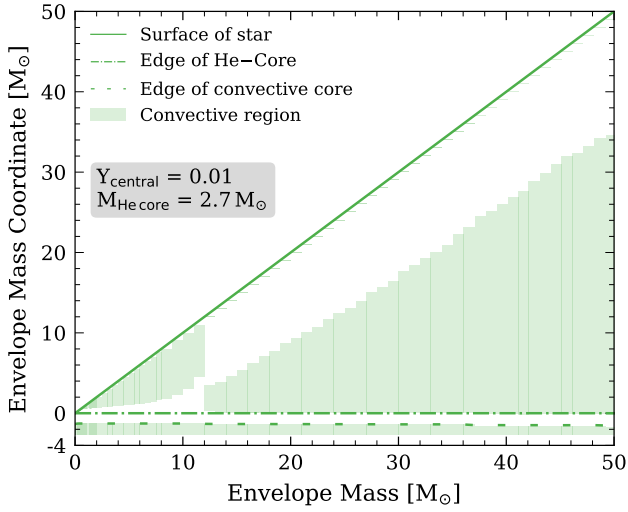


Figure F18. Kippenhahn-like diagram for core-He burning models with a constant $M_{\text{core}} = 2.7M_{\odot}$ and varying envelope mass. See caption of Fig. 7 for further details.

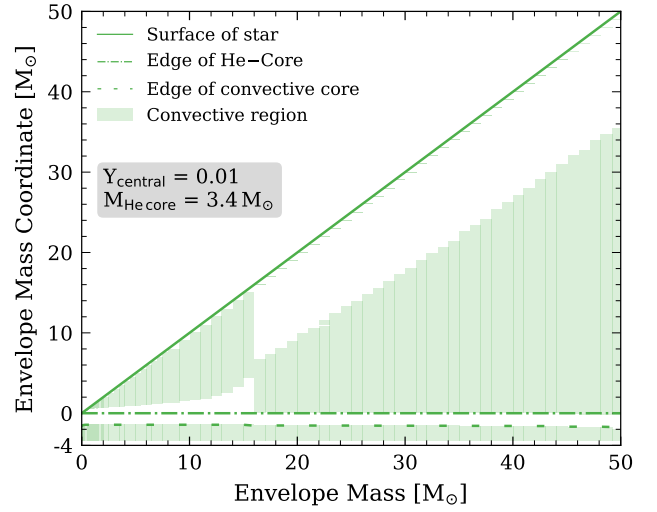


Figure F20. Kippenhahn-like diagram for core-He burning models with a constant $M_{\text{core}} = 3.4M_{\odot}$ and varying envelope mass. See caption of Fig. 7 for further details.

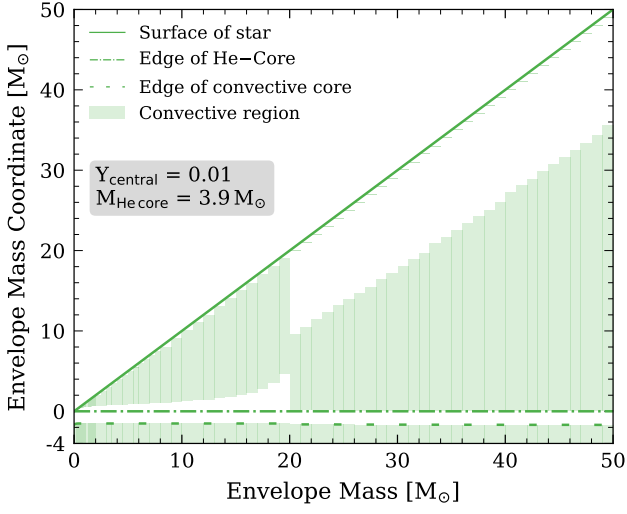


Figure F21. Kippenhahn-like diagram for core-He burning models with a constant $M_{\text{core}} = 3.9M_{\odot}$ and varying envelope mass. See caption of Fig. 7 for further details.

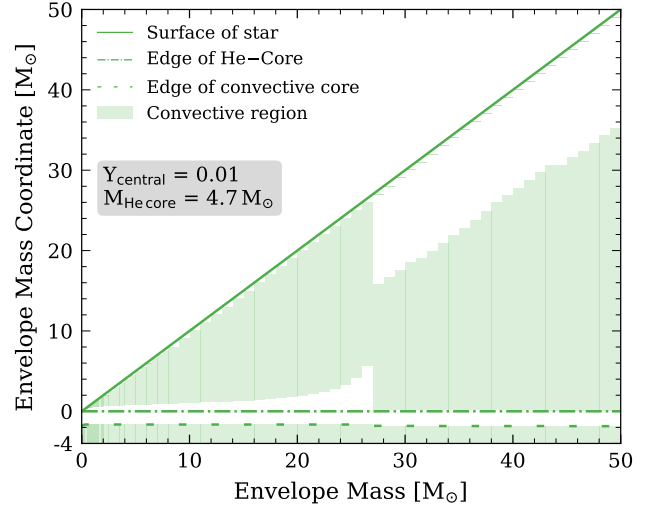


Figure F23. Kippenhahn-like diagram for core-He burning models with a constant $M_{\text{core}} = 4.7M_{\odot}$ and varying envelope mass. See caption of Fig. 7 for further details.

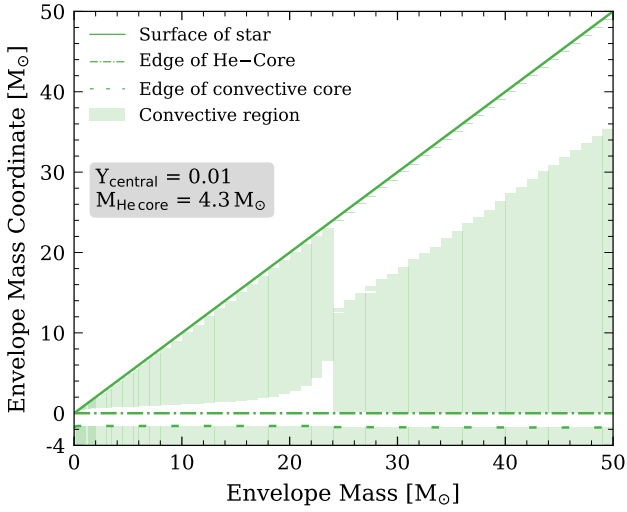


Figure F22. Kippenhahn-like diagram for core-He burning models with a constant $M_{\text{core}} = 4.3M_{\odot}$ and varying envelope mass. See caption of Fig. 7 for further details.

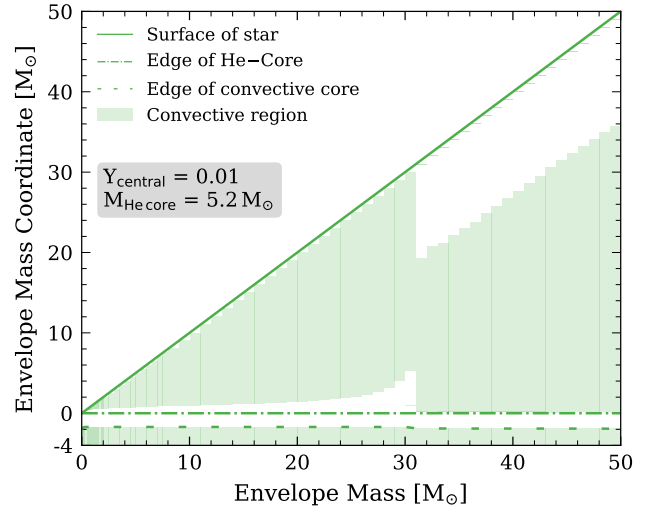


Figure F24. Kippenhahn-like diagram for core-He burning models with a constant $M_{\text{core}} = 5.2M_{\odot}$ and varying envelope mass. See caption of Fig. 7 for further details.

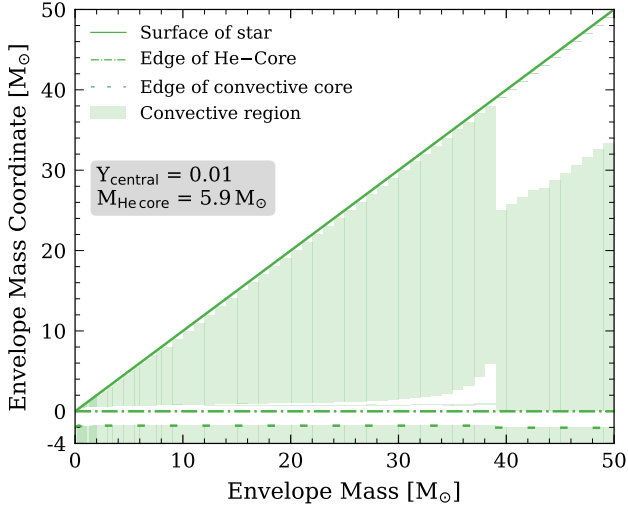


Figure F25. Kippenhahn-like diagram for core-He burning models with a constant $M_{\text{core}} = 5.9M_{\odot}$ and varying envelope mass. See caption of Fig. 7 for further details.

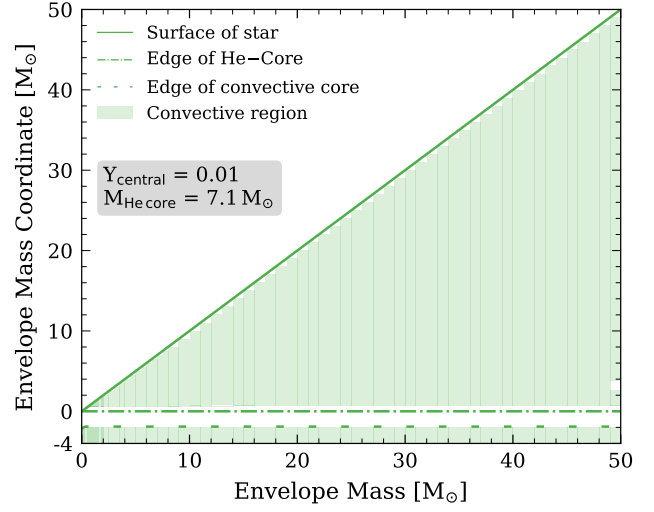


Figure F27. Kippenhahn-like diagram for core-He burning models with a constant $M_{\text{core}} = 7.1M_{\odot}$ and varying envelope mass. See caption of Fig. 7 for further details.

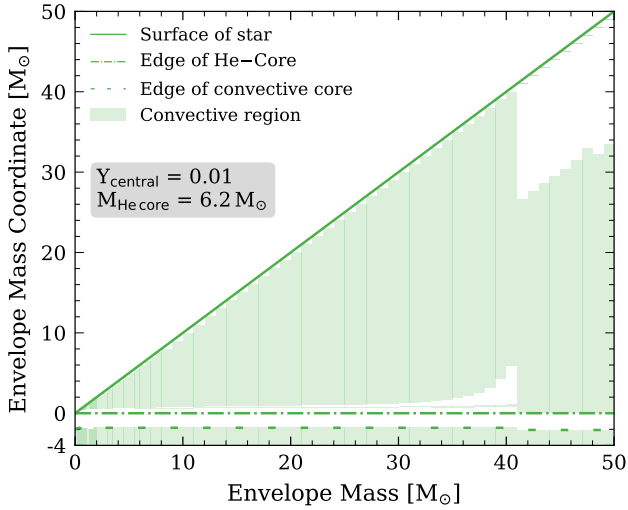


Figure F26. Kippenhahn-like diagram for core-He burning models with a constant $M_{\text{core}} = 6.2M_{\odot}$ and varying envelope mass. See caption of Fig. 7 for further details.

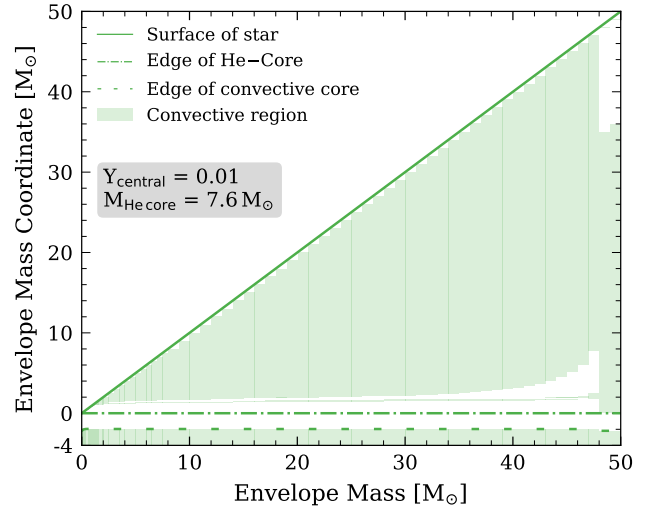


Figure F28. Kippenhahn-like diagram for core-He burning models with a constant $M_{\text{core}} = 7.6M_{\odot}$ and varying envelope mass. See caption of Fig. 7 for further details.

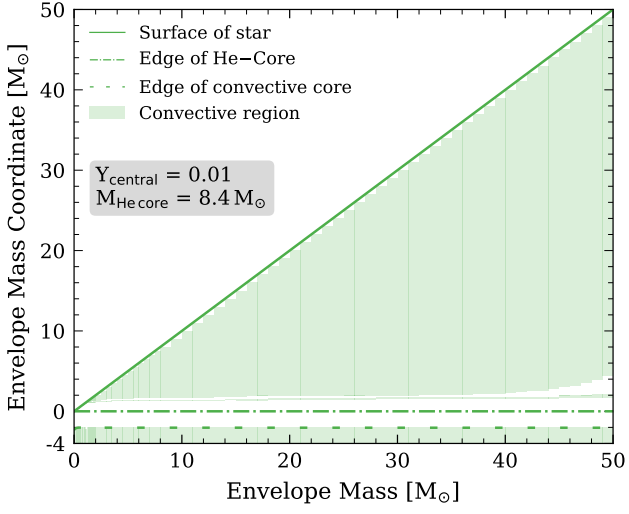


Figure F29. Kippenhahn-like diagram for core-He burning models with a constant $M_{\text{core}} = 8.4M_{\odot}$ and varying envelope mass. See caption of Fig. 7 for further details.

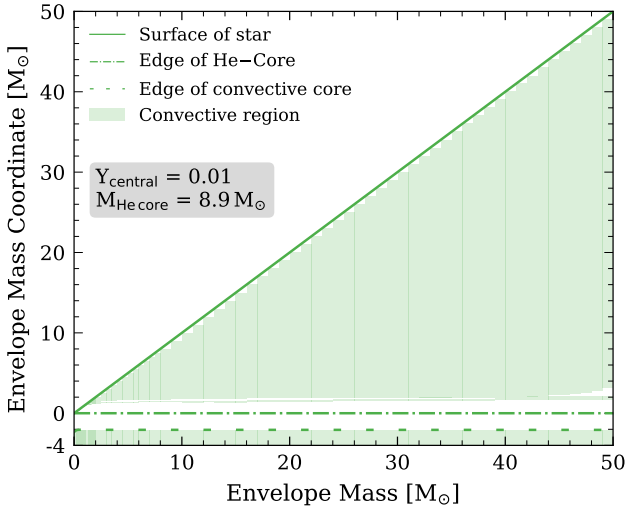


Figure F30. Kippenhahn-like diagram for core-He burning models with a constant $M_{\text{core}} = 8.9M_{\odot}$ and varying envelope mass. See caption of Fig. 7 for further details.